

**Solar Eruptive Events:
Coronal Dimming and a New CubeSat Mission**

by

James Paul Mason

B.S., University of California at Santa Cruz, 2009

M.S., University of Colorado at Boulder, 2012

A thesis submitted to the
Faculty of the Graduate School of the
University of Colorado in partial fulfillment
of the requirements for the degree of
Doctor of Philosophy
Department of Aerospace Engineering Sciences
2016

This thesis entitled:
Solar Eruptive Events:
Coronal Dimming and a New CubeSat Mission
written by James Paul Mason
has been approved for the Department of Aerospace Engineering Sciences

Dr. Thomas Woods

Prof. Xinlin Li

Prof. Scott Palo

Dr. Amir Caspi

Prof. Jeffrey Forbes

Date _____

The final copy of this thesis has been examined by the signatories, and we find that both the content and the form meet acceptable presentation standards of scholarly work in the above mentioned discipline.

Mason, James Paul (Ph.D., Aerospace Engineering Sciences)

Solar Eruptive Events:

Coronal Dimming and a New CubeSat Mission

Thesis directed by Dr. Thomas Woods

Often the abstract will be long enough to require more than one page, in which case the macro “\OnePageChapter” should *not* be used.

But this one isn’t, so it should.

Dedication

To my late father, who inspired me from an early age to come this far.

Acknowledgements

First and foremost, my deepest thanks to Tom Woods. Through the projects he's introduced me to – in solar physics, in sounding rockets, and in small satellites – I've discovered a career path that excites me and that provides continuous opportunities to learn and contribute. Moreover, he's an excellent role model: dedicated and passionate about his work, patient with everyone without seeming to have to try, and exceptionally reliable. All of the above combined has made my time in graduate school likely to be, upon reflection long from now, one of the highlights of my life. Thank you to my committee for guidance and support, most of whom I've been fortunate to work with closely: Xinlin Li, Scott Palo, Amir Caspi, and Jeff Forbes. Finally, I couldn't have struggled through without the support of my peers, especially Allison Youngblood, whose work ethic inspires me and whom I've been extremely lucky to find. Oh, and my dog, Nessie, who requires three walks a day, has turned out to provide the periods of relaxation away from a screen that have aided in my ability to actually comprehend the work I'm doing.

Contents

Chapter

1	Introduction	1
2	Relevant Background	3
2.1	Brief Tour of the Sun	3
2.1.1	Core	4
2.1.2	Radiative Zone	6
2.1.3	Convection Zone	8
2.1.4	Photosphere	9
2.1.5	Chromosphere	10
2.1.6	Electromagnetic Radiation From Atoms and Charged Particles	11
2.1.7	Transition Region	12
2.1.8	Thermodynamic Equilibrium	15
2.1.9	Corona	15
2.1.10	Heliosphere	15
2.2	Physics of Solar Eruptive Events	15
2.2.1	Magnetic Energy Storage	15
2.2.2	Energy Release Overview	15
2.2.3	Solar Flares	15
2.2.4	Coronal Mass Ejections	15

2.3	Space Weather	15
2.4	Instrument Descriptions	15
2.4.1	Spectrographs	15
2.4.2	Spectral Imagers	15
2.4.3	Magnetic Imagers	15
2.4.4	Coronagraphs	15
2.4.5	In-situ Measurements	15
3	Mechanisms and Observational Signatures of Coronal Dimming	17
3.1	Mass-loss Dimming	19
3.2	Thermal Dimming	20
3.3	Obscuration Dimming	23
3.4	Wave Dimming	25
3.5	Doppler and Bandpass Dimming	27
3.6	Dimming Physics and Observations Summary	30
4	Coronal Dimming Case Studies	32
4.1	Observations and Analysis	33
4.1.1	Simple Dimming Case	33
4.1.2	Complex Dimming Case	40
4.2	Flare-Dimming Deconvolution Method	49
4.3	Error Estimates for Flare-Dimming Deconvolution Method	52
4.4	Dimming Parameterization Results	55
4.4.1	Simple Dimming Case	55
4.4.2	Complex Dimming Case	57
4.5	Case Studies Summary	59

5	Semi-Statistical Study of Dimming-CME Relationship	61
5.1	Introduction to Dimming and CME Parameterization and Statistics	62
5.2	Observations and Event Selection	64
5.3	Flare-Dimming Deconvolution Method Statistics	68
5.4	Dimming Light Curve Fitting Method	71
5.4.1	Physics Motivation and Fit Types	71
5.4.2	Dimming Fit Uncertainty Computation	74
5.5	Parameterization Methods	75
5.5.1	Dimming Parameterization	76
5.5.2	CME Parameterization	77
5.6	Dimming and CME Parameters Correlation	78
5.7	Summary	81
6	Overview of MinXSS Solar CubeSat	82
6.1	Brief CubeSat Introduction	82
6.2	Science Objectives	84
6.2.1	Solar Flare Studies	85
6.2.2	Topics Beyond Solar Eruptive Events	88
6.3	Mission Architecture	89
6.3.1	Primary Instrument: Amptek X123-SDD	90
6.3.2	Secondary Instrument: Solar Position Sensor and X-Ray Sensor	92
6.3.3	CDH and Flight Software	93
6.3.4	Electrical Power System, Battery, and Solar Panels	95
6.3.5	Communications	96
6.3.6	Attitude Determination and Control System	97
6.4	Advancing CubeSat Technologies and Lessons Learned	98
6.4.1	CubeSat Card Cage	98

6.4.2	3-D Printed Parts	99
6.4.3	Simplification of Solar Panel Fabrication Process	100
6.4.4	Pseudo-Peak Power Tracking	101
6.4.5	Importance of Flight Like Testing	104
6.4.6	Importance of a Second CubeSat Unit	107
6.4.7	Low-Cost Mitigation of Radiation Issues for Electronics	108
6.5	Summary	108
Bibliography		110
Appendix		
A	Coronal Dimming Event List and Ancillary Data	117
B	MinXSS CubeSat Mass/Power Tables	118

Tables**Table**

2.1	Selected emission lines and temperatures	14
3.1	Dimming mechanisms summary	18
4.1	2011 August 4 event statistics	44
4.2	EVE precision by emission line	52
4.3	Key dimming results for 2010 August 7 event	57
5.1	Semi-statistical study event list	67
5.2	Dimming-CME parameter correlations	79

Figures

Figure

2.1	Sun Structure Cutaway	3
2.2	Solar Temperature and Density Versus Height	5
2.3	Solar Plasma β Versus Height	6
2.4	Solar Elemental Abundances	7
2.5	Surfacing of magnetic field	8
2.6	Sunspots and Active Regions	9
2.7	Spicules of the Chromosphere	10
2.8	Atomic Transitions for Balmer and Lyman Series	11
2.9	Fe Ionization Fraction	14
2.10	AIA bandpasses	16
3.1	Schematic of mass-loss dimming	20
3.2	Schematic of thermal dimming	21
3.3	Outflow velocity vs temperature	22
3.4	Dimming dependence on temperature in EVE	24
3.5	Schematic of obscuration dimming	25
3.6	Photoionization cross-sections for H and He	26
3.7	Schematic of obscuration dimming	27
3.8	Geometry and effect of Doppler dimming	28

3.9	Bandpass dimming	29
4.1	LASCO coronagraph data for 2010 August 7 event	33
4.2	LASCO coronagraph data for 2010 August 7 event	34
4.3	AIA contour analysis for 2010 August 7 event	36
4.4	AIA before/after images of 2010 August 7 event	37
4.5	EVE selected extracted emission lines for 2010 August 7 event	39
4.6	LASCO and STEREO coronagraph data for 2011 August 4 event	40
4.7	Historical CME speed histogram	41
4.8	AIA contour analysis for 2011 August 4 event	42
4.9	Additional AIA contour analysis for 2011 August 4 event	45
4.10	AIA wave analysis for 2011 August 4 event	46
4.11	EVE selected extracted emission lines for 2011 August 4 event	48
4.12	Flare-dimming deconvolution method example	50
4.13	Flare-dimming deconvolution algorithm schematic	51
4.14	Dimming parameterization for 2010 August 7 event	56
4.15	Dimming parameterization for 2011 August 4 event	58
5.1	Selected four week period in historical context	65
5.2	All deconvolution combinations example	69
5.3	Limb CME expansion and dimming	72
5.4	Dimming best fit statistics	74
5.5	Dimming fits example	75
5.6	Dimming-CME correlations	79
5.7	Correlations: dimming depth vs high and low CME mass	80
6.1	Photo of 3 MinXSS CubeSat models	83
6.2	History of solar SXR measurements	86

6.3	XPS vs ESP SXR measurements	86
6.4	MinXSS requirements flowdown	90
6.5	MinXSS mechanical block diagram	91
6.6	SPS and XS exploded view	94
6.7	CubeSat card cage	98
6.8	Aluminum 3-D printed SPS and XS	99
6.9	Stainless steel 3-D printed solar panel hinges	100
6.10	MinXSS solar panel	101
6.11	Pseudo-Peak power tracker circuit	102

Chapter 1

Introduction

- Solar eruptive events are rapid releases of energy on the Sun that are sometimes directed Earth-ward, making it important to understand them and to forecast their arrival time and magnitude of their impact
- Three basic types of eruptive event: flare, coronal mass ejection, energetic particles this dissertation focuses on the first two
- Some background about solar flare prediction provided in Chapter 2, including my own massive statistical study, which went to print in ApJ my first year of graduate school
- The relationship between coronal mass ejections and the void they leave behind in the solar corona is the primary topic of the dissertation and its discussion spans several chapters.
 - * Chapter 3 discusses the various physical processes that can lead to an observation that may be interpreted as a dimming, and the amalgamation of related observations that can theoretically be used to identify and isolate each mechanism
 - * Chapter 4 puts theory to the test in a detailed case study of a single, relatively simple, event. The aforementioned conglomeration of observations were used to determine that this was indeed a simple case with one dimming mechanism dominating the observation; that which theory says should be most strongly related to the associated CME

- * Chapter 5 expands the study of the relationship between dimming and CMEs by performing an analysis similar to that of the case study but for approximately 30 events. Thus, a tentative statistical correlation between dimming and CME parameterizations could be derived.
- The topic of solar flares is picked up again briefly in the science motivation for the solar CubeSat MinXSS. An overview of the mission is the topic of Chapter 6, which includes science motivation, system overview, and lessons learned.
- Chapter 7 delves deeper into the CubeSat engineering with a detailed thermal balance test and model analysis, culminating in the (likely) first ever tuned CubeSat thermal model that has been validated by dedicated testing and on-orbit measurements.
- Chapter 8 provides a summary of deliverables and results, and lays out plans for future work. The latter will be the first steps in my post-doc that has already been secured through my first grant being funded as well as SDO/EVE and MinXSS extended mission funding.

Chapter 2

Relevant Background

2.1 Brief Tour of the Sun

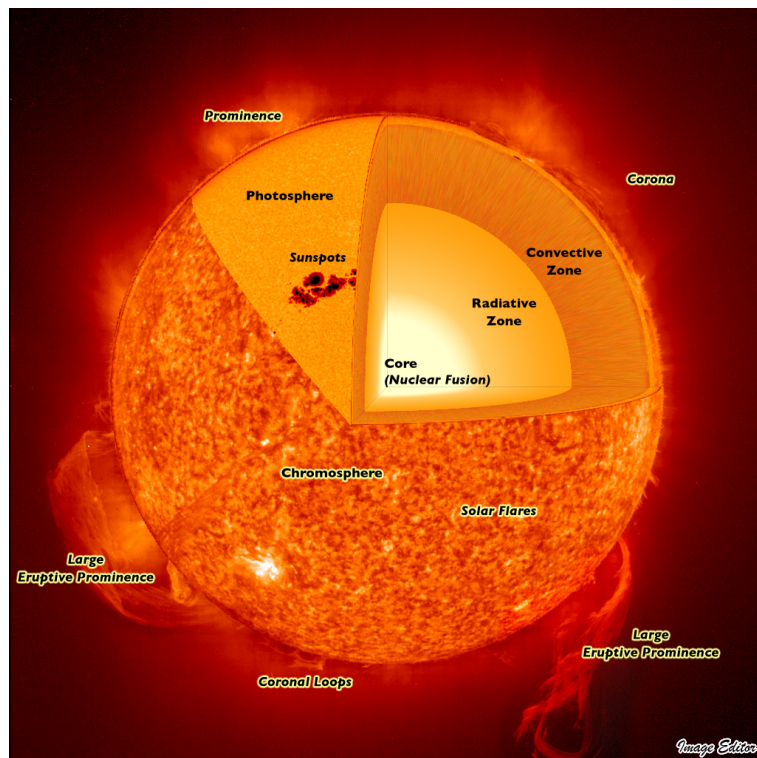


Figure 2.1: Sectional cutaway diagram of the sun to show basic structure. Figure courtesy of Image Editor on flickr

Figure 2.1 shows the basic structure of the sun. Nuclear fusion occurs in the core and produces high-energy photons that slowly travel outward through the radiative zone. In every imaginary spherical surface centered on the core, the net energy flux outward must be positive

else the sun would explode. In the convection zone, the dominant form of heat transport becomes mass plasma motion that circulates hot matter upward where it cools and sinks back down. At the photosphere, the opacity drops rapidly and photons are free to fly. The undulating chromosphere lies just above the photosphere; it is vastly out-shined by the photosphere except in a few special wavelengths corresponding to dark absorption lines in the photosphere. The transition region is so named for the dramatic and unintuitive temperature increase from the chromosphere to the corona. Through the interior of the sun, the temperature and density steadily drop (see Figure 2.2) as one would expect from everyday experience, for example, temperature drops further from a campfire. Nevertheless, the transition region escalates the temperature, bringing the corona to 1 MK. Where the sun below and far above the corona are dominated by gas dynamics, the corona itself is dominated by magnetic fields. This trade-off is characterized by the β parameter:

$$\beta = \frac{p_{gas}}{p_{mag}} = \frac{nk_B T}{B^2/(2\mu_0)} \quad (2.1)$$

where p_{gas} is the pressure of a gas (or plasma in this case), p_{mag} is the magnetic pressure, n is the number density, k_B is Boltzmann's constant, T is temperature, B is the strength of the magnetic field, and μ_0 is the permeability of free space. When $\beta > 1$, normal gas pressure dominates and when $\beta < 1$, magnetic pressure dominates. The transition from $\beta > 1$ to $\beta < 1$ is an important one for understanding how vast amounts of energy can be stored in the solar atmosphere, providing the necessary power to drive solar eruptive events. β as a function of height above the photosphere is shown in Figure 2.3.

The following sections will step through each layer of the sun with descriptive detail proportional to their relevance to the work to be presented in later chapters.

2.1.1 Core

The gravitational pressure and density in the core of stars is sufficient to ignite nuclear fusion. In a main sequence star at the midpoint of its life, like the sun, the primary fusion reaction is the conversion of hydrogen to helium. The majority of the sun is made of hydrogen (see Figure 2.4) – a

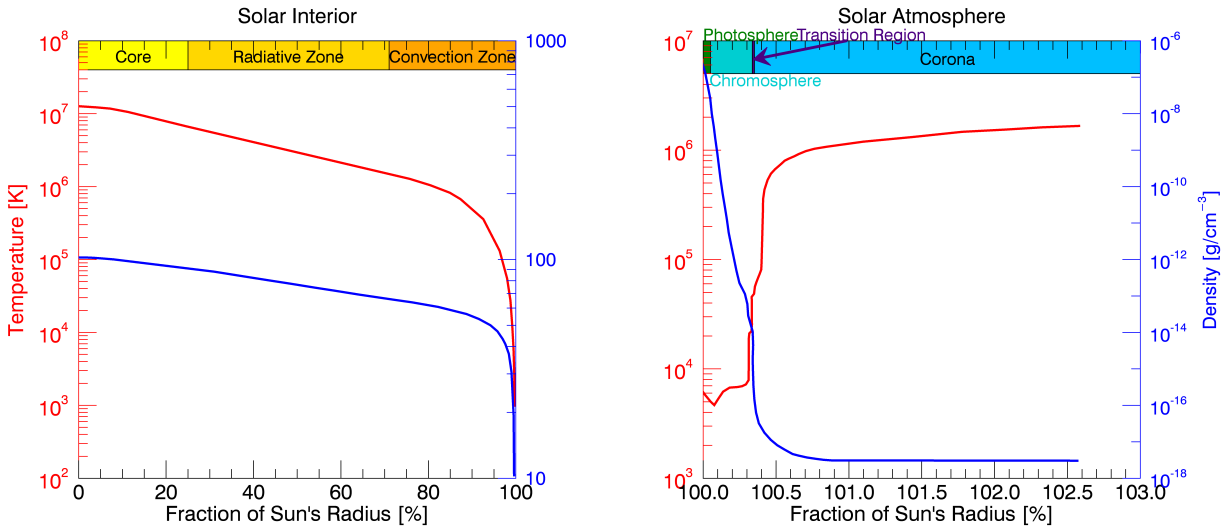


Figure 2.2: Solar temperature and density versus height from the core to the corona. Data adapted from various sources. Atmospheric temperature and density from Eddy (1979), interior temperature from Lang (2001), and interior density from Christensen-Dalsgaard et al. (1996).

reflection of its relative abundance in the universe at large. Fusion in the core of stars is responsible for producing elements up to iron; the fusion process for elements heavier than iron is endothermic and thus cannot be used by the star to support itself against gravity. Instead, heavier elements are produced during supernovae. Supernovae also spread the source star’s fusion products far away where they are incorporated into newly forming stars. Thus, the sun has observable metals¹ such as Fe even though it has not reached the point in its life where it produces them itself. The metals in these second and third generation stars are not confined to the core; rather, they can be found even in the corona. In subsequent sections it will become clear that having various elemental species at different stages of ionization in the directly observable solar atmosphere provides a means of determining temperature and structure.

¹ “metals” here is in the astrophysical sense of any element that is not hydrogen or helium

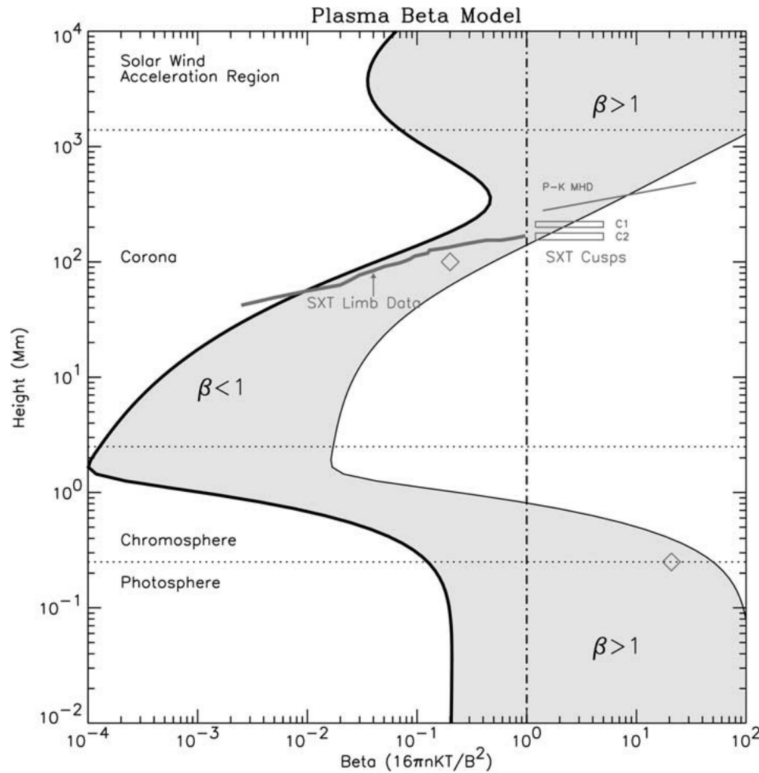


Figure 2.3: Solar plasma β versus height from the photosphere through the corona. Figure courtesy of Gary (2001).

2.1.2 Radiative Zone

Every nuclear reaction in the core generates high-energy photons. It takes thousands to hundreds of thousands of years for these photons to reach the surface because the incredible density of the solar interior results in a mean free path for photons on the order of centimeters. Because the density decreases with radial distance from the center (blue line in Figure 2.2), there is a subtle bias in the mean free path of the photons that causes the net direction to be outward. This is the physical process that characterizes the radiative zone. The net outward flux of energy (heat/photons) must be positive else the energy build up would result in an explosion. Additionally, temperature decreases with distance from the center (red line in Figure 2.2). When in thermodynamic equilibrium, as the solar interior is, atomic emission of photons obeys Planck's law, which describes

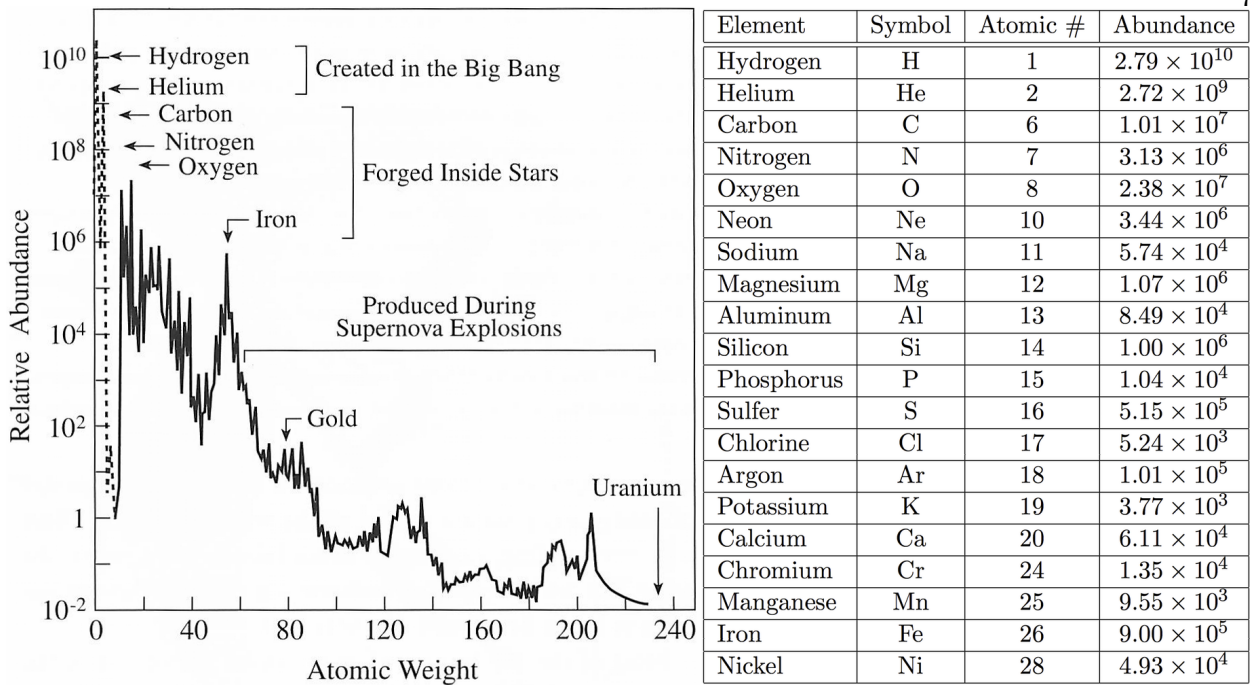


Figure 2.4: (Left) A plot of the abundance of all elements in the sun. (Right) A corresponding table of the 20 most abundant elements. Values in the plot and table are normalized to the abundance of Si, 1.00×10^6 . Figure and plot are adapted from Lang (2001).

blackbody emission:

$$S_\lambda = \frac{8\pi hc}{\lambda^5} \frac{1}{e^{hc/\lambda k_B T} - 1} \quad (2.2)$$

where S is the spectral radiance of a body at a particular temperature, λ is wavelength, h is Planck's constant, c is the speed of light, k_B is Boltzmann's constant, and T is temperature. This equation can be interpreted simply as a lower temperature resulting in lower energy emission (i.e., longer wavelength). Thus, as photons move outward from the core, they are absorbed by atoms at lower temperature and reemitted at longer wavelengths. In order to conserve energy, multiple photons of lower energy must be emitted. All sunlight is essentially an attenuation of the light generated in the fusing core.

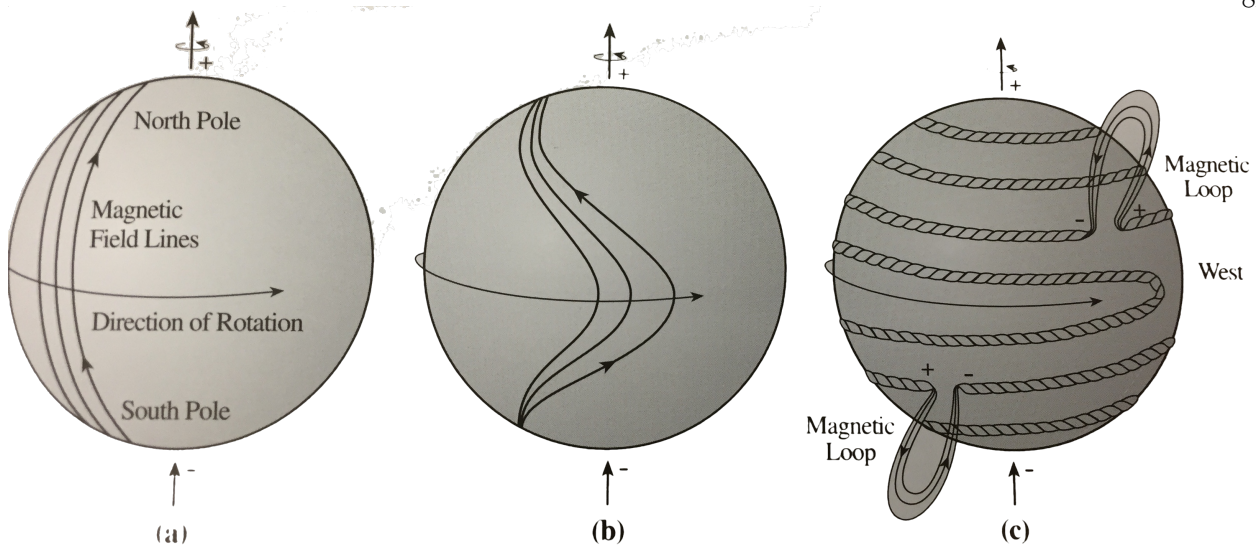


Figure 2.5: (Left) Once the solar dynamo generates a magnetic field vertically around the sun, (middle) differential rotation of the sun causes the field to wrap around the sun, (right) and any small kinks in the field are lifted by their buoyancy in an Ω loop. Figure courtesy of Lang (2001).

2.1.3 Convection Zone

At approximately 70% of the sun's radius, the dominant outward heat transport mechanism changes from radiation to convection. Plasma stores heat near the base of the zone and its buoyancy causes it to rise to a point where its heat can be rapidly dissipated (this point is the photosphere where radiative cooling becomes highly effective). The cooled plasma then sinks back down where it will again be heated at the base of the convection zone, establishing the cycle of heat transport. The observed convective cells at the photosphere are known as granules and supergranules. The difference between them is size and that supergranules have much slower horizontal plasma flow. Additionally, the convection zone is responsible for many of the dynamics observed in the corona (to be described in subsequent sections), which are due to the strong magnetic field and $\beta < 1$ in the corona. The magnetic field is thought to be generated at the base of the convection zone. The precise mechanism of the solar dynamo is not yet well understood, but the surfacing of the field is likely described by slight kinks in the field being lifted by plasma buoyancy (see Figure 2.5). $\beta > 1$ in the convection zone, so the magnetic field generated at the base is subject to the upward plasma

motion as just described. Once it reaches the solar atmosphere, the magnetic field dominates and so is not pulled back down with the sinking plasma.

2.1.4 Photosphere

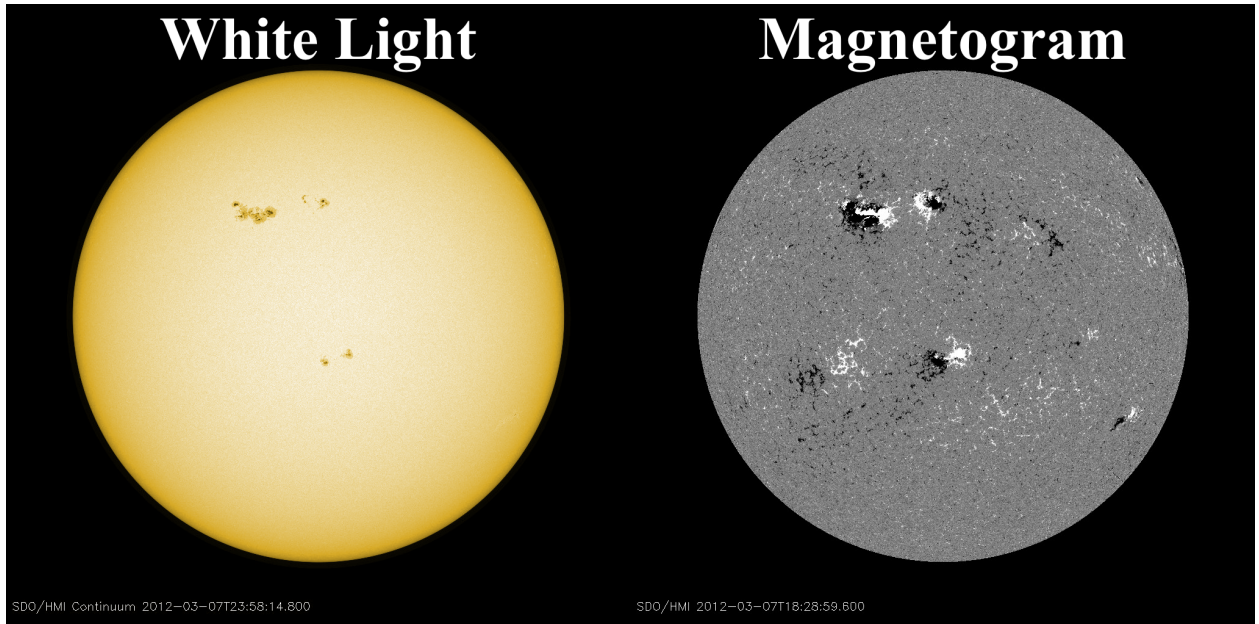


Figure 2.6: (Left) White light image of the solar photosphere on 2012 March 5. (Right) The corresponding photospheric line-of-sight magnetic field. Black indicates field into the page and white field out of the page. These data come from the Helioseismic Magnetic Imager onboard the Solar Dynamics Observatory spacecraft, to be described in Section 2.4.

The photosphere is a thin ($\tilde{300}$ km or 0.05% of the solar radius) layer where the opacity suddenly drops and photons can escape to space more or less unscathed. It is often referred to as the “surface” of the sun but this label can be misleading since the density at the photosphere is 2500 more tenuous than the *air* on top Mount Everest. The photosphere is constantly roiling; the lifetime of a granule is only about 8 minutes and large-scale patterns of supergranules last about 24 hours. In each granule, hot plasma rises at the center and sinks at the edges. Magnetic field is collected at the edges of the supergranules as plasma motion can move magnetic field in the photosphere. Sunspots, concentrated dark regions in photospheric white light² (Figure ??,

² “white light” refers to the integrated visible spectrum emission

left), correspond to regions of concentrated magnetic field. In these locations, magnetic pressure alleviates some of the gas pressure, which lowers the temperature (see numerator of Equation 2.1), and thus the emission peak and intensity decrease according to Planck’s law (Equation 2.2). These areas are known as active regions when viewed in magnetogram data (Figure 2.6, right) and are the primary source for solar eruptive events (see Section 2.2).

2.1.5 Chromosphere

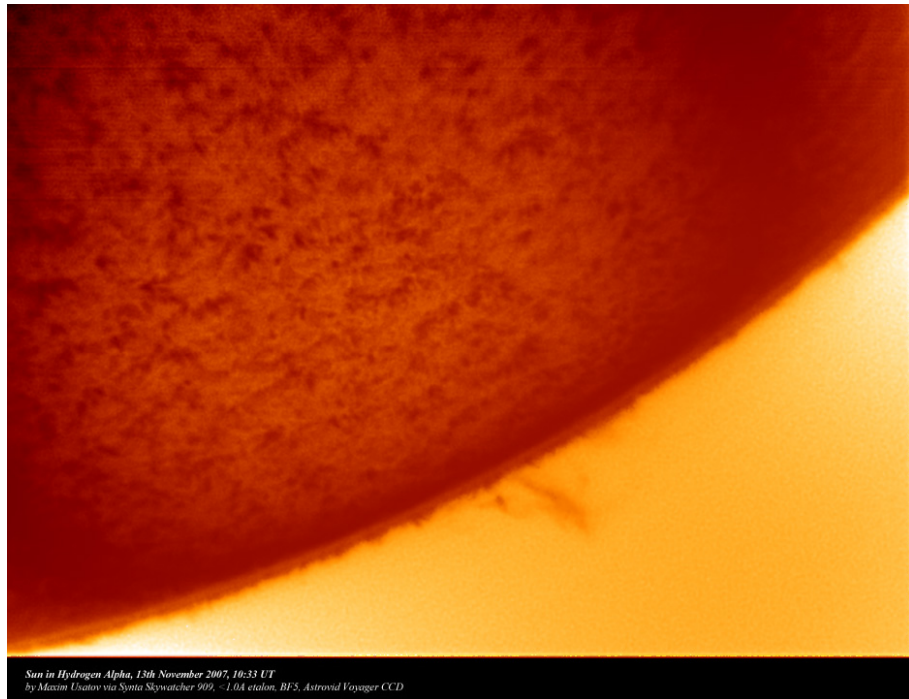


Figure 2.7: Chromospheric spicules visible on the limb³ of the sun, imaged in H α . This photo was taken by an amateur astronomer from the ground, Maxim Usatov.

The chromosphere is an irregular layer of the sun that mostly consists of small jets known as spicules (Figure 2.7). The chromosphere was initially discovered and only observable during natural solar eclipses for a few seconds around totality when the bright photosphere was blocked. The layer has a dominant red color, which guided the selection of its name (“chromo” comes from the Greek word for color). The red light comes primarily from H α emission. H α comes from the $n = 3 \rightarrow 2$ transition of hydrogen (Figure 2.8). The next section will go into the details of electromagnetic

radiation, including this type of bound-bound emission. Instruments can use filters to select this particular wavelength, making observation of the chromosphere routine and independent of solar eclipses.

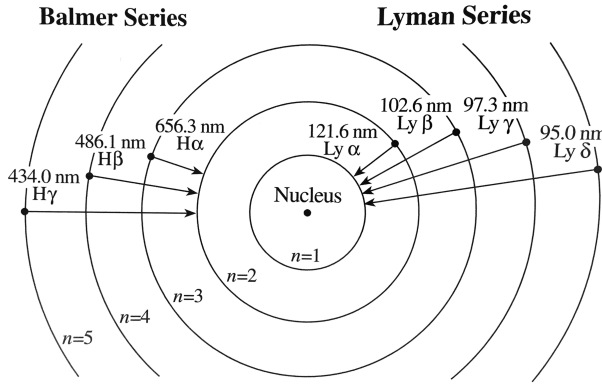


Figure 2.8: Diagram of the hydrogen atom, with electronic orbitals labeled (n). Two important transition series are identified: the Balmer series which includes transitions ending at $n = 2$ and the Lyman series with transitions ending at $n = 1$. The wavelength and common name for the resultant photon emission are also labeled.

2.1.6 Electromagnetic Radiation From Atoms and Charged Particles

There are three basic types of electromagnetic radiation that are emitted by electrons: bound-bound, free-bound, and free-free. Additionally, nuclei can emit photons.

Bound-bound When an electron transitions from one orbital energy of an atom to a lower one, a photon is emitted with the corresponding energy of the transition. Downward energy transitions can occur spontaneously or through a collisional de-excitation, where the atom impacts another particle and transfers some of its energy to the other particle. Upward energy transitions can also occur through collision or by absorption of a photon. The wavelength of the emitted photon is primarily determined by the electronic energy transition but can also be influenced by numerous other processes, for example, the strength of the surrounding magnetic field (Zeeman splitting), collisions during the energy transition, and the relative line-of-sight velocity of the atom with respect to the observer (Doppler). These and other effects result in line broadening, sometimes

to the point of splitting the lines.

Free-bound Also known as radiative recombination, free-bound transitions are those where an atom captures a free electron. When a free electron is captured, a photon is emitted with energy equal to the difference between the kinetic energy of the free electron and the energy of the bound atomic state. The orbitals of the atom have discrete (quantized) energy values but the kinetic energy of free electrons exists on a continuum. Thus light from free-bound transitions is also a continuum in wavelength though it has a lower limit defined by the energy of the bound state it is captured into. The reverse process (bound-free) is ionization and occurs when a photon is absorbed by an atom and an electron is liberated.

Free-free Also known as Bremsstrahlung (“braking radiation”), any accelerating charged particle emits photons according to Maxwell’s equations. The resultant emission is continuum because there are no quantum constraints on the kinetic energy of free particles before or after an acceleration event. Because electrons are much less massive than nuclei, they tend to experience many changes in direction and speed in a dynamic plasma. Even the lightest nucleus – hydrogen, which is just a proton – is 1836 times heavier than an electron. So, while the nucleus will also experience a change in kinetic energy, it is negligible compared to the electron’s. The acceleration in this case is mediated through the powerful electromagnetic force between these oppositely charged particles. It is also possible for the similarly charged ions to accelerate each other, or electrons to accelerate other electrons, but these events are not responsible for the dominant observed emission.

Nuclear decay Nuclei can also be excited into a higher energy state through powerful collisions. When they return to a lower energy state, a photon is emitted and is typically in the gamma range of the spectrum.

2.1.7 Transition Region

The transition region is defined by the rapid increase in temperature between the chromosphere and corona (see Figure 2.2). It is only 100 km thick but is ill defined spatially. Is it in the spicules of the chromosphere? In the loops of active regions? Its location is not obvious and its

existence seems to defy the laws of thermodynamics. The early discovery of how hot the corona was and that the transition region existed was controversial. It depended on temperature-sensitive observations, which have now become routine and widely accepted.

There are several means by which temperature of the solar atmosphere can be inferred. The simplest is the observation of an emission line that has been identified in the laboratory, which specifies the corresponding ion and bound-bound transition. Additional laboratory measurements and theory provide the ionization fraction of each element as a function of temperature (Figure 2.9). A higher temperature results in greater ionization. Thus, observation of an emission line known to correspond to a particular ion is an indicator of that ion's existence in the remote plasma and an approximate temperature can be inferred. Table 2.1 provides some examples for ionization state, corresponding temperature, and a known emission line, which will be used extensively in later chapters.

The next most common method for temperature determination uses the ratio of two emission lines. The flux in each line is dependent on the energy of the bound-bound transition, ΔE , and the collision rates for that transition. The ratio of the line fluxes is temperature sensitive if $\Delta E > kT$. This method can handle non-isothermal plasmas by integrating the collision rates over volume. This method fails if there are two lines used that have source regions that are distant from each other so care must be taken when the source plasma contains spatial variations in density and temperature, as is the case with the sun. Additionally, this method depends on the relative ion abundances, so if ionization balance varies with time, that time variation must be taken into account. Line ratios are not used for temperature determination in this dissertation.

The mechanism responsible for the rapid temperature change through the transition region remains poorly understood and is one of the biggest problems in solar physics. Theories abound to explain it but are beyond the scope of this dissertation. Here, we simply accept that the transition region *does* lead to a much hotter corona, an observational fact that has long been established.

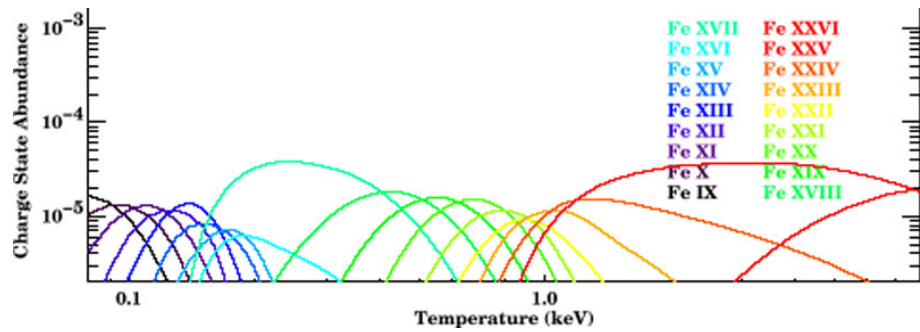


Figure 2.9: Ionization fraction for Fe as a function of energy. Here, energy and temperature are related by a constant value (Boltzmann's constant) and are thus equivalent. Charge state abundance is the product of elemental abundance and ionic fraction. Figure courtesy of Peterson and Fabian (2006).

Table 2.1: Selected emission lines

Ion	Wavelength (Å)	Peak formation temperature (MK)
Fe IX	171	0.63
Fe X	177	0.93
Fe XI	180	1.15
Fe XII	195	1.26
Fe XIII	202	1.58
Fe XIV	211	1.86
Fe XV	284	2.19
Fe XVI	335	2.69
Fe XVIII	94	6.46
Fe XX	132	9.33

2.1.8 Thermodynamic Equilibrium

2.1.9 Corona

2.1.10 Heliosphere

2.2 Physics of Solar Eruptive Events

2.2.1 Magnetic Energy Storage

2.2.2 Energy Release Overview

2.2.3 Solar Flares

2.2.4 Coronal Mass Ejections

2.3 Space Weather

2.4 Instrument Descriptions

2.4.1 Spectrographs

2.4.2 Spectral Imagers

2.4.3 Magnetic Imagers

2.4.4 Coronagraphs

2.4.5 In-situ Measurements

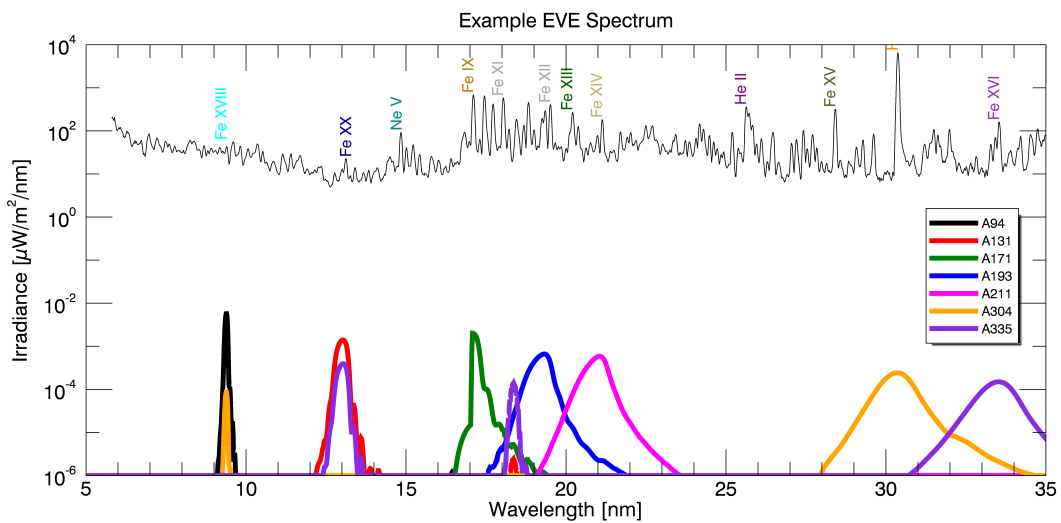


Figure 2.10: AIA bandpasses, model solar spectrum to provide an idea of the amount of blending.

Chapter 3

Mechanisms and Observational Signatures of Coronal Dimming

This chapter details the physics of coronal dimming and the observational signatures that result. There are theoretically many physical processes that can lead to an observer identifying "dimming", but some physical processes have little to do with a coronal mass ejection (CME). Traditionally, the term "coronal dimming" has been assumed to refer to the void left in the corona after a CME departs. This is one cause of a transient hole in the corona and is of the greatest concern to space weather forecasters. However, changing temperatures (common during solar eruptive events) cause ionization fraction shifting, resulting in some emissions dimming while others brighten. Additionally, dark material (e.g., a filament) can pass between a lower bright region (e.g., flaring loops) and the observer, causing a transient dip in emission. Third, solar eruptive events sometimes have associated waves that propagate across the solar disk. These waves are observed as narrow bright fronts with a trailing dark region. The trailing dark region is another way to achieve a transient dimming of emission. Next, there are two ways that Doppler effects can cause transient dips in emission. The first is called Doppler dimming and results from fast moving plasma being sufficiently Doppler-shifted to reduce resonant fluorescence from the solar emission line sources; a phenomenon which is independent of the observation angle. The second occurs if eruptive plasma is moving fast enough in the line-of-sight to shift its emissions outside the bandpass of an observing instrument, which we have named "bandpass dimming". The physics and instrumental identifiers for each of these types of theoretically observable dimming are summarized in Table 3.1 and are discussed in detail in the sections that follow.

Table 3.1: Summary of physical processes that can manifest as observed dimming

Short Name	Physical Process	EVE Full-Disk Observational Identifiers	AIA Imaging Observational Identifiers
Mass loss (Fig. 3.1)	Ejection of emitting plasma from corona	Simultaneous intensity decrease in multiple coronal emission lines, with percentage decrease indicative of percentage mass lost	Area over and near the erupting active region (AR) darkens
Thermal (Fig. 3.2)	Heating raises ionization states (e.g., a fraction of Fe IX becomes Fe X); cooling does the opposite	Heating: Emission loss in lines with lower peak formation temperatures and near simultaneous emission gain in lines with higher peak formation temperatures; vice versa for cooling	Heating: Area near AR darkens in channels with lower peak formation temperature and near simultaneous brightening in channels with higher peak formation temperatures; vice versa for cooling
Obscuration (Fig. 3.5)	Dim feature (e.g., filament material) moves into line-of-sight over a bright feature (e.g., flare arcade)	Drop of emission lines proportional to their absorption cross section in the obscuring material	Direct observation of this obscuration process
Wave (Fig. 3.7)	Wave disturbance propagates globally, causing compression/rarefaction of plasma as wave passes by	No effects have been clearly identified	Direct observation of this wave process, especially apparent with difference movies
Doppler (Fig. 3.8)	Fast moving plasma Doppler shifts away from resonant fluorescence with solar emission lines	Doppler wavelength shift of emission lines and change in intensity, possibly also observed as line broadening	Change in intensity of moving plasma as its velocity changes
Bandpass (Fig. 3.9)	Emissions from fast moving plasma have Doppler wavelength shift	Emission line shifts in wavelength or has broadening	Doppler shift convolves with band-pass sensitivity to cause apparent reduction in emission

3.1 Mass-loss Dimming

The physical process in mass-loss dimming is the eruption of emitting plasma (see Figure 3.1; Harrison and Lyons 2000; Harra and Sterling 2001). It can be a CME (i.e., plasma leaves the sun) or a failed ejection (i.e., plasma rises and then falls back onto the sun), the latter of which still manifests locally as a mass-loss dimming, but does not result in the appearance of a CME in coronagraph data and may not appear in a disk-integrated spectrograph like EVE. The eruption physics model is the standard CME initiation discussed in Section ???. However, where most CME discussions will then follow the CME as it transitions away from the sun into an interplanetary CME, in mass-loss dimming we are instead interested in the details of the void left behind in the corona. The mass of an average CME and a typical active region are of the same order of magnitude: 10^{15} g, meaning that a departing CME can "blow out" a large part of the active region with it (Aschwanden et al., 2009a). This is the physical process assumed to be the main contributor to observed dimming in many recent studies (Sterling and Hudson, 1997; Reinard and Biesecker, 2008, 2009; Aschwanden et al., 2009a). Harrison et al. (2003) showed that dimmings can account for a large percentage of CME mass. Thus, mass-loss dimming is very relevant for the space weather community, who study and forecast CMEs.

Observationally, mass-loss dimming appears in EVE as multiple emission lines dropping nearly simultaneously. In the case of a failed ejection, the dimming area and the ejected material are likely to maintain a total emission that is close enough to constant that it will not be apparent in EVE data. For space weather, this is of little concern since CMEs have far greater geoeffectiveness than short-lived holes in the corona of small spatial extent. However, AIA data allow the identification of mass-loss dimming even if the event is a failed ejection. In either case, mass-loss dimming appears in AIA as a relatively compact area near an active region becoming darker, sometimes with a dark cloud visibly moving off-disk. Assuming the dimmings in Reinard and Biesecker (2008) to all be due to mass loss, the timescale of the process is 3 - 12 hr and rarely persists longer than a day. Additional observations from the Hinode spacecraft have confirmed

density decreases with accompanying outflows (Attrill et al., 2010; Harra et al., 2010; Tian et al., 2012).

3.2 Thermal Dimming

Temperature evolution of emission lines is only interpreted as observed dimming if one is not careful to observe co-spatial emission lines at different peak formation temperatures. As plasma is heated or cooled, the ionization fraction changes, necessarily causing the emission intensity to change (Figure 3.2). For example, heating causes some Fe IX to become Fe X and thus, in the absence of competing physical processes, Fe IX 171 Å emission drops while Fe X 177 Å emission rises. This pattern was identified observationally in Figure 6 of Woods et al. (2011) using SDO/EVE data, Robbrecht and Wang (2010) using STEREO/EUVI, and Jin et al. (2009) and Imada et al. (2007) with Hinode/EIS. It can also be observed in the standard composite (multi-wavelength) movies produced by the AIA team; indeed, this is one of the prime purposes for the composites. The initiation time and duration of temperature evolution tends to be quite similar to mass-loss dimming, as they are typically both responses to the rapid release of magnetic field energy

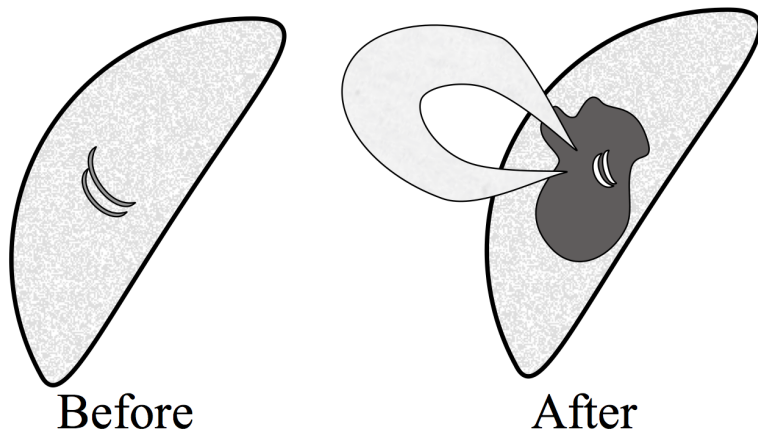


Figure 3.1: Schematic depicting the process of mass-loss dimming. Prior to the eruption (left), coronal loops between two active regions are relatively quiescent. During and after the eruption (right), the loops become brighter and reconfigured, a CME is ejected, and a void forms in the coronal plasma. The post-flare coronal loops usually reform in much the same as the original configuration.

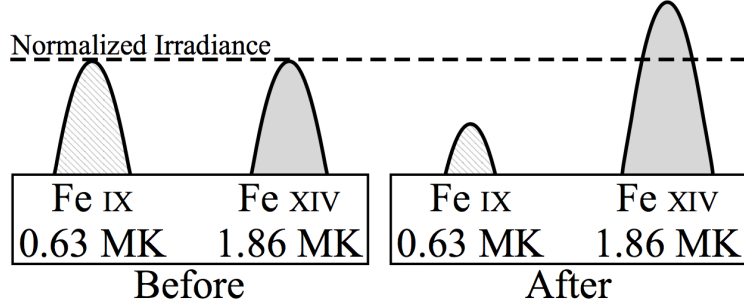


Figure 3.2: Schematic depicting the observational behavior for the thermal dimming effect. Relative to a pre-eruption time (left), the cooler Fe IX emission drops while the warmer Fe XIV emission increases (right) due to heating of the plasma and redistribution of ionization states.

in active regions and require several hours of recovery time. Thus, thermal processes could be mistaken for mass loss if only a single spectral line was observed. Ideally, unblended emission lines from an entire coronal ionization sequence (e.g., Fe I to Fe XVIII) could be used to mitigate this convolution of dimming observations. However, as we will show in Section 4.3, it may be sufficient to have observations of two sufficiently separated ionizations states to differentiate between thermal evolution and mass-loss dimming. This is due, in part, to the fact that hotter lines (e.g., Fe XV and above) are primarily emitted from confined loops near the flare and are thus not strongly impacted by mass-loss dimming.

Multi-wavelength Doppler studies have shown that while all (measured) emission lines become blue-shifted (indicating an outflow), the magnitude of the shift is strongly proportional to the lines peak formation temperature (Imada et al., 2007; Jin et al., 2009). Figure 3.3 shows this dependence for a plage region with a dimming event during an X-class flare. Part of the explanation for this is that as a population of ions is accelerated outward as part of the CME, it is simultaneously experiencing heating as part of the eruptive process. This causes the ionization fraction to shift upward to the point where there may be little low ionization states left e.g., Fe IX. Tracking a single ion, one would see the same nuclei accelerating outward while having electrons stripped away. This explains why lower ionization states seem to have relatively little outflow velocity. Additionally, Fe IX 171 Å emission can be depressed further after open magnetic field lines from the departing CME

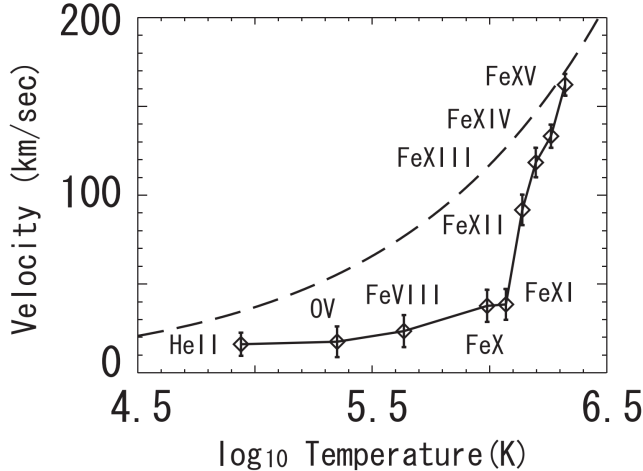


Figure 3.3: Outflow velocity vs emission line peak formation temperature for a dimming region near a plage. Adapted from Imada et al. (2007).

close down and cause another bout of heating; causing e.g., Fe IX to become Fe X and beyond, which propagates outward as a "heat wave dimming" (Robbrecht and Wang, 2010). However, Mason et al. (2014) found that the onset time, slope, and duration of dimming are comparable in SDO/AIA 171 Å and 193 Å¹ and in SDO/EVE 171Å and 195 Å (described in Chapter 4). It should also be noted that EUV images tend to provide higher contrast for dimming in Fe XII 195 Å than Fe IX 171 Å. This is because there is much less Fe XII in the quiescent corona than Fe IX. Therefore, the background in 171 Å images is much brighter, making dimming (which are typically less than a 5% reduction of full-disk emission) more difficult to identify. Nevertheless, we find that for full-disk emission (i.e., irradiance from EVE) the 171 Å emission shows stronger dimming than the 195 Å emission as shown in 3.4.

It is important to note that, in general, the magnitude of total observed dimming in a given line in EVE spectra is inversely proportional to its peak formation temperature, which can be inferred from Figure 3.4. This figure was generated using a simple algorithm that searched all EVE/MEGS-A data for relative irradiance decreases greater than a specified threshold (1%, 2%,

¹ Note that the SDO/AIA 193 Å band encompasses 195 Å

3%) of flares exceeding GOES X-ray class of C1. The window of time searched was bounded by the GOES event start time and the sooner of either 4 hours after the start time or the next GOES event start time. This algorithm was applied to all EVE data from mission start (2010 May 1) to the failure of the MEGS-A detector (due to a shorted capacitor on 2014 April 30). MEGS-A takes the measurements of all wavelengths studied here. Figure 3.4 shows that the number of dimmings dramatically decreases as the magnitude threshold is increased, and decreases slightly with higher peak formation temperature. This latter effect is partially due to flare heating adding emission in the higher temperature, higher ionization state, lines that partially offsets the mass-loss dimming. Additionally, these trends indicate that at sufficiently high peak formation temperature, no dimming may be observed at all, even at the lowest detection threshold, which is consistent with the hotter lines being restricted to the confined flare loops and hence experiencing no mass loss. In other words, the higher the peak formation temperature, the greater the relative contribution of more confined loops to the measured emission.

An instrument with spatial resolution like AIA can be used to isolate the confined flaring loops and create a time series of just the dimming region, and then the sum of those dimming regions can be compared to the EVE full-disk (irradiance) dimming trend. This type of analysis and comparison between AIA and EVE dimming is provided in Chapter 4. AIA too has its own limitations; relevant in this case is the relatively lower spectral resolution that blends together emission from several ionization states of Fe. With EVE and AIA combined, it is possible to analyze thermal dimming but the ideal instrument for fully characterizing this phenomenon would be a high spectral resolution hyperspectral imager in the EUV.

3.3 Obscuration Dimming

The physical process that results in apparent dimming here is material that is dark in a particular wavelength (e.g., a filament) moving between lower-down bright material (e.g., flare arcade) and the observer (Figure 3.5). In optically thick wavelengths, the dark plasma absorbs some of the bright emission, resulting in an apparent decrease in emission. The slow draining of plasma

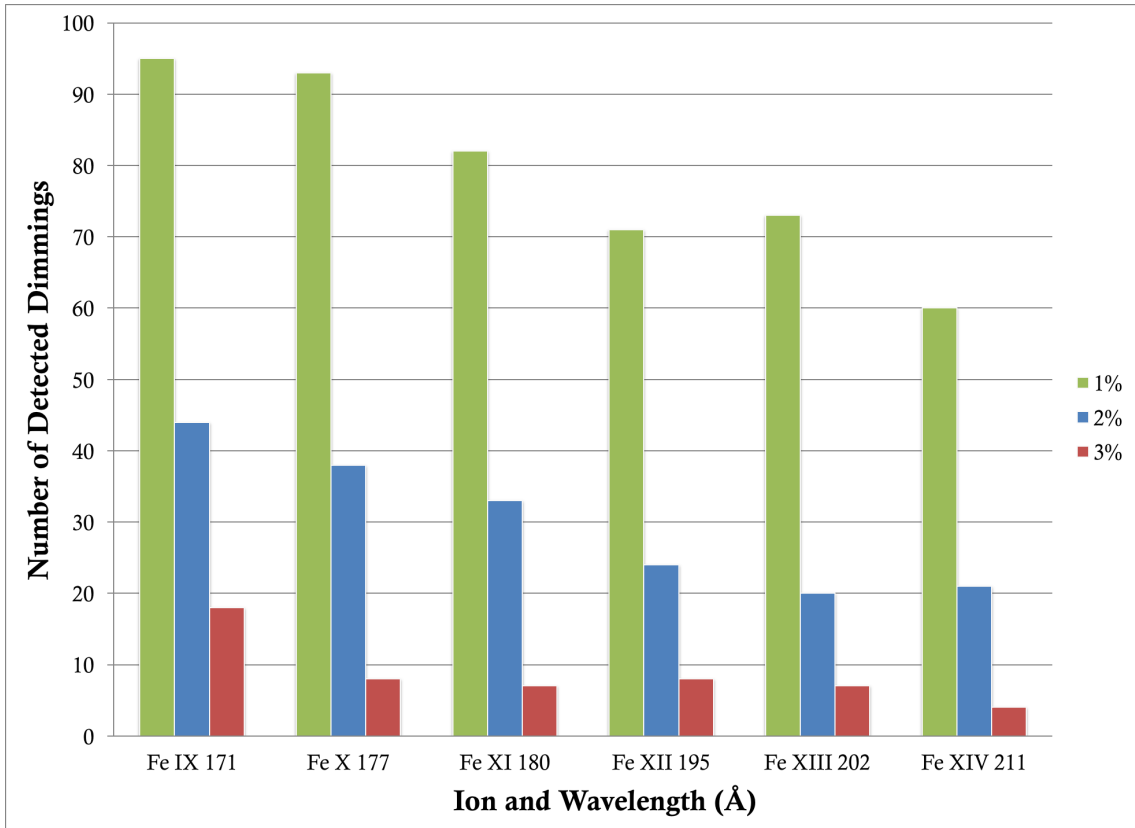


Figure 3.4: Number of identified dimmings in EVE for six spectral lines using different percentage dimming depths as the threshold for a detection. There were 302 flares (\geq M1.0 GOES class) used to trigger an automated search for dimming in EVE. Note the decrease in detections with increasing ionization state (i.e. peak formation temperature).

back to the corona can obscure underlying emission for hours, and absorption can be observed in both coronal and chromospheric lines (e.g., Gilbert et al. 2013). Although obscuration dimmings can exhibit time and spatial scales comparable to the more short-lived mass-loss dimmings, it is fairly straightforward to identify absorption signatures in the EUV images. It may also be possible to identify this phenomenon with EVE using the He II 256 Å and 304 Å chromospheric emission lines and knowledge of the absorption cross-section through filamentary plasma. Figure 3.6 shows the photoionization cross-sections of the dominant species in the solar corona. Hydrogen and helium contribute an order-of-magnitude more absorption than metals², and thus the effect of metals can

² "Metals" in the astrophysical sense

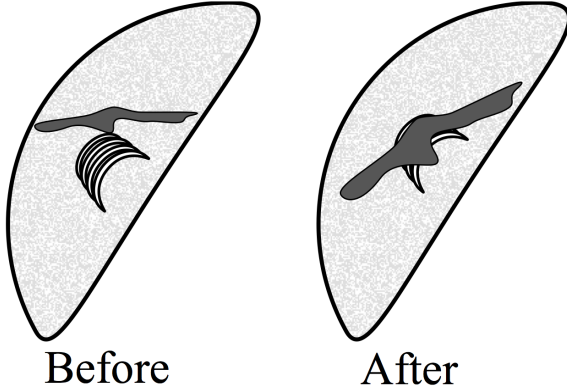


Figure 3.5: Schematic depicting the process of obscuration dimming. A filament previously obscuring only the quiet sun (left) expands and moves in front of a flare arcade (right). This results in a decreased observed emission from the flare arcade in wavelengths where the filament is optically thick.

be ignored. The cross-sections are quite steep in the wavelength range of interest here (roughly 150-310 Å). This means that approximately twice as much He II 256 Å than He II 304 Å emission will come through a filament. Furthermore, the mass-loss dimming sensitive lines (e.g., Fe IX 171 Å and 195Å) will be less affected by this obscuration, but a 1% effect would be sufficient to cause a "false" detection. It may be possible to identify obscuration dimming with EVE's 256 Å and 304 Å measurements and determine that an obscuration dimming has occurred. However, further analysis of this type of dimming is required before any conclusions can be drawn.

3.4 Wave Dimming

The debate about the physics of coronal EUV waves continues (e.g., Zhukov and Auchère 2004; Muhr et al. 2011; Liu and Ofman 2014) but one of the simplest explanations of the observations is that plasma is compressed as a longitudinal wave passes through the medium. Traveling (i.e., not static) rarefactions are sometimes observed following the compression (Muhr et al., 2011), the compressed regions having higher densities resulting in increased emission, and vice versa (Figure 3.7). Alternatively, some models suggest that the observed phenomenon is not a wave at all, but rather the impact of the CME departing on the global magnetic field (Chen et al., 2002,

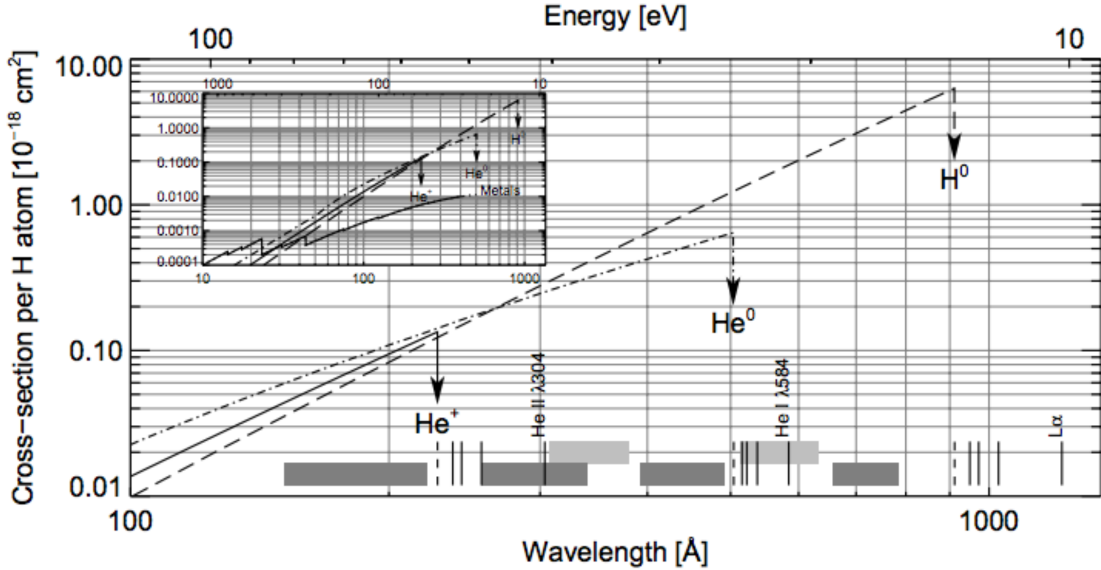


Figure 3.6: Photoionization cross-sections for He I (dot-dashed line), He II (solid line), and H (dashed line) per hydrogen atom. The inset shows a wider wavelength range of the same data but with metals shown for comparison. The dashed vertical bars at the bottom indicate the edges of respective continua. The grey regions at the bottom are not pertinent here as they correspond to specifics of the SOHO/CDS instrument. Adapted from Andretta et al. (2003).

2005). Regardless of the physical process responsible, the observation is the same. The EUV waves emanating from an eruption can be seen to cause dimmings and brightenings elsewhere in the solar EUV images, often starting at the eruption site and then seen later very far from the original eruption site, particularly near other active regions. We refer to these dimmings that are non-local to the erupting site as sympathetic dimmings (Schrijver and Higgins, 2015). This is quite likely to occur if a distant active region has significant potential energy stored when the disturbance reaches it – the wave propagating across the magnetic field lines acts as a catalyst.

It is important to distinguish between the wave-caused dimmings and other causes of remote dimming, such as large-scale disappearing loops that are visible in soft X-ray images but only have visible EUV changes at their footpoints (Pohjolainen et al., 2005). EUV wave dimmings are unlikely to be easily identified in full-disk spatially-integrated instruments like EVE because the enhanced emission nearly cancels out the dimmed emission when summed.

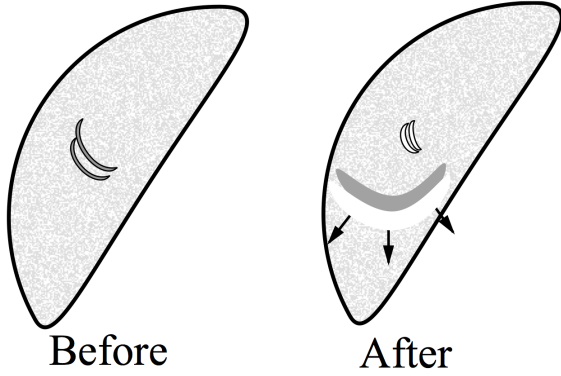


Figure 3.7: Similar to Figure 3.5, but depicting the process of wave dimming. After an eruptive event, a wave propagates and expands through the corona. The compressed plasma of the wavefront results in enhanced emission, while the rarefied trailing region is dimmed.

3.5 Doppler and Bandpass Dimming

Two additional processes can theoretically lead to the observation of dimming in a limited wavelength range and both result from Doppler effects. The first has been given the name "Doppler dimming". In this type of dimming, resonant fluorescence of a high-velocity, remote cloud of plasma (e.g., CME) by a source population (solar emission lines) can decrease as the resultant Doppler shift becomes sufficiently large (see Figure 3.8; Hyder and Lites 1970). Here, Doppler takes effect due to the relative velocity between the source (the sun) and the scattering medium (the CME) and is thus independent of observer angle. This phenomenon has been known for decades for cometary emissions (Swings, 1941; Greenstein, 1958) and has been documented in chromospheric lines associated with eruptions (Labrosse and Mcglinchey, 2012) as well as in coronal lines such as O VI for polar coronal hole outflows (Giordano et al., 2000). However, the majority of EUV emission lines in the corona are collisionally dominated i.e. not resonantly excited, and will not exhibit this effect. Furthermore, the dimming region is the CME itself, which is likely to be outside the field of view of EUV instruments observing the solar disk. Therefore, it is possible to diagnose this type of dimming when it is pronounced in resonantly excited lines but does not manifest in the lines of interest studied herein.

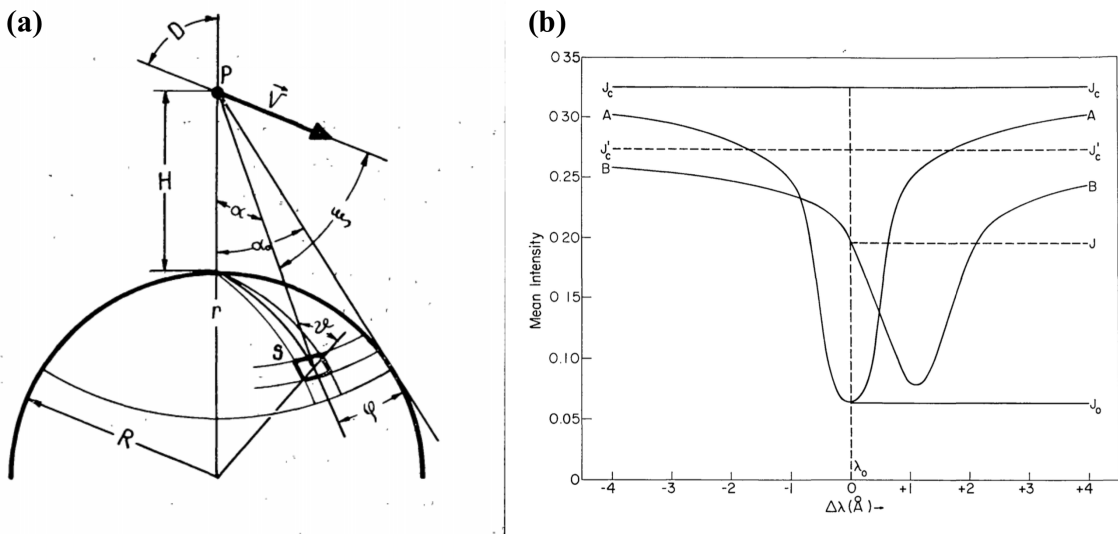


Figure 3.8: (a) Geometry of Doppler dimming. The large circle at the bottom represents the sun, the point P represents the position of mass that has erupted e.g., a CME. The vector V is the velocity of the CME. The square patch on the sun represents an area of source emission. Adapted from Rompolt (1967). (b) The H α profiles seen by (A) a stationary observer at a height of 5600 km above the photosphere; and (B) an observer at a height of 30,000 km moving radially outward at 75 km s^{-1} . The mean intensity (as seen by the scattering medium) is measured in units of the intensity of the nearby continuum at the center of the disk. It can be seen that the Doppler shift also causes an intensity decrease. Adapted from Hyder and Lites (1970).

The second type of dimming that results from a Doppler effect is one we call “bandpass dimming”. This physical process is tied to the observers location similarly to obscuration dimming (see Section 3.5). Mass ejected toward the observer will have emissions that are necessarily blue-shifted. If the velocity is high enough, it can shift emission lines outside of an imager’s bandpass, causing an apparent dimming in the data. Most imagers use filters that tend to have bandpasses on the order of nanometers but can have sharp edges (Figure 3.9). CMEs typically have speeds ranging from a few hundred to a couple thousand km s^{-1} . However, a CME only accounts for a small fraction of the total emission from the solar disk. As noted in Hudson et al. (2011), these Doppler shifts tend to be on the order of picometers. Additionally, a CME moving fast enough to shift emission outside the bandpass would be outside the field-of-view of the instrument in a very short time. Thus, this type of apparent dimming is not expected in EUV images, but we include

it for completeness and note that this may be a consideration for designing future instruments.

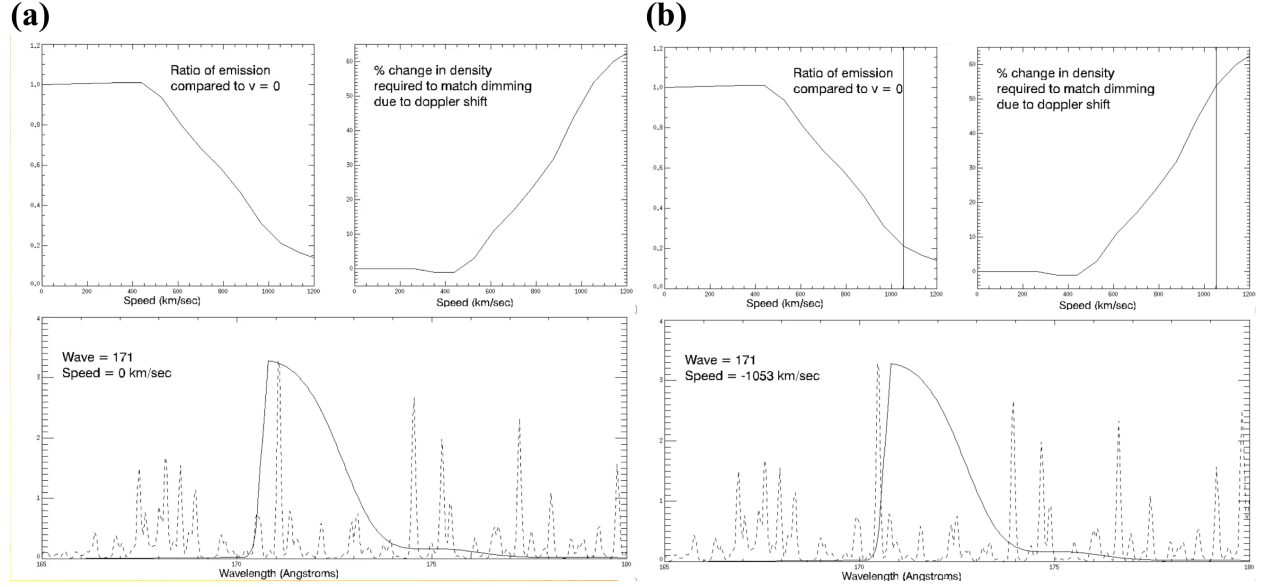


Figure 3.9: Spectra to illustrate bandpass dimming, taken as snapshots from a movie produced by Barbara Thompson. (a) Bottom: The dashed line shows a modeled solar spectrum and the solid line shows the bandpass for AIA's 171 Å. Top left: The ratio of emission relative to plasma with no line-of-sight velocity as a function of velocity. Top right: The amount of density decrease (in %) that would be required to achieve the same amount of dimming as bandpass dimming at each velocity. (b) Same as (a) but at a velocity of 1053 km s^{-1} , which is an example of the 171 Å emission Doppler shifting outside the associated AIA bandpass.

In a spectrograph like EVE, the Doppler shifts would instead simply cause a wavelength shift of the emission line from the ejected material, which is how Hudson et al. (2011) performed their Doppler analysis of the EVE data. When this Doppler-shifted emission is convolved with the relatively static plasma remaining on the sun, a small Doppler shift from the ejected material manifests as line-broadening in the integrated irradiance while a large shift would result in a line splitting. It should be noted that the EVE extracted lines data product applies a static mask to the spectra so a sufficiently large Doppler shift could cause an apparent dimming in this product. Again, the observed shifts are far too small to impact the EVE data analysis.

3.6 Dimming Physics and Observations Summary

The physics for most of these types of dimming is relatively simple and well-understood, with the exception of global waves. Mass-loss dimming is simply the direct result of a CME removing a significant quantity of emitting material from the solar corona. The coronal dimming amount increases as the CME pulls away, reaches a maximum dimming depth, and then the emission begins to return to the original pre-flare level after a few hours as post-flare loops begin to replace the lost plasma from the surrounding corona and transition region. Instrumentally, even though EUV measurements select specific temperature ranges, mass-estimates based on them appear consistent with white-light coronagraph derived masses (Aschwanden et al., 2009a).

Thermal dimming is a major concern in nearly all of the citations above for its potential to interfere with mass-loss dimming analysis and the resultant estimated CME masses. The physics here is also simple: eruptive events result in various forms of heating (see Section ??) that shift upward the ionization fraction of dominant EUV emitters (e.g., Fe). Instrumentally, this effect can be compensated for by measuring emission lines from multiple ionization states of the same ion (e.g., Fe IX-XV).

Obscuration dimming physics are also simple, essentially a result of Beer's law, as light passes through a medium with nonzero opacity. Instrumentally, this is easily identified with imagers and we believe it may be possible to identify with a spectrograph, provided some chromospheric helium emission lines are measured (e.g., 256 Å and/or 304 Å).

The physics of global waves is highly contested but the observations are well established. For a disk-integrating spectrograph like EVE, which is the primary source of data analysis herein, we believe that wave dimming will be negated by wave brightening. Indeed, to our knowledge, no observations of waves have been detected from EVE observations.

Doppler dimming physics are well understood and long standing. A CME may fluoresce due to stimulation from the sun, but the wavelengths will be Doppler shifted according to the relative velocity of the CME from the sun. This shift reduces the efficacy of the stimulation, resulting in

less fluorescence. However, the dimming region in this case is the CME itself, which is likely to be outside the field of view of instruments like AIA and EVE. Additionally, the emission lines of interest in this study are collisionally dominated. Thus Doppler dimming is an interesting phenomenon but is not expected to dramatically impact analyses of the other types of dimming.

The physics of bandpass dimming is simple Doppler shifting of an emitting plasma. Potential dimming in this case is primarily an instrumental effect, as the Doppler shift could push important emission lines outside the instruments bandpass or data processing line-selection masks. However, studies have shown that the actual Doppler shifts are orders of magnitude too small to cause this type of dimming.

Chapter 4

Coronal Dimming Case Studies

This chapter focuses on the detailed analysis of two coronal dimming events. One was selected for its relative simplicity, involving only mass-loss dimming and some thermal effects, while the other was selected for its complexity, involving nearly all of the types of dimming as described in Chapter 3. Observations and analysis of the EUV irradiance and images of these events as well as the related coronagraphs are first described in Section 4.1. A new method for deconvolving flare emission from dimming irradiance measurements is developed in Section 4.2 while Section 4.3 contains the associated error propagation. Finally, Section 4.4 provides analyses spanning the observations of these two coronal dimming events and parameterizes dimming into depth and slope. We find that the new flare-dimming deconvolution method for irradiance successfully matches the dimming profile extracted from the spatially-isolated dimming as obtained from EUV image time series for the simpler dimming case. Thus, we show that it is possible to accurately characterize dimming in a localized area even with no spatial resolution, i.e., with irradiance. The preliminary analysis of the more complex dimming case is provided here, but further analysis of the complex dimming case for the full-range of cotemporal dimming processes will be a topic of postdoctoral research.

4.1 Observations and Analysis

4.1.1 Simple Dimming Case

This event occurred on 2010 August 7 at approximately 18:24 UT. The eruptive event consisted of an M1.0 flare, dimming in the region around the flare, and a coronal mass ejection (CME). Other, relatively distant, active regions were also on disk but did not have any significant sympathetic eruptive responses as is sometimes seen. Mass-loss dimming and flare-related thermal effects were found to be important, while the other types of dimming (see Chapter 3) were negligible.

Coronagraph Observations

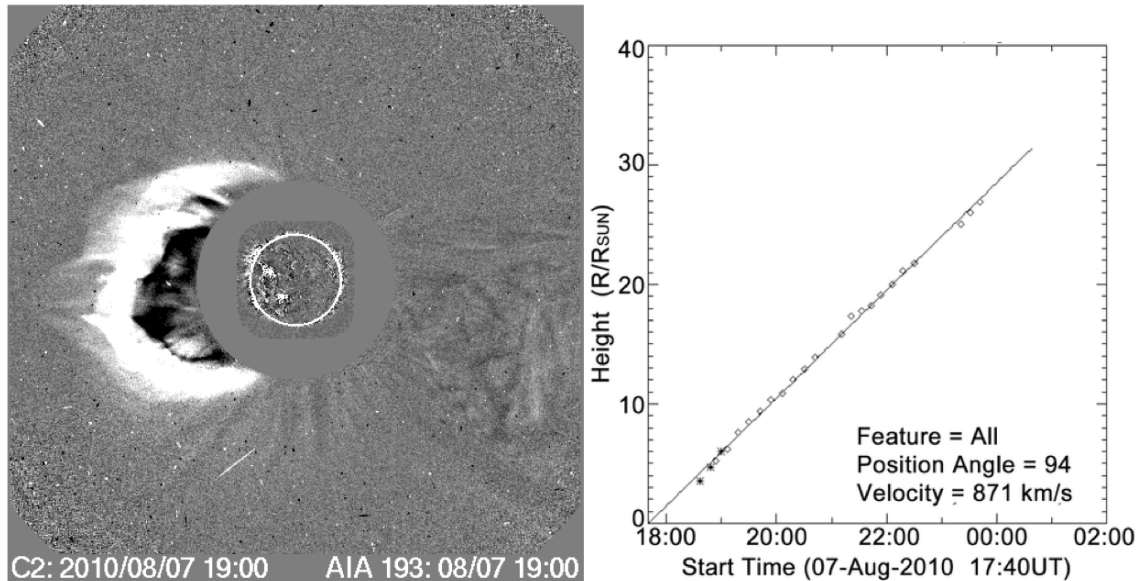


Figure 4.1: CME event at 19:00 on 2010 August 7. Left: difference image from LASCO C2 and AIA 193 Å channel. Right: CME height versus time shows nearly linear velocity of 871 km s^{-1} . Figure adapted from CDAW CME Catalog, courtesy of S. Yashiro and N. Gopalswamy.

The Coordinated Data Analysis Workshops (CDAW) LASCO CME catalog (herein referred to simply as the CDAW catalog) is an extensive database of all CMEs observed by the SOHO/LASCO coronagraphs with related quantities such as date, time, computed velocity, and sometimes mass (Gopalswamy et al., 2009). The CDAW catalog has seven CME events listed for 2010 August 7. All but two of them occur prior to the M1.0 flare at 18:24 UT that is of primary interest for the

simple dimming case study. This rules out all but those two to be CMEs associated with the M1.0 flare. The CME shown in Figure 4.1 is flagged as a halo event with a time of 18:36 UT in CDAW, while the next event occurred with a central position angle of 116° at 22:24 UT. The timing and location of the flare and associated dimming region suggest that the halo CME is the one associated with the dimming. The plane-of-sky velocity estimate for this CME is 871 km s^{-1} as indicated in Figure 4.1. No mass is listed for this CME in CDAW, but using LASCO and STEREO data and the techniques outlined in Colaninno and Vourlidas (2009), a mass of $6.4 \times 10^{15} \text{ g}$ was computed for this CME event (A. Vourlidas 2014, private communication). A “true space” velocity was also computed as 850 km s^{-1} at 9 R_\odot with a deceleration of 6.84 m s^{-2} (Figure 4.2). True space in this context means that the viewpoints from multiple angles were used to determine the actual 3-D vector of propagation; a single viewpoint has inherent uncertainty in the propagation angle because there are too many free parameters to fully constrain it. Based on these estimates for mass and velocity, this CME is considered be of modest size.

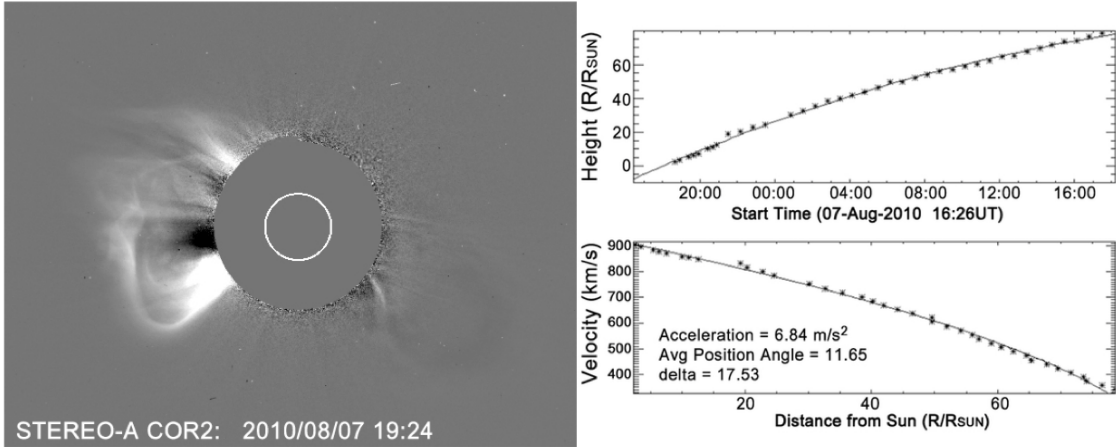


Figure 4.2: Left: STEREO-A COR2 difference image at 19:24 UT. Right: CME height vs. time calculated from STEREO and shows a deceleration of 6.84 m s^{-2} . Figure courtesy of Barbara Thompson.

SDO/AIA EUV Image Observations

The relative simplicity of this event is why it was chosen for a case study. The observations in AIA do not suggest that obscuration, waves, or Doppler shift contributed to the observed dimming. The area in the red contour of Figure 4.3 was

selected manually (by eye) to represent the region of mass loss. Pixel values inside each contour were summed and a time series of these sums created with successive images in multiple AIA wavelength bands. These light curves are shown on the right of Figure 4.3. The light curve for the red contour shows clear dimming in 193 Å and 171 Å. In fact, the dimming from this region accounts for nearly all of the observed dimming throughout the entire event. This contour was selected after several iterations that indicated slight deviations in the contour had minimal impact on the light curve, as long as the dark region was fully encompassed. In other words, the result is fairly insensitive to the precise contour selection. The other contours were also selected manually to isolate regions of potential dimming e.g., as a sympathetic response from the solar eruptive event of interest. The exception is the magenta contour surrounding the flare loops that brightens dramatically but does not ever dim.

The He II 304 Å light curves are included to provide a contrast to the dimming effects seen in the coronal Fe lines. This He II wavelength is generated primarily in the chromosphere and transition region, as opposed to the coronal source of the other EUV wavelengths. Mass loss occurs primarily in the corona, as the term coronal mass ejection suggests. This is reflected in the lack of dimming observed in the non-coronal He II 304 Å emission line.

Thermal effects may play a role in this event but may be difficult to quantify using only AIA because the relatively wide spectral bands of AIA channels mean many emission lines and continuum are blended together (see Figure 2.10 and Table 2.1), which makes specifying a well-defined temperature difficult. Nevertheless, some indication of temperature is given by AIA and multi-wavelength composites can aid in this analysis. Figure 4.4 shows AIA composite images (211 & 193 & 171 Å) before the solar eruptive event and during the dimming. All of these bands correspond primarily to the cool corona and transition region. If an area is dark, that means that there is little emission in all three of these wavelengths. Because these three bands span a broad range of temperatures from 0.6 MK to 1.86 MK, having all three dim at the same time means it is not a thermal dimming case but is instead indicative of mass loss dimming. In areas where temperature effects are very strong, e.g., heating in the confined flare loops, it can be seen that

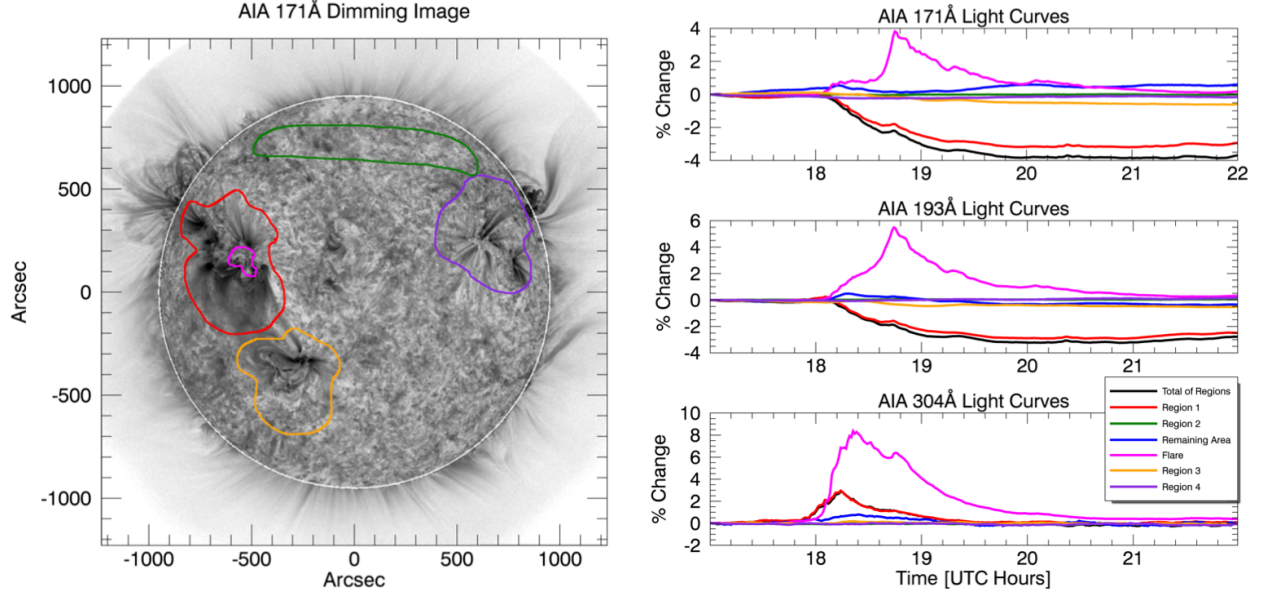


Figure 4.3: AIA results for the M1.0 Flare on 2010 August 7. Images improved by using point spread function to compensate for instrument “blurring” of light. Left: AIA 171 Å channel difference image with subjectively selected region contours overlaid. The red contour outlines what is thought to be the region of mass loss. The orange and purple contours outline other active regions on the disk, which have the potential to have sympathetic eruption/dimming. The green contour outlines a filament, which also has the potential to sympathetically dim based on its behavior during the M flare on 2010 August 5. The magenta contour isolates the flaring coronal loops. The white line around the solar limb is an artifact of the solarsoft de-rotation method. Right three plots: light curves of AIA 171 Å, 193 Å, and 304 Å channels for the color-corresponding contours on the AIA image. The blue line is the light curve for all on-disk area not enclosed by a contour. The black line is the sum of all contoured regions (excluding the magenta flaring region) and acts as a proxy for total dimming. All percent changes are calculated from the band’s pre-flare value at 17:00 UT. The transition region He 304 Å emission does not show dimming; both cool corona Fe emissions (171 Å and 193 Å) show dimming.

emission is strong in all three of these bands resulting in the composite being white near the active region. Even though the flare loop region is also where the highest ionization states and their emissions can be found, there is still ample emission in these relatively low ionization states of Fe. Thus, it's unlikely that a region in these composites would become dark purely from a temperature change. EVE is less sensitive than AIA to blending in temperature space due to its higher spectral resolution and plethora of emission lines from Fe at different ionization states. A future study using the differential emission measure techniques of Caspi et al. (2014) to study the temperature

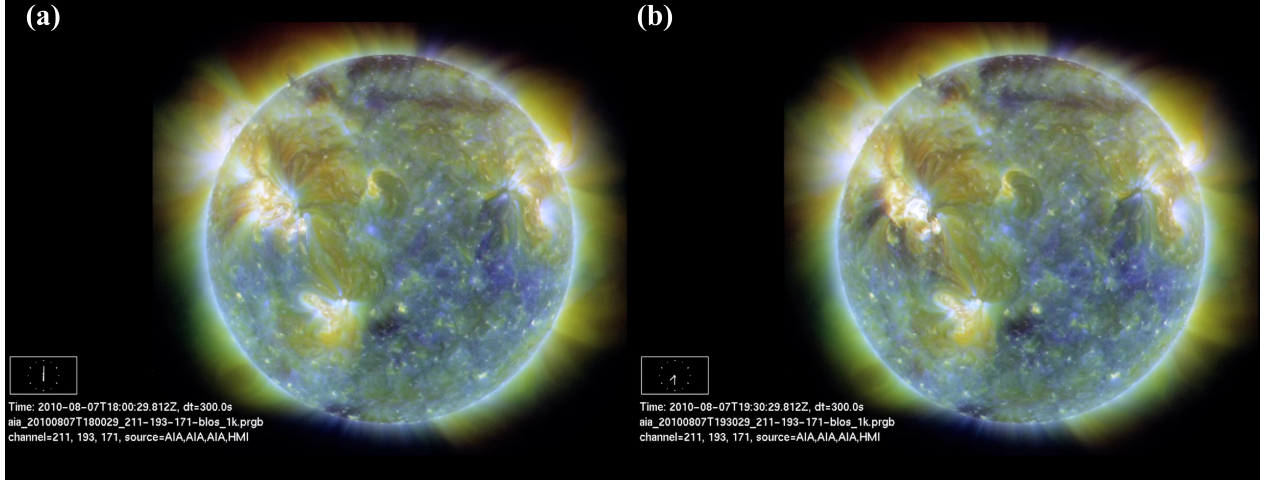


Figure 4.4: AIA composite images (a) prior to solar eruptive event and (b) during deep dimming. In these images, purple is 211 Å, brownish-gold is 193 Å, and yellow is 171 Å. These static images show dimming in the region as outlined in Figure 4.3, though the change is much more dramatic and obvious when viewed as a movie ([link](#)).

evolution could help to quantify this effect.

SDO/EVE EUV Irradiance Observations Figure 4.5 shows a trend that is consistent with the findings from Figure 3.4: that an ion’s peak formation temperature¹ is inversely proportional to magnitude of dimming. The transition from an ionization state that shows dimming to ones that only show brightening occurs at Fe XIV 211 Å, which itself shows dimming in some events but not others. The transition for where the Fe emission shows dimming varies by solar eruptive event. For example, the Fe XVI 335 Å emission has shown dimming for larger CME events (Woods et al., 2011). Herein, we will refer to Fe IX 171 Å through Fe XIV 211 Å as “dimming lines” and Fe XIV 211 Å through Fe XXIV 192 Å as “non-dimming lines” based on examining many dimming events. Note that 211 Å emission line is included in both descriptions to reflect its ambiguity for different eruptive events.

It is also important to note in Figure 4.5 that the onset of dimming in the dimming lines is nearly simultaneous. Meanwhile, the gradual-phase flare peak is delayed in lower ionizations of

¹ Recall that greater ionization requires greater energy and that temperature is one measure of energy content for a Maxwellian plasma

Fe, which is due to a cooling effect. The primary source of energy release in a flare is near the point of magnetic reconnection, typically far above the footpoints of the magnetic loops involved, in the corona. Some of the energy goes into the acceleration of particles downward. When these particles impact the denser chromosphere, they cause heating and chromospheric evaporation. As that thermal plasma enters the corona it cools (Fletcher et al., 2011), and highly ionized Fe gains electrons (radiative recombination) as the primary primary cooling process. Thus, the peak is later for lower ionization states as the hot, highly-ionized Fe ions cascade down to cooler Fe ions for this case (see Figure 4.5). This process is typical for most flare events. The Fe IX 171 Å irradiance, in particular, shows the competing effects of this gradual phase flare peak and coronal dimming: it's irradiance begins to drop at the same onset as the other emission lines, then has a positive peak of about +2%, and drops to a dimmed condition again. Images with spatial resolution can isolate the flaring region responsible for this peak, as is shown with the magenta contour in Figure 4.3. Alternatively, we have developed a method for isolating and removing this peak in dimming lines with the spatially-integrated irradiance from EVE, which will be detailed in Section 4.2.

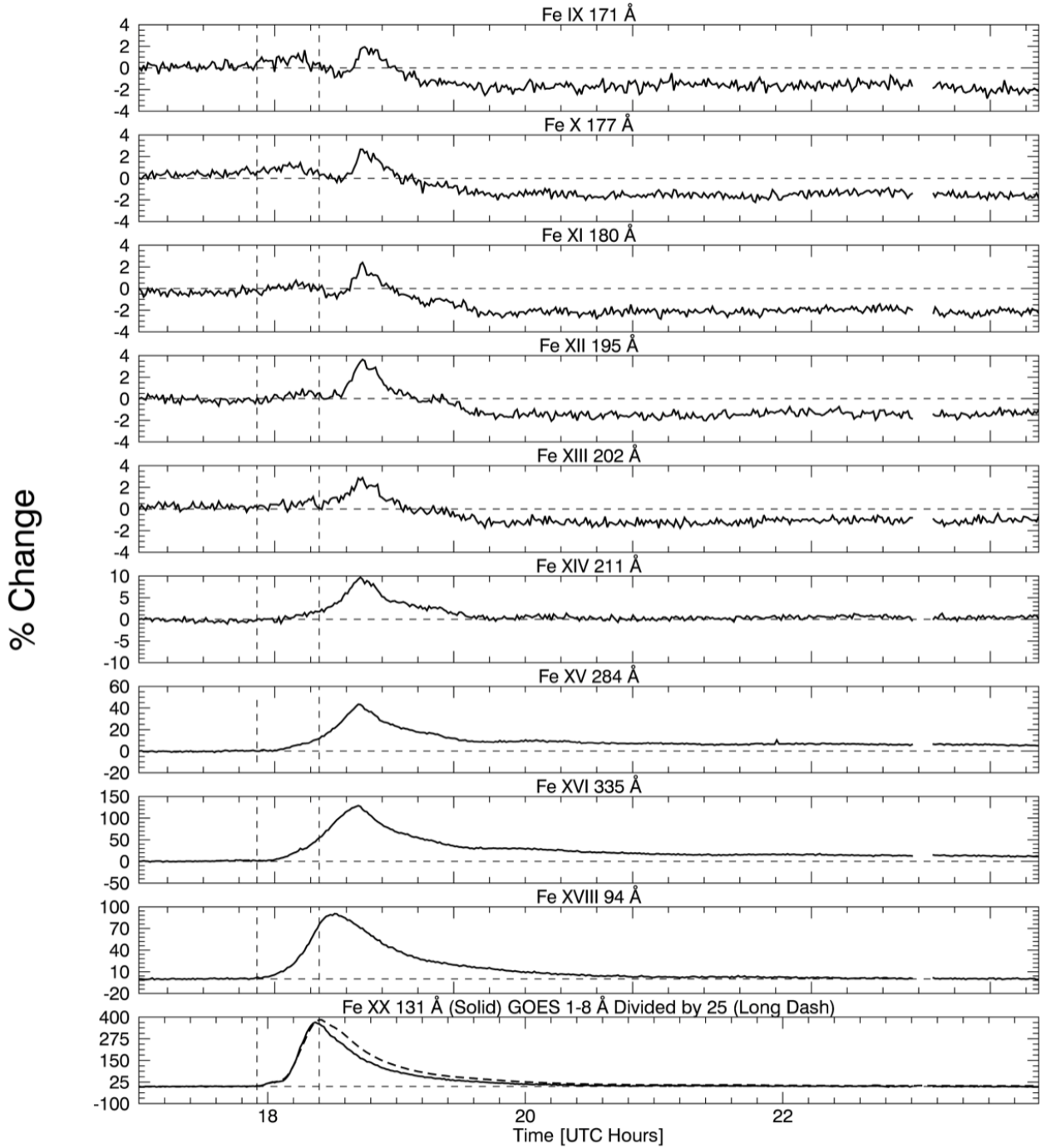


Figure 4.5: One minute average EVE light curves of the 2010 August 7 coronal dimming event for most of the spectral lines listed in Table 2.1, as well as the GOES 1-8 Å channel light curve. The leftmost vertical dashed line indicates the GOES event start time, while the other vertical dashed line indicates the GOES event peak time. Peak formation temperature of the EVE spectral lines increases from top to bottom plot. Fe IX to Fe XIII show clear dimming, Fe XIV is borderline, and Fe XV to Fe XX show smooth brightening with no dimming. The Fe XX 131 Å profile is very similar to GOES 1-8 Å, indicating that this line in EVE is a good proxy for gradual phase timing. Also note the vertical axes: dimming is on the order of a few percent for the cooler Fe emissions while the hotter Fe emissions have bright peaks in the hundreds of percent. All percent changes are calculated relative to the pre-flare irradiance at 17:00 UT.

4.1.2 Complex Dimming Case

This event occurred on 2011 August 4 at approximately 3:47 UT. It spawned from NOAA active region 11261 at location N19W36. The eruptive event consisted of an M9.3 flare, a large and fast CME, and nearly all of the types of dimming discussed in Chapter 3: mass-loss and thermal dimming, a global wave that then triggered a sympathetic filament eruption, and an obscuration dimming from the nearby filament. No bandpass or Doppler dimming were identified even in this relatively energetic event. This event was chosen specifically for presenting so many types of dimming and related physical processes in a single case.

Coronagraph Observations

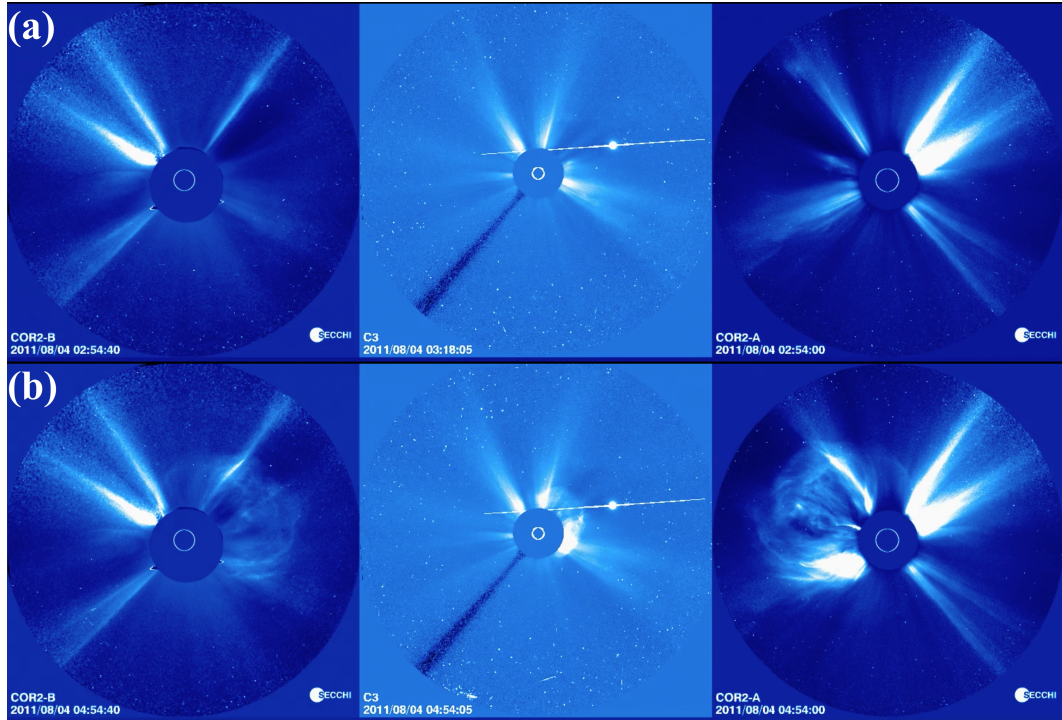


Figure 4.6: Coronagraph images of CME associated with 2011 August 4 dimming event. From left to right the coronagraphs are STEREO Behind C2, LASCO C3, and STEREO Ahead C2. Top: Images prior to CME. Bottom: Images during CME.

Images from the three coronagraphs are shown in Figure 4.6. The CME in Figure 4.6 (b) can be seen in STEREO-B (behind) on the right of the solar disk, in LASCO as the start of a

halo CME offset to the upper-right of the disk, and in STEREO-A (ahead) on the left of the disk. Additionally, bright streamers can be seen inside the CME and on the opposite side of the Sun, signifying that the outer corona of the Sun was also in a more complex configuration than the 2010 August 7 case.

The CDAW catalog for this event lists it as a halo CME with a velocity of 1315 km s^{-1} , relatively fast for a CME (faster than 99.03% of other CMEs, see Figure 4.7), and a mass of $1.16 \times 10^{16} \text{ g}$. However, halo CMEs present a strong challenge for obtaining accurate mass, and the catalog flags it as a poor mass estimate. Mass estimates based on the three coronagraphs are $8.6 \times 10^{15} \text{ g}$ for LASCO C3 (35% lower than the CDAW value), $7 - 8 \times 10^{15} \text{ g}$ for STEREO-A COR2, and $4.3 \times 10^{15} \text{ g}$ for STEREO-B COR2 (A. Vourlidas 2013, private communication). A deprojected, 3-D analysis has not been performed for this CME.

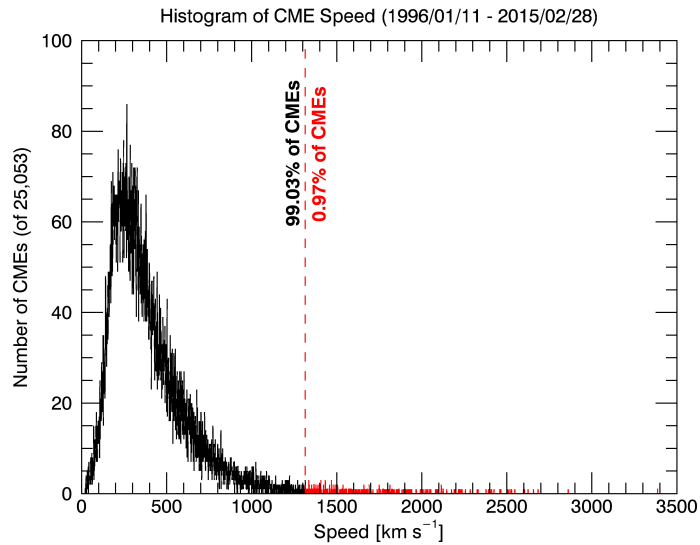


Figure 4.7: Histogram of CME speed from 1995 to 2015 based on the CDAW LASCO CME catalog's 25,053 CMEs with listed speeds. The red vertical line is at 1315 km s^{-1} , the listed speed of the 2011 August 4 event.

SDO/AIA EUV Image Observations

The complexities of this eruptive event are quite apparent in AIA observations. Figure 4.8 is

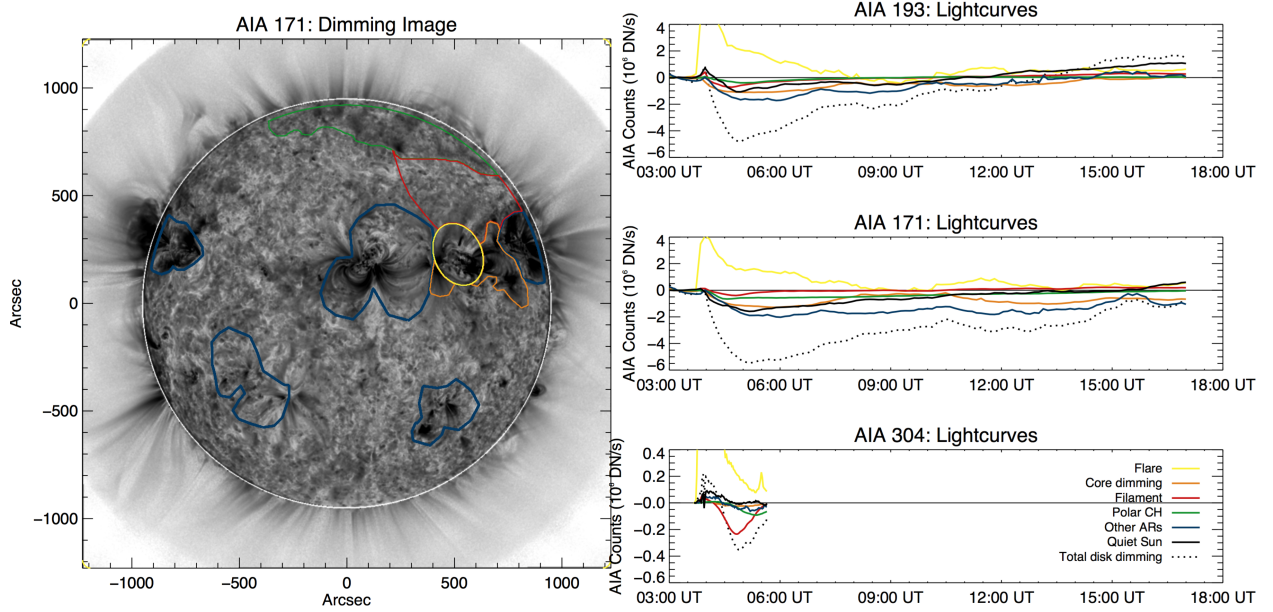


Figure 4.8: Same as Figure 4.3 but for 2010 August 7 event. Colored contours and lines in plots correspond according to legend, but are different from Figure 4.3. An additional difference is that the He II 304 Å line now shows dimming. Not all 304 Å data were available at the time of processing, which is why the time series ends at 6:00 UT. Figure courtesy of Rachel Hock.

in the same format as Figure 4.3 but is for the 2011 August 4 event. Dimming is seen in numerous locations for this event, indicating the far-reaching influence of this eruption. In particular, even though 304 Å data were not processed to the end of the dimming window², the main phase of obscuration dimming is clearly visible. Additionally, 193 Å and 171 Å show dimming in every region outside of the flare-isolating contour (yellow). The primary region thought to be associated with mass-loss dimming is labeled “core dimming” (orange) here. It corresponds to an area immediately surrounding the active region where the flare took place and is bounded by quiet-Sun on top and bottom and other active region loops to the left and right. All other active regions visible on disk are contained in blue contours and eventually show even greater dimming than the core region (orange). Note that for the first several minutes, the core dimming dominates the other active regions. Also, the dotted black dash line is the disk signal excluding the flare region (yellow),

² Figure 4.9 shows these data in full, though for differently selected contours

effectively the sum of all plotted lines except yellow. It can be seen that the relative contribution of each region to the total dimming is nonzero. Table 4.1 details these contributions.

The overall structure of Table 4.1 is wavelength and feature (vertical) and contribution at maximum dimming (i.e. minimum count), maximum dimming contribution, and the range of contributions. It can be seen that in 193 Å and 171 Å, peak dimming is dominated by the non-flaring active regions. As will be shown later, this is mainly a reflection of dimming from the nearby active region. It is also worth noting that core dimming reaches its maximum dimming 36 minutes earlier than the dimming from non-flaring active regions. This suggests that the latter is either a sympathetic response to the primary dimming catalyzed by the global wave or additional mass being ejected that becomes the tail side of the CME. As expected, in 304 Å, the minimum count is dominated by obscuration from the nearby filament (red). This is consistent with the physical theory for obscuration dimming detailed in Section 3.5. The dominant region changes when looking at the maximum contribution. Here, the core dimming region dominates for 193 Å but the non-flaring active regions dominate the dimming in 171 Å. Again, we will soon show that the most nearby active region contributes greatly to the dimming and may have contributed to the outgoing mass of the CME. The 304 Å dimming is similar in timing to the core dimming region evolution, and AIA 304 Å movies confirm that the maximum dimming is coming from the filament eruption and resultant obscuration for the 304 Å emission. In summary, different spectral emissions have maximum dimming at different times because their main contributions are from different dimming regions. In particular, the 193 Å emission is primarily from the core dimming region; the 171 Å emission has greater contributions from non-flaring active regions and the quiet-Sun; and the 304 Å emission is very clearly dominated by obscuration from the filament.

Figure 4.9 is the same format as Figure 4.8 but with different regions selected, and does not use images corrected with the point spread function. The latter explains why the total dimming is about 2% less than in Figure 4.8; in other words, the application of the point spread function correction for AIA images is important for dimming studies. Of importance for this comparison is that the red contour, which encompasses the core dimming region from Figure 4.8 and the most

Table 4.1: Statistics for dimming features in Figure 4.8 for 2011 August 4 event. Table courtesy of Rachel Hock.

Dimming Feature	Time (UT)	Count Counts ($10^6 DN s^{-1}$)		Contribution (%)	Time (UT)	Contribution Counts ($10^6 DN s^{-1}$)		Contribution (%)	Range of Contribution (%)
		Minimum	Maximum			($10^6 DN s^{-1}$)	($10^6 DN s^{-1}$)		
AIA 193:									
Total disk dimming	4:55	-4.81	-						
Core dimming	5:17	-1.11	25.3	04:05	-0.63	73.1	18.9-	73.1	
Filament eruption	4:41	-0.72	16.2	04:05	-0.23	27.2	1.0-	27.2	
Polar coronal hole	5:03	-0.39	8.5	05:17	-0.38	8.7	0.6-	8.7	
Non-flaring active regions	5:53	-1.72	43.1	08:04	-1.05	54.6	29.6-	54.6	
Quiet Sun	4:55	-1.07	22.3	08:40	-0.57	26.0	8.0-	26.0	
AIA 171:									
Total disk dimming	5:10	-5.46	-						
Core dimming	5:53	-1.28	24.5	04:05	-0.40	27.3	9.4-	27.3	
Filament eruption	4:48	-0.40	8.0	04:41	-0.38	8.1	0.0-	8.1	
Polar coronal hole	4:34	-0.66	15.7	04:26	-0.63	16.6	7.5-	16.6	
Non-flaring active regions	6:00	-2.02	38.9	08:54	-1.72	53.9	16.6-	53.9	
Quiet Sun	5:10	-1.59	29.0	04:05	-0.68	46.7	20.8-	46.7	
AIA 304:									
Total disk dimming	4:53	-0.36	-						
Core dimming	5:08	-0.03	9.5	04:23	-0.02	62.2	7.4-	62.2	
Filament eruption	4:49	-0.24	69.4	04:25	-0.08	304.3	9.4-	304.3	
Polar coronal hole	5:22	-0.09	40.0	05:38	-0.06	49.3	1.1-	49.3	
Non-flaring active regions	5:11	-0.06	20.6	05:31	-0.05	25.1	2.4-	25.1	
Quiet Sun	5:34	-0.02	14.0	05:37	-0.02	14.4	0.1-	14.4	

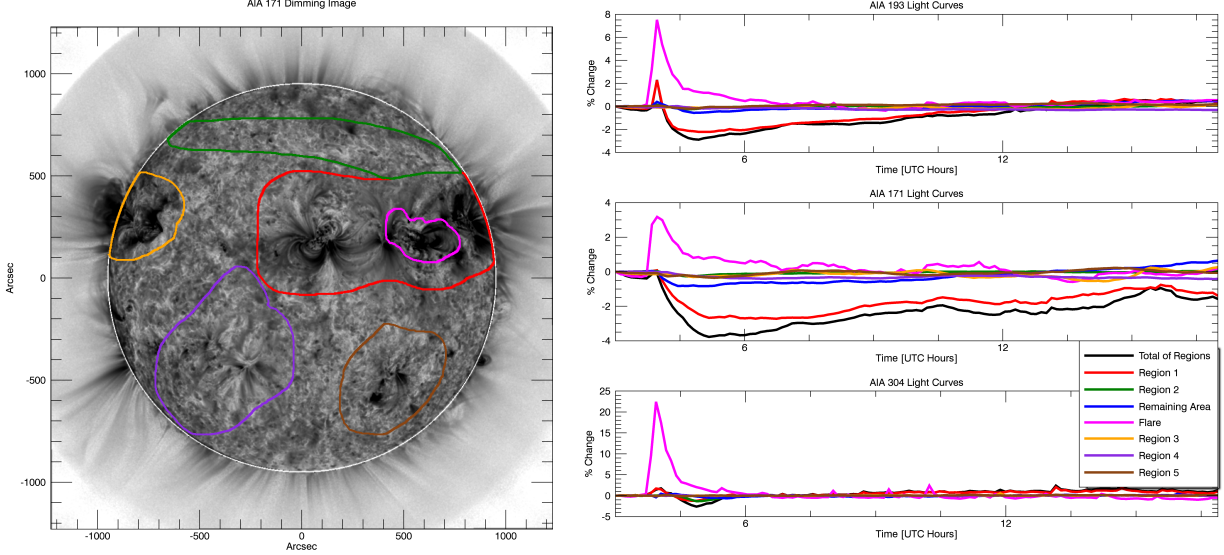


Figure 4.9: Same as Figure 4.8 but with new contours selected and no point spread function correction applied. Also the 304 Å emission time series is now complete in this later analysis using more recent AIA data products.

nearby non-flaring active region, accounts for the majority of total dimming in 193 Å and 171 Å. These two active regions are so close together that it is possible that the CME pulled mass away from a coronal volume encompassing both active regions. It can also be seen that 171 Å has a more prominent dimming in the remaining area (blue), i.e. quiet-Sun, than in 193 Å. This is evidence of heat-wave dimming described in Robbrecht and Wang (2010).

Also note that while the AIA 193 Å band contains the Fe XXIV 192 Å emission line, this high ionization state is only expected in hot plasma such as in flaring loops, which are spatially isolated in the contours of Figures 4.3, 4.8, and 4.9. Thus, for this particular case of spectral blending, the impact on analysis and interpretation is minimized.

Running-difference movies make EUV waves easier to detect by eye but it is difficult get the same clarity with static images. Instead, Figure 4.10 follows a similar format to earlier AIA figures but draws geometric contours propagating from the source active region. The light curves in Figure 4.10 are color coded from dark to light corresponding to increasing distance from the source region.

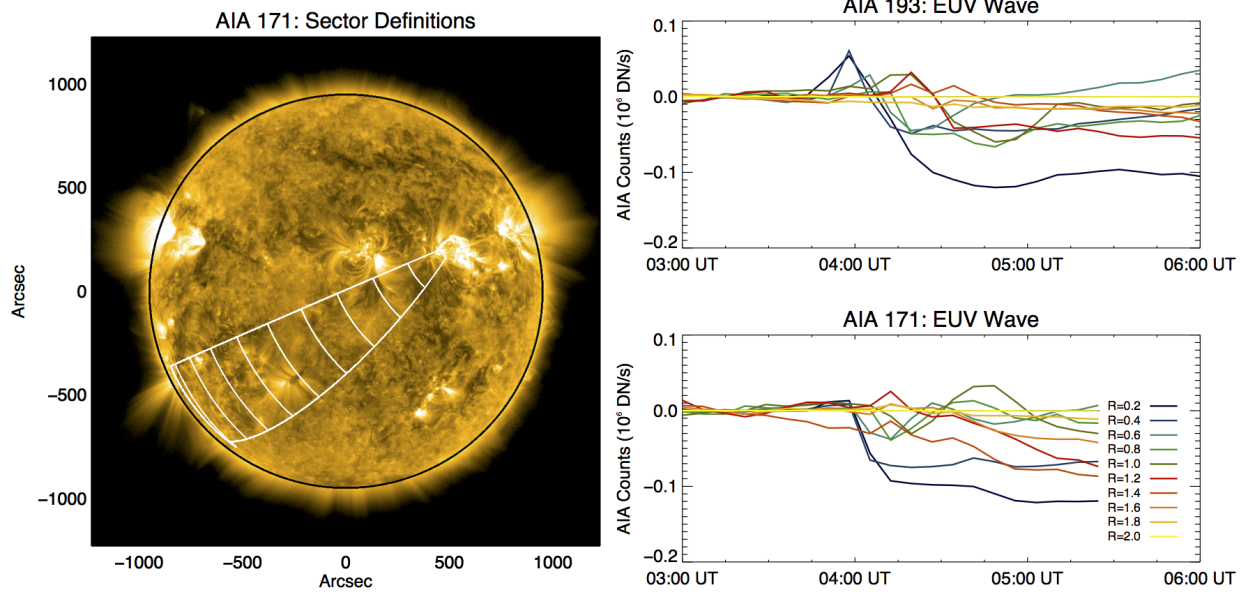


Figure 4.10: Similar format to Figure 4.9, but with geometric contours selected specifically for analysis of propagating wave. In the line plots on the right, distance from the source active region increases with lightness of color. Figure courtesy of Rachel Hock.

There appear to be thermal effects (heating and then cooling) from the wave as the AIA 193 Å and 171 Å light curves peak at different times during this time series. The propagation of the wave can be seen as the darker-color curves reach their minimum earlier with larger magnitude, and the lighter-color curves show only a minor impact from the wave. This is the expected behavior for any impulsive wave phenomenon as energy is dissipated in the surrounding medium.

SDO/EVE EUV Irradiance Observations Figure 4.11 shows selected extracted emission lines from EVE for the 2011 August 7 complex eruptive event. Because obscuration dimming is important for this case, the plot includes two He II lines: 256 Å and 304 Å, both of which show dimming at approximately the same time as what was seen in AIA (Figure 4.8). The irradiance increase from roughly 5:00 to 7:00 UT in Fe XIV 211 Å may relate to the EUV late phase discussed in Woods et al. (2011). Dimming in Fe IX to Fe XIII was significant in this case, roughly twice as large as in the simpler 2010 August 7 event. Furthermore, the peak time versus ionization state trend is reversed compared to the simpler event e.g., Fe IX 171 Å actually peaks just prior to the

GOES event peak time (second vertical dash), and higher ionization states peak later and later. This is indicative that slow heating processes are dominating the overall irradiance time series. In either heating or cooling cases, the flare-dimming deconvolution method discussed in Section 4.2 works equally well.

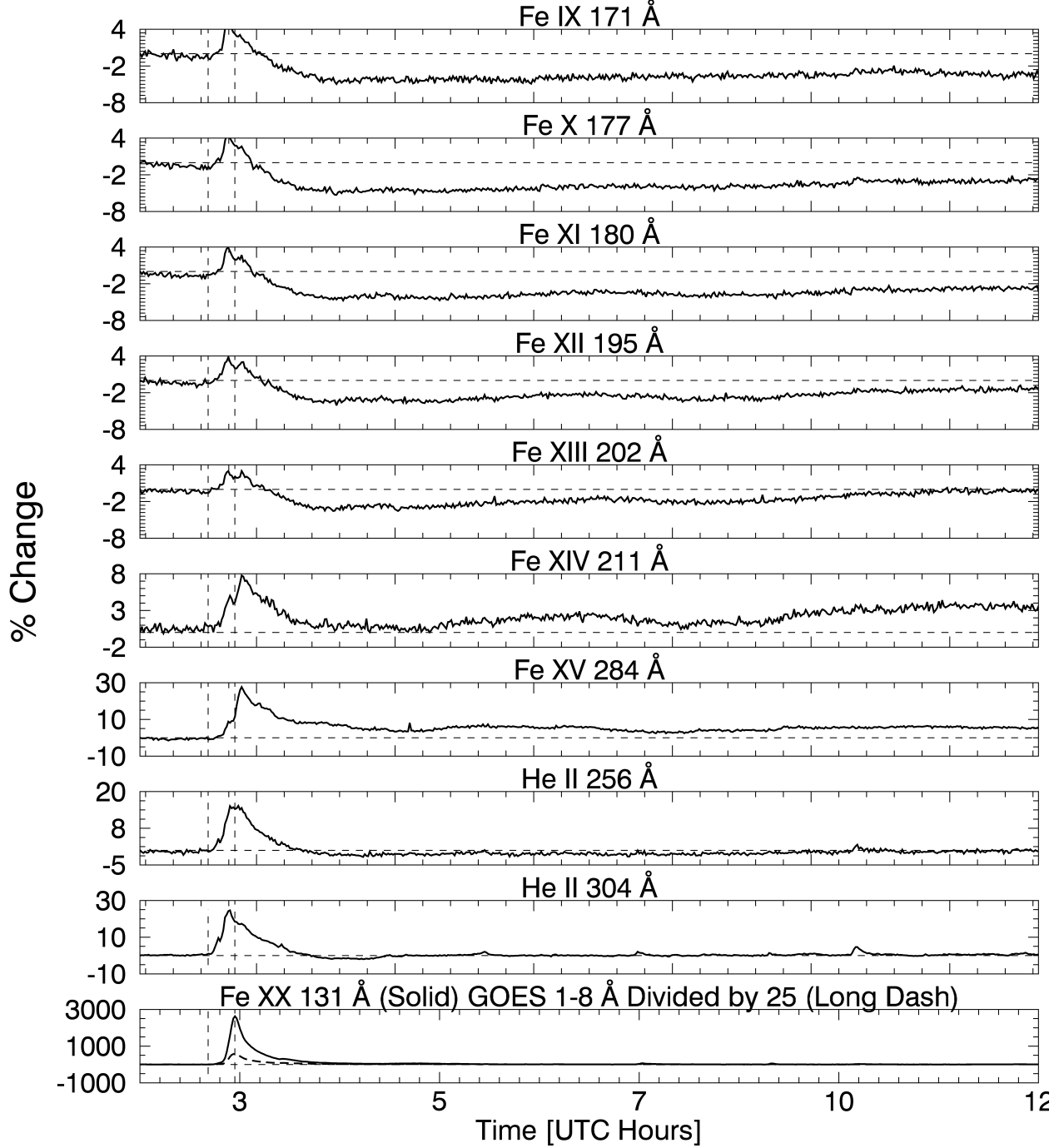


Figure 4.11: Same as Figure 4.5 but for the 2011 August 4 event, and showing He II 256 Å and 304 Å instead of Fe XVI 335 Å and Fe XVIII 94 Å. Just as before, Fe IX to Fe XIII show clear dimming, Fe XIV is borderline, and Fe XV to Fe XX show smooth brightening with no dimming. The Fe XX 131 Å profile is 3x larger than GOES 1-8 Å but still has a similar shape and timing. Also note the vertical axes: dimming is 2x larger than it was for the 2010 August 7 event. The two He II lines show dimming as well, suggestive of obscuration dimming.

4.2 Flare-Dimming Deconvolution Method

Figures 4.5 and 4.11 showed how cooling and heating impact the time of an irradiance peak in each ionization state of Fe: cooling causes the low ionization states to peak later and heating causes the reverse. In either case, it is clear that dimming magnitude decreases with higher ionization states of Fe. Eventually, around Fe XIV at 211 Å, dimming is no longer clear. The next ionization state, Fe XV at 284 Å, shows strong brightening in response to the flare but no dimming. The shape of the flare peak is similar in all wavelengths³. Using this observation, we developed a simple algorithm to remove the flare peak in the dimming lines. We make the assumption that the peak in the high ionization states is a good proxy for what *would have* been observed in the low ionization states if there were no dimming. However, the magnitudes and timing are quite different. To account for this, we scale the larger peak down and shift it in time so that they are matched. An example of the process is shown in Figure 4.12, and a flow-chart of the algorithm is shown in Figure 4.13. The ten-second EVE spectra are averaged to two-minutes to reduce noise (see black line in Figure 4.12) and the simple IDL *max* function is applied to find the peak in the light curve for every emission line listed in Table 2.1. Then, the scaled non-dimming emission line is shifted in time such that its peak matches the one in the dimming line (see green line in Figure 4.12). Finally, the scaled and time-shifted non-dimming light curve is subtracted from the dimming emission line to obtain a light curve sensitive primarily to mass-loss dimming (see blue line in Figure 4.12).

The red line in Figure 4.12 is the same red line that was shown in Figure 4.3, which corresponded to the dimming area in AIA thought to be most associated with mass-loss from the corresponding observed CME. It is clear that the deconvolution method applied brings the EVE light curve much closer (from black line to blue line) to the AIA one (red line). The agreement is not perfect, particularly at later times, and the noise in EVE is greater – even with the two-minute averaging – than AIA. However, the agreement during the initial decline is much better and is where the slope of dimming is computed, which will be shown to be a critical proxy to CME

³ Though the shape of the flare peak appears to become more smooth at higher ionization states because of the significantly larger increase making the small oscillations imperceptible in the plots

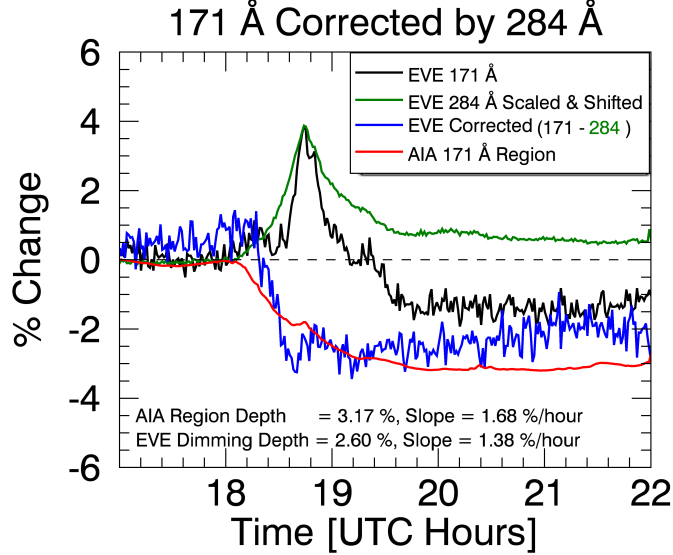


Figure 4.12: Example of the flare-dimming deconvolution method. This particular event is the simple case described in Section 4.1.1. A non-dimming line (e.g., 284 Å) is scaled down and shifted in time such that its flare peak matches the one in a dimming line (green and black, respectively). The scaled and time-shifted non-dimming light curve is then subtracted from the dimming light curve, resulting in a "corrected" or "deconvolved" light curve representative of mass-loss dimming (blue). The red line is the same as the red line in Figure 4.3, indicating the spatially isolated dimming in AIA 171. Dimming depth and slope are shown at the bottom of the plot and were computed at a particular time and time range, respectively.

velocity. The later rise in the corrected EVE line (blue) is due to a slow decrease in the scaled & time-shifted correction line (green). The unaltered dimming line (black) is relatively flat in the later hours of the dimming, consistent with the AIA light curve (red). This behavior varies by event but a "bottomed-out" dimming is common. Typically, the maximum depth is reached quickly and maintained for several hours. It will later be shown that depth is another critical proxy for CMEs; this one for CME mass. In practice, the depth is measured at a point soon after the maximum dimming is reached, so later behavior of the corrected EVE line (blue) is of less importance than the removal of the flare peak. The further in time one goes, the more likely it is for other events or physical processes to occur that would complicate the spatially-integrated EVE analysis. Duration of dimming may be an interesting parameter to study, but due to the continuing evolution

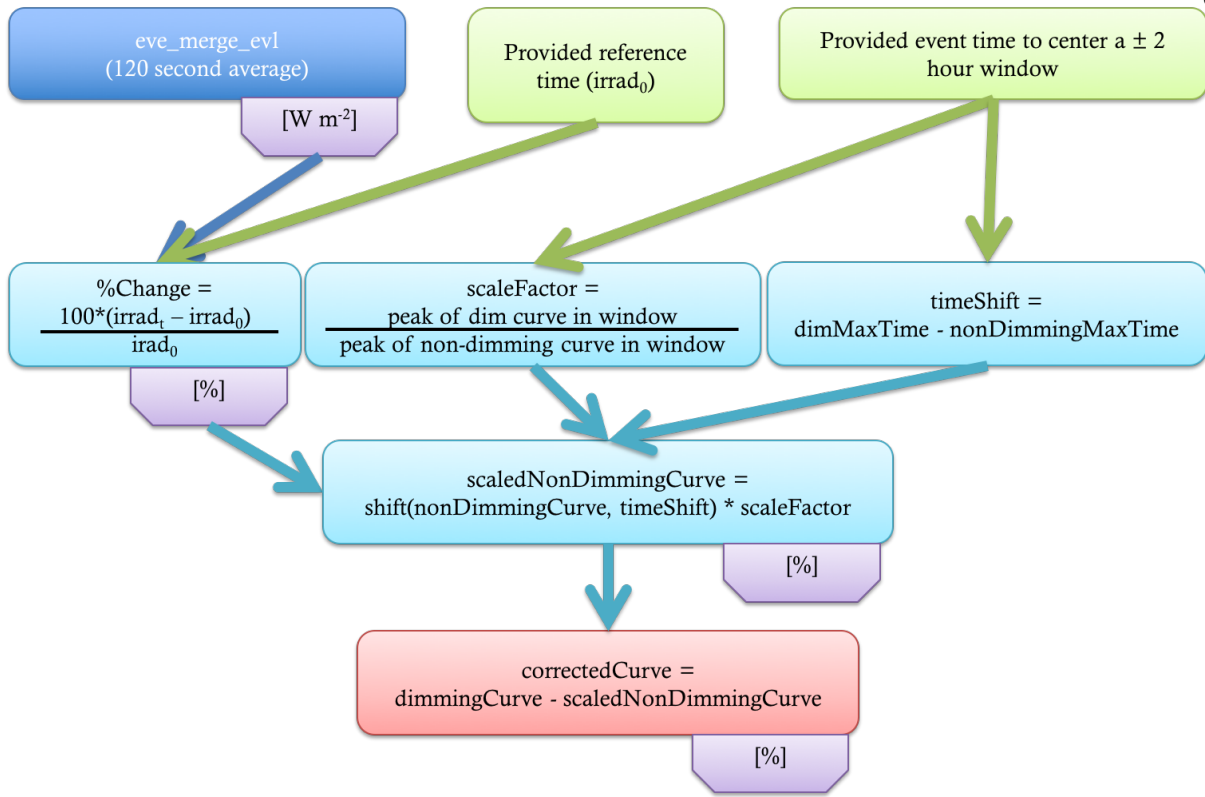


Figure 4.13: Flow-chart for the flare-dimming deconvolution algorithm. Rounded-rectangular boxes describe the steps and the purple boxes indicate the units of the irradiance at that step.

and dynamics of the sun it is of secondary priority for this study. Additionally, the duration is likely to be most closely linked to the physical processes responsible for filling plasma back into the void, relaxation of the disturbed system, and temperature evolution causing changes to ionization fractions. All of these have a tenuous connection to CME kinetics and thus provide less promise of providing a physical justification for studying dimming proxies for CMEs.

Which combinations of dimming and non-dimming lines make for the best dimming-isolated light curve? In the simple 2010 August 7 event, it was Fe IX 171 Å (dimming) and Fe XV 284 Å, respectively. Similar results were obtained using different combinations of other line pairs, one from the dimming group and one from the non-dimming group. In the 28 other cases studied (see Chapter 5), the same combination of Fe IX 171 Å (dimming) and Fe XV 284 Å (non-dimming) proved best.

4.3 Error Estimates for Flare-Dimming Deconvolution Method

The error estimates for the dimming parameters of slope and depth will be discussed in Chapter 5. Those errors will depend on the results of the present section.

Coronal dimming is a transient event lasting several hours that is studied in terms of relative change from the initiation time. As such, no long-term degradation of EVE needs to be factored into uncertainties i.e. the absolute accuracy is not important but the measurement precision is. To estimate precision, a period of solar inactivity was analyzed: 2013 January 28 from 00:00 - 01:00 UT. The estimated precision of these 120-second averaged EVE line data was calculated as the variance of the mean (Bevington, 2003), i.e., the standard deviation divided by the square root of the number of samples, which was 12 in this analysis. Table 4.2 provides the estimated precision for each emission line used in this study, and provides a sense of how well we can detect EVE dimmings that typically have depths less than 5% of the pre-flight irradiance level.

Table 4.2: Estimated precision for selected emission lines in EVE spectra. The Fe IX 171 Å and Fe XV 284 Å emission lines are the choice lines for dimming analysis with EVE data.

Ion	Wavelength (Å)	Estimated Precision (%)
Fe IX	171	0.06
Fe X	177	0.05
Fe XI	180	0.04
Fe XII	195	0.04
Fe XIII	202	0.04
Fe XIV	211	0.07
Fe XV	284	0.08
Fe XVI	335	0.17
Fe XVIII	94	0.08
Fe XX	132	0.20

These base uncertainties were propagated through each step of the EVE dimming correction method described in Section 4.2. First, the line precisions are combined with the provided reference

time to compute percent change (see Figure 4.13, Equation 4.1).

$$\%change = 100 \times \frac{(irrad_t - irrad_0)}{irrad_0} \quad (4.1)$$

where $irrad_t$ is the irradiance at each time and $irrad_0$ is the irradiance at the provided pre-flare reference time. In practice, the latter is a manually selected pre-flare point that appears to correspond well to a quiet or well-behaved period. All of the uncertainty derivations to follow are based on the basic uncertainty propagation equation,

$$F = f(X, Y) \quad (4.2)$$

$$\sigma_F^2 = \sigma_x^2 \left(\frac{\partial F}{\partial X} \right)^2 + \sigma_y^2 \left(\frac{\partial F}{\partial Y} \right)^2 \quad (4.3)$$

where F is a generic function that will be specified for each of the steps of the deconvolution method. The first step of computing percent change (i.e. where F = Equation 4.1) has the corresponding uncertainty derivation:

$$\begin{aligned} \frac{\partial F}{\partial X} &= \frac{100}{irrad_0} \implies \left(\frac{\partial F}{\partial X} \right)^2 = \left(\frac{100}{irrad_0} \right)^2 \\ \frac{\partial F}{\partial Y} &= -\frac{100 \times irrad_t}{irrad_0^2} \implies \left(\frac{\partial F}{\partial Y} \right)^2 = \left(-\frac{100 \times irrad_t}{irrad_0^2} \right)^2 \\ \therefore \sigma_F^2 &= \sigma_x^2 \left(\frac{100}{irrad_0} \right)^2 + \sigma_y^2 \left(-\frac{100 \times irrad_t}{irrad_0^2} \right)^2 \\ \implies \sigma_F &= \sqrt{\sigma_x^2 \left(\frac{100}{irrad_0} \right)^2 + \sigma_y^2 \left(-\frac{100 \times irrad_t}{irrad_0^2} \right)^2} \end{aligned} \quad (4.4)$$

where σ_x is the precision of $irrad_t$ and σ_y is the precision of $irrad_0$, which will be identical in this case since Equation 4.1 refers to a single emission line. This is the uncertainty corresponding to *dimmingCurve* and *non-dimmingCurve*. The next step in the algorithm (see Figure 4.13) is to scale the *non-dimmingCurve* irradiance so that the peaks of the dimming and non-dimming line have the same magnitude (both of which are now in % units). The derivation for the corresponding uncertainty is,

$$F = xy$$

$$\frac{\partial F}{\partial x} = y, \frac{\partial F}{\partial y} = x$$

$$\therefore \sigma_F^2 = \sigma_x^2 y^2 + \sigma_y^2 x^2 = \sigma_{scalednon-dimmingCurve}^2 \quad (4.5)$$

where x is the non-dimming light curve, σ_x is the result of Equation 4.4 (i.e. the σ_F in Equation 4.4), y is the scale factor (which is a single value), and σ_y is derived as follows:

$$\begin{aligned} \text{Let } \frac{d}{b} &= \frac{dimCurve_{peak}}{nondimCurve_{peak}} = y \\ \sigma_y^2 &= \sigma_d^2 \left(\frac{1}{b}\right)^2 + \sigma_b^2 \left(-\frac{d}{b^2}\right)^2 \\ \therefore \sigma_y^2 &= \left(\frac{\sigma_d}{b}\right)^2 + \left(\frac{\sigma_b d}{b^2}\right)^2 \end{aligned}$$

Thus we have the *scalednon-dimmingCurve* and its associated propagated uncertainty. The final step is to apply the correction to the *dimmingCurve*, which is just a simple subtraction, resulting in the final uncertainty:

$$\sigma_{correctedCurve} = \sqrt{\sigma_{dimmingCurve}^2 + \sigma_{scalednon-dimmingCurve}^2} \quad (4.6)$$

where $\sigma_{dimmingCurve}^2$ comes from Equation 4.4 and $\sigma_{scalednon-dimmingCurve}^2$ comes from Equation 4.5. Evaluation of Equation 4.6 with EVE data results in an uncertainty of $\pm 0.175\%$ ⁴. Chapter 5 will discuss the passing of the above uncertainty into IDL's *poly_fit* function and the final resultant errors associated with that process.

⁴ % here is the same unit as the irradiance, not a percentage of the irradiance value

4.4 Dimming Parameterization Results

4.4.1 Simple Dimming Case

Parameterization of dimming is focused primarily on slope and depth, both of which can be manually selected by eye. The time to select for these parameters is debatable but in this case, we chose depth to be a point soon after the dimming “floor” is reached in AIA Region 1 (red contour and line). Slope was taken to this point, starting from 17:50 UT – the time just before GOES 1-8 Å and EVE 131 Å began to rise. The deconvolution method (Section 4.2) significantly reduces the impact of the flares gradual phase peak to dimming measurements for EVE. Prior to the correction, EVE would have measured a dimming depth of 1.27% in 171 Å and 0.18% in 195 Å. After the correction, these values are 2.94% and 2.09%, respectively. Similarly, slope was changed from $1\% hr^{-1}$ (171 Å) and $0\% hr^{-1}$ (195 Å) to $2.29\% hr^{-1}$ (171 Å corrected) and $2.09\% hr^{-1}$ (195 Å corrected). The expectation is that all dimming lines should have similar dimming amount and onset time for the mass-loss dimming process, and these results after the flare gradual phase contribution has been removed support this expectation for this simple dimming case. Furthermore, if this event was being observed in real time, the gradual phase peak makes it impossible to estimate the amount and speed (slope) of dimming accurately. This correction method allows the irradiance increase due to the gradual phase contribution to be compensated in the EVE time series that have dimming.

The small difference in time between different emission peaks – Fe XX peaks 21 minutes before Fe IX in this case – is information that can be used to understand the temperature evolution during dimming. In this event, that time difference is significantly shorter than the hours-long duration of the total dimming event. Thus, it is unlikely that thermal dimming is a significant contributor to the total observed dimming. Instead, our correction method uses non-dimming lines as independent measurements of the flare gradual phase profile. Since no dimming is observed in the non-dimming lines, the gradual phase profile is assumed to be pure and can then be used as a proxy to remove only the effect of the gradual phase in the dimming light curve with a minimal

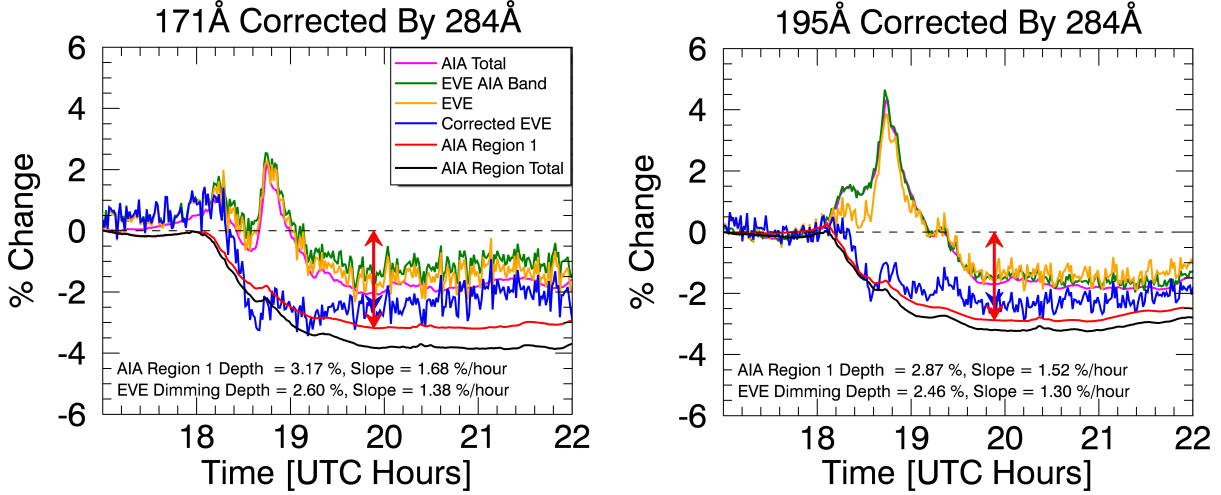


Figure 4.14: Both plots are similar to Figure 4.12 but provide more detail. The left shows results from 171 Å and the right is for 193 Å (AIA) / 195 Å (EVE). The red vertical arrow indicates the point where depth is computed and overlaps a blue vertical arrow indicating the end time of slope computation. The slope range begins at 17:50 UT.

impact on total dimming. In this way, we can effectively match AIA dimming observations, which are capable of isolating the dimming regions.

The expectation is that the EVE-corrected dimming results should have the same amount of dimming as the AIA results and are also independent of Fe ionization level (in the dimming lines). Figure 4.14 shows the comparison of EVE-corrected dimming time series to AIA results in both 171 Å and 193/195 Å, and Table 4.3 lists the dimming results.

AIA Region 1 is considered the reference for mass-loss dimming, so its dimming depth and slope are compared as an estimate of uncertainty for these results from EVE. The differences for the AIA 171 Å and 195 Å dimming depth and slope are 0.3% and 0.16% hr^{-1} , respectively. The relative uncertainty of these is 10% of the mean depth and slope values, being 3.02% and 1.60% hr^{-1} . These differences in the two different AIA bands could reflect the uncertainty that Region 1 is only due to mass-loss dimming and our ability to identify the best Region 1 boundary to encompass the mass-loss dimming phenomena. However, selecting a slightly different boundary did not greatly impact the resultant light curves, so the difference may be real. This would indicate that AIA too

Table 4.3: Key dimming results for 2010 August 7 event. Note that 195 Å in EVE corresponds to the 193 Å band in AIA, which encompasses 195 Å.

Dim line (Å)	AIA Total Depth (%)	AIA Reg. 1 Depth (%)	EVE Depth Corrected (%)	EVE Depth Un- corrected (%)	AIA Total Slope (% hr ⁻¹)	AIA Rg. 1 slope (% hr ⁻¹)	EVE Slope Corrected (% hr ⁻¹)	EVE Slope Un- corrected (% hr ⁻¹)
171	2.03	3.17	2.60	1.63	1.07	1.68	1.38	0.86
177	—	—	2.79	1.89	—	—	1.48	1.00
180	—	—	2.87	1.98	—	—	1.52	1.05
195	1.68	2.87	2.46	1.52	0.89	1.52	1.30	0.81
202	—	—	2.31	1.60	—	—	1.22	0.85
211	0.52	2.03	2.57	1.60	0.28	1.50	1.36	0.85

sees shallower dimming for higher ionization states if the deconvolution method described in Section 4.2 is not applied. The corrected EVE results for dimming depth and slope have mean values of 2.53% and 1.34% hr^{-1} , and both are 14% less than the AIA Region 1 mean values. The standard deviations for the six EVE lines corrected dimming depth and slope are 0.21% and 0.11% hr^{-1} , respectively. As expected (intended), the EVE corrected results are much more self-consistent with each other than the uncorrected results. It is also interesting to note that the AIA dimming results from Region 1 are similar to each other and the EVE corrected dimming results, but the AIA total dimming results are less similar to either of these results. The slope tracks the depth variation well; that is, the slope is less when the depth is less. Our expectation is that the dimming slope could represent the CME velocity, and the dimming depth could represent the CME mass loss.

4.4.2 Complex Dimming Case

The dimming parameterization method in this case was the same as in the simple dimming case above. Figure 4.15 shows the analogous plots for this event. While the general trend of EVE follows AIA, it's clear from these plots that applying the same deconvolution methods does not result in as good a match of EVE to AIA. Note that even uncorrected EVE reaches a deeper

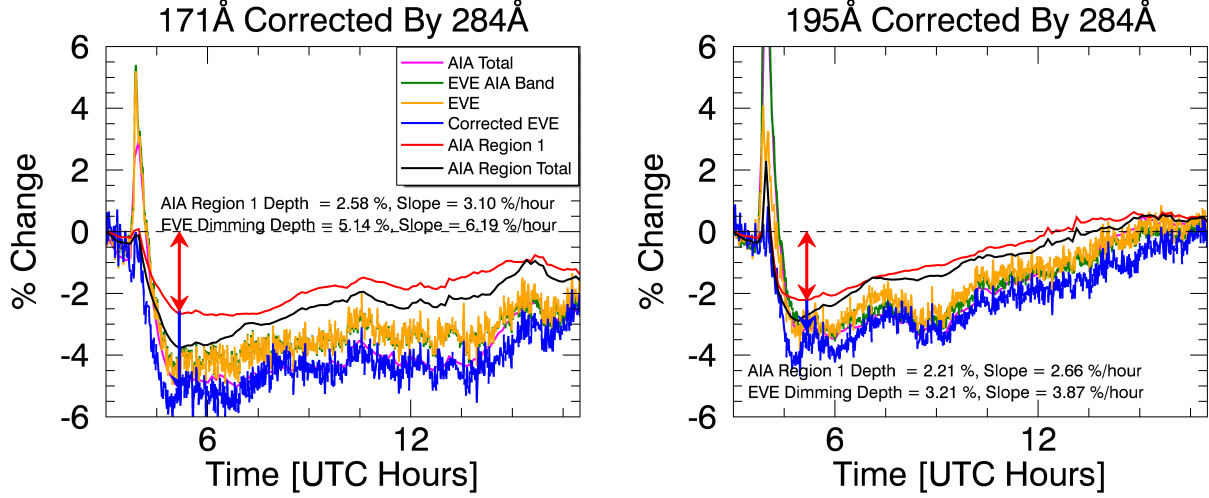


Figure 4.15: Same as Figure 4.14 but for the 2011 August 4, more complex, case. The AIA regions correspond to those selected in Figure 4.9.

minimum than the AIA light curves⁵. The only way for the deconvolution method to raise EVE irradiance would be for the non-dimming line to have dimming, which would violate the definition of it being a non-dimming line. Since this was not the case, all of the corrected/deconvolved EVE light curves (blue) are even lower than the uncorrected EVE dimming line (gold), bringing it further from the AIA "core dimming" light curve (red). The AIA total dimming results, which include all dimming regions but not the flare region, do agree better with the EVE dimming results. Nevertheless, the deconvolution method did successfully remove the flare peak in dimming lines as can be seen in the difference between the raw EVE (gold) and corrected EVE (blue) light curves. AIA showed that the remaining area (i.e. quiet Sun) had non-negligible dimming (black curve in Figure 4.8 and blue in Figure 4.9). Adding that to the AIA total dimming for 171 Å would result in a peak dimming of about 4% – still 1% lower than what is seen in EVE. Doing the same for 195 Å would get the two to match within 1%. The analysis is further complicated by the fact that the AIA bandpasses are several nanometers wide causing blending of many emission lines and continuum that makes direct comparison with EVE difficult, particularly for an event with so many

⁵ Remember that the black line is the total inside contoured areas in AIA, not the total disk

simultaneous physical processes involved, each of which has an impact on the different emission lines that can vary differently over time.

The ultimate goal of the dimming analysis is to provide proxies for CME mass and velocity. This event was included in the semi-statistical study to determine the relationship between those CME parameters and the dimming depth and slope that will be discussed in Chapter 5.

4.5 Case Studies Summary

To summarize the physical processes taking place in the simpler 2010 August 7 event, the plasma and its irradiance have source and sink terms. Near the beginning of the flare, heating is very dominant and causes a rapid increase in high ionization states for the various Fe emissions. Later in the flare, cooling of the plasma causes an increase in lower ionization states, and those cooler lines peak later than the hot lines. Through it all, the mass ejection can act as a sink for most coronal emissions (mass-loss dimming). Early in the flare, before the low ionization states have been strongly affected by the cooling described above, the mass ejection dominates and causes the irradiance to visibly drop for the cool corona lines. Much later in the flare process, as the plasma temperature and post-flare loops begin to return to pre-flare level and loop configurations, the missing plasma again becomes apparent in the irradiance time series as an hours-long, few-percent decrease. Quantitative dimming results for AIA and EVE are summarized in Table 4.3 for this simple dimming case.

The physical interpretation of the more complex 2011 August 4 event is more difficult to obtain. The size of the flare was nearly an order of magnitude larger than in the simpler 2010 August 7 case and the associated CME velocity was 1.5x faster – together, these are a general indicator that the amount of energy involved in the eruptive event was much larger in the more complex event. Additionally, the pre-eruption state of the Sun was more complex for the 2011 August 4 event, as evidenced by the more numerous active regions and polar filament, the coronal streamers, and the proximity of active regions to the one responsible for the eruption itself. All of this means that more energy was released via more mechanisms. The EUV wave was much more prominent

in this case, sympathetic responses were clear, and heating (rather than cooling) dominated the irradiance indicative of energetic processes dominating over relaxing ones. Quantitative dimming results from the analysis of AIA images are summarized in Table 4.1 for this complex dimming case.

Chapter 5

Semi-Statistical Study of Dimming-CME Relationship

Extreme ultraviolet (EUV) coronal dimmings are often observed as part of few solar eruptive events. These phenomena can be generated via several different physical processes (see Chapter 3). For space weather, the most important of these is the temporary void left behind by a coronal mass ejection (CME). Massive, fast CMEs tend to leave behind a darker void that also usually corresponds to minimum irradiance for the cooler coronal emissions. If the dimming is associated with a solar flare, as is often the case, the flare component of the dimming in the cooler coronal emission can be isolated and removed from the dimming light curve using simultaneous measurements of warmer coronal lines (see Chapter 4). In the present Chapter, we apply this technique to 38 dimming events: the two case studies from Chapter 4 plus 36 additional events taken from two separate two-week periods in 2011. Dimming is then parameterized in terms of depth and slope for each of the events. We provide statistics on which combination of wavelengths worked best for the correction method, describe the fitting methods applied to the dimming light curves, and compare the dimming parameters with corresponding CME parameters of mass and speed. The best linear relationships found with an accuracy of about 20% are that the CME speed is about 630 km s^{-1} times the dimming slope ($\% \text{ hour}^{-1}$) and the CME mass is about $1.03 \times 10^{15} \text{ g}$ times the dimming depth (%).

5.1 Introduction to Dimming and CME Parameterization and Statistics

Extensive surveys of coronal dimming events and their relation to CMEs have been performed by Reinard and Biesecker (2008, 2009). For their sample of 100 dimming events, Reinard and Biesecker (2008) found a mean lifetime of 8 hours, with most disappearing within a day. Reinard and Biesecker (2009) studied CMEs with and without associated dimmings, finding that those with dimmings tended to be faster and more energetic. Bewsher et al. (2008) found a 55% association rate of dimming events with CMEs, and conversely that 84% of CME events exhibited dimming. Dimming regions occur on a spatial scale similar to CMEs, more so than other CME-associated activity (such as flares and EUV waves). Studies have demonstrated that dimming regions can be a good indicator of the apparent base of the white light CME (Thompson et al., 2000; Harrison et al., 2003; Zhukov and Auchère, 2004). Thus, dimmings are usually interpreted as mass depletions due to the loss or rapid expansion of the overlying corona (Hudson et al., 1998; Harrison and Lyons, 2000; Zhukov and Auchère, 2004). Spectroscopic observations of coronal dimmings (Harra and Sterling, 2001; Harrison et al., 2003; Harra and Sterling, 2001) found blueshifts in several coronal lines, indicating outflow in dimming regions. When dimmings are present with a CME, they are one of the earliest signatures of the actual mass ejected from the low corona, and provide unique information on the onset time and location of the ejection. Many landmark studies have established that dimmings can contribute a large fraction of the mass to a CME (Harrison and Lyons, 2000; Harrison et al., 2003; Zhukov and Auchère, 2004; Aschwanden et al., 2009a). There are well-established methods to derive the mass properties of CMEs, but there are still outstanding questions involving the source of the CME mass: how much of the mass comes directly from the erupting region, how much comes from the surrounding or overlying large-scale corona, and how much is "swept up" as the CME propagates (Bein et al., 2013).

An Earth-directed CMEs potential geoeffectiveness is typically characterized by three values: its velocity, mass, and the magnitude and duration of the southward component of the magnetic field (B_z) at the time of Earth impact. Typical CME forecasts provide a predicted Earth ar-

rival time only. The geomagnetic storm magnitude is strongly linked to the CME momentum and magnetic field orientation while arrival time at Earth is primarily dependent on CME velocity. The current standard process for estimating velocity relies on sequential coronagraph images from SOHO/LASCO and STEREO/SECCHI. There are ground-based white light coronagraph measurements, such as by High Altitude Observatory's K-Cor instrument, but those measurements are limited to the low corona and constrained by the times that the sun is at a sufficiently high elevation as viewed from a fixed-position on Earth's surface (typically <6 hours per day). Analysis of coronagraph images to determine CME velocities and masses results in relatively large uncertainties of 30-50% (Vourlidas et al., 2000, 2010, 2011). The velocity and mass measurements with the most uncertainty are for Earth-directed CMEs that are seen as halos in coronagraphs at or near Earth. For these CMEs, velocity is significantly affected by projection on the plane-of-sky, and a large percentage of the mass can be hidden behind the instruments occulter. Without observations of these CMEs from another viewpoint, such as STEREO, it is difficult to make an accurate measurement of the CME velocity and mass from the coronagraph observations. However, dimmings associated with these CMEs are very well observed by Earth-based observations. Our studies of coronal dimming events have focused on the possibility of coronal dimming observations providing useful indicators for CME velocity and mass, and can readily be combined with most B_z prediction methods.

While earlier studies showed that dimmings can account for a significant fraction of the mass ejected, multi-viewpoint observations using STEREO data have the advantage of providing independent mass measurements for the same event from two different aspect angles, yielding a better mass accuracy. In a survey of six STEREO events observed as dimming by EUVI and as CMEs by COR2, Aschwanden et al. (2009a) found a clear correspondence between the EUV and white light mass estimates. Colaninno and Vourlidas (2009) developed a triangulation method to estimate the true (accurate) mass of CMEs from SECCHI observations. More recently, Bein et al. (2013) applied similar methods to a larger CME sample (25 events) and over an extended height range, allowing them to remove the effects of the CME emerging from behind the occulter

and to calculate the mass flux of the CMEs in the lower corona. Standard plane-of-sky velocity estimates are made and cataloged by the Coordinated Data Analysis Workshops (CDAW) CME catalog (Gopalswamy et al., 2009), which use routinely produced LASCO coronagraph images. None of these methods can be used to estimate B_z but velocity is of particular use to space weather forecasters for predicting Earth-arrival times.

In the present chapter, we analyze 38 coronal dimming events – the two from Chapter 4 plus 36 more during two separate two-week periods during 2011 – and search for the relationship between dimming and CME velocity and mass. Of the 38 total events studied, 17 could be parameterized for CME velocity and dimming speed, and 14 could be parameterized for CME mass and dimming depth.

Section 5.2 shows examples of observations, describes the method for selecting this sample of events, and explains why some events identified in AIA could not be analyzed with EVE and/or coronagraphs. Section 5.3 provides further discussion and statistics on the flare-dimming deconvolution method detailed in Section 4.2. Section 5.4 describes the fitting method applied to the deconvolved EVE light curves, including a discussion of uncertainties. Section 5.5 discusses the parameterization of fitted dimming light curves and CMEs observed in coronagraphs, also including a discussion of uncertainty. Section 5.6 shows the correlations between the various combinations of coronal dimming and CME parameters. As usual, the final section, 5.7, provides a summary of the analysis and results in this chapter.

5.2 Observations and Event Selection

In addition to the two cases studied in detail (see Chapter 4), four weeks were selected in 2011 for analysis of coronal dimming events: February 10-24 and August 1-14 (Figure 5.1). These two independent periods about 6 months apart are during the initial rise of solar activity of solar cycle 24. The duration was chosen such that there would be approximately 30 identifiable dimming events. It is also desirable to select a time when the two STEREO spacecraft orbital locations were advantageous for geometric analysis, and when the other space-based instruments used in this

study could be expected to be operating nominally. The periods of study are typical in terms of CME occurrence and solar EUV irradiance variability, both near their respective mean values (see Figure 5.1).

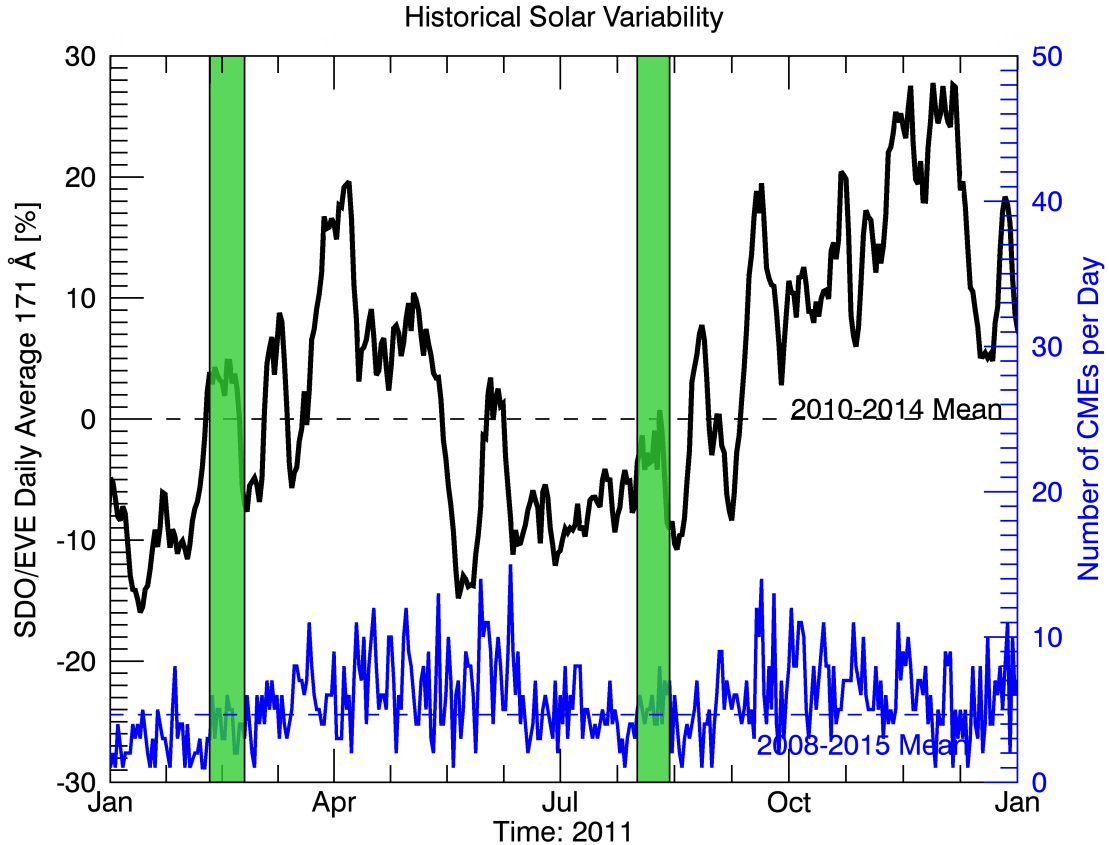


Figure 5.1: Context for the selected periods of study. The black line is the daily averaged EVE Fe IX 171 Å line and the blue line is the daily total CME occurrence. The vertical green bars indicate the selected periods of this study. The mean for EVE (dashed black line) is taken over the first four years of EVE's operations (2010-2014) and the mean for CME occurrence (dashed blue line) is taken for the most recent solar cycle starting in 2008 to the end of 2015. Note that the full range of both of these means is not shown; only 2011 is shown for clarity of the selected periods.

First, images from AIA were used to identify dimming events. Identification was performed manually using daily AIA movies to create a list of candidate events. Two people made the identifications separately, using differently formatted movies. James Mason used the AIA 211-193-171 Å composite movies (e.g., Figure 4.4) and Dave Webb used the 193 Å movies. The primary initial

selection criteria were that 1) the dimming must persist for several hours and 2) the dimming must have non-trivial spatial extent (at least comparable to the size of an active region). The independently identified events were then accumulated, duplicates merged as positively identified events, and disparities investigated by each identifier. Sometimes disparities proved to be questionable events according to the selection criteria above and were removed from the event list. Other times the disparities proved that the independent identification acted as a failsafe – a single observer simply missed an event but the other caught it. Future studies that are more expansive, such as analyzing the entire SDO era, should use the automated AIA dimming detection method developed by Krista and Reinard (2013).

Once the event list was deconflicted, the approximate time of the event was used to search the related observations in other instruments: flares from GOES X-ray flux, CMEs from LASCO and COR, and solar irradiance from EVE. This initial list included 38 events (including the 2010 August 7 simple case from Chapter 4, which was outside the four week period, and the 2011 August 4 complex case from Chapter 4, which happened to fall inside the second two-week range). In some cases, the dimming was not clear in EVE data or the CME was not clearly identified in the coronagraph images; nevertheless these were dimmings identified in AIA and are listed in Table 5.1 and Appendix A for completeness. Appendix A expands the event list with additional ancillary data such as dimming and CME parameterization values and associated uncertainties. Of the 38 total events, 29 could be parameterized with EVE in terms of depth and slope, 21 had measured CME velocities, and 17 had measured CME masses. Six of the CMEs had at least two views so that 3-D analysis could be applied for improved accuracy of the CME kinetic parameters.

Table 5.1: Event list. Times and locations are approximate. The “derived parameter” columns abbreviations are as follows: V = velocity, M = mass, 3V = 3-D velocity, 3M = 3-D mass, D = depth, S = slope. Only 29 of the events have the full complement of parameterizations to allow the study of the relationships between dimmings and CMEs. See Appendix A for event list with additional ancillary data.

Event #	Date	Time [UT]	Location	EVE Derived Parameters	CME Derived Parameters
1	2011 Feb 10	07:40	N20 W-limb	D, S	—
2	2011 Feb 10	13:36	N20 W-limb	D, S	V, M
3	2011 Feb 11	07:46	N20 W-limb	D, S	V, M
4	2011 Feb 11	13:21	N60 W00	D, S	—
5	2011 Feb 11	21:43	N10 E-limb	D, S	V, M
6	2011 Feb 12	06:05	N30 E10	D, S	—
7	2011 Feb 13	14:00	S10 E10	D, S	3V, 3M
8	2011 Feb 14	15:45	S10 W00	D, S	V, M
9	2011 Feb 14	17:36	N30 E20	—	3V, 3M
10	2011 Feb 15	02:07	N00 W00	D, S	3V, 3M
11	2011 Feb 16	14:40	S20 W30	D, S	—
12	2011 Feb 17	00:47	E40 W00	D, S	—
13	2011 Feb 18	11:15	S10 W50	D, S	V, M
14	2011 Feb 17	19:20	N30 W00	D, S	—
15	2011 Feb 24	07:40	N10 E-limb	D, S	—
16	2011 Feb 25	07:00	N45 E60	D, S	V, M
17	2011 Aug 2	05:10	N05 W20	D, S	V, M
18	2011 Aug 2	13:00	N00 E-limb	D, S	—
19	2011 Aug 3	13:43	N05 W48	D, S	V, M
20	2011 Aug 4	04:12	N05 W58	D, S	V, M
21	2011 Aug 4	04:41	N80 W00	—	V
22	2011 Aug 5	07:25	S30 E50	—	—
23	2011 Aug 6	11:50	S14 E10	D, S	—
24	2011 Aug 6	18:25	N05 W25	—	—
25	2011 Aug 6	17:35	N30 W-limb	—	V, M
26	2011 Aug 6	22:40	N10 W25	D, S	—
27	2011 Aug 7	04:00	N10 W55	D, S	V, M
28	2011 Aug 8	01:15	N80 E05	—	—
29	2011 Aug 8	11:00	N15 W70	—	—
30	2011 Aug 8	17:42	N05 W05	D, S	—
31	2011 Aug 8	18:42	N05 W75	—	3V, 3M
32	2011 Aug 9	08:10	N15 W70	D, S	3V, 3M
33	2011 Aug 9	09:12	S30 E-limb	—	—
34	2011 Aug 9	11:26	N05 W00	D, S	V, M
35	2011 Aug 11	10:23	N00 W-limb	D, S	3V, 3M
36	2011 Aug 12	00:09	N45 E80	D, S	V, M
37	2011 Aug 12	11:13	N50 E70	D, S	—
38	2010 Aug 7	18:05	N05 E60	D, S	3V, 3M

Because EVE irradiance observations are spatially integrated, dimmings from distant areas that occur too closely in time overlap in the irradiance time series and cannot be easily separated and parameterized. Thus, such events have a “–” in the EVE Derived Parameters column of Table 5.1 and are excluded from the correlative study in Section 5.6. This was the case for Events 9, 21, 29, 31, and 33. Similarly, Event 22 was a series of small eruptions from an active region with multiple slow CMEs whose analysis would be prohibitively difficult for a statistical study. Secondly, some dimmings identified in AIA were not detectable in the EVE data, making parameterization impossible. Here, “not detectable” simply means that the EVE light curves did not show anything resembling the archetypal dimming near the time that was identified in AIA. This implies the magnitude of the dimming was small (< 1% impact on irradiance), which would be the case if the dimming itself was not very deep or if evolution elsewhere on the solar disk dominated (e.g., active region evolution). Examples of the former are Event 24, which was a very slight darkening of an active regions coronal loops with no identified CME; Event 28, which was a small occurrence of “coronal rain”, also with no identified CME; and Event 25, which was an off-disk dimming event with a narrow CME. In principle, it is possible for off-disk events to generate a large irradiance change, but in this case the change was insufficient to be observable by EVE. In total, these criteria on EVE measurements resulted in 9 of the 38 events being excluded from the correlation analysis, leaving 29 events. These 29 can be processed using the flare-dimming deconvolution method described in Section 4.2. The next section will discuss the results of this process.

5.3 Flare-Dimming Deconvolution Method Statistics

There are 30 permutations of the dimming emission lines (171, 177, 180, 195, 202, 211 Å) and non-dimming emission lines (211¹, 284, 335, 94, 131 Å) for the correction method. Each one is processed using the same algorithm described in Section 4.2. Figure 5.2 shows an example of all 30 combinations for a single event (Event 20).

It can be seen that the the higher the ionization state of the non-dimming line (blue), the

¹ Recall that 211 Å is included in both dimming and non-dimming categories to reflect its ambiguity

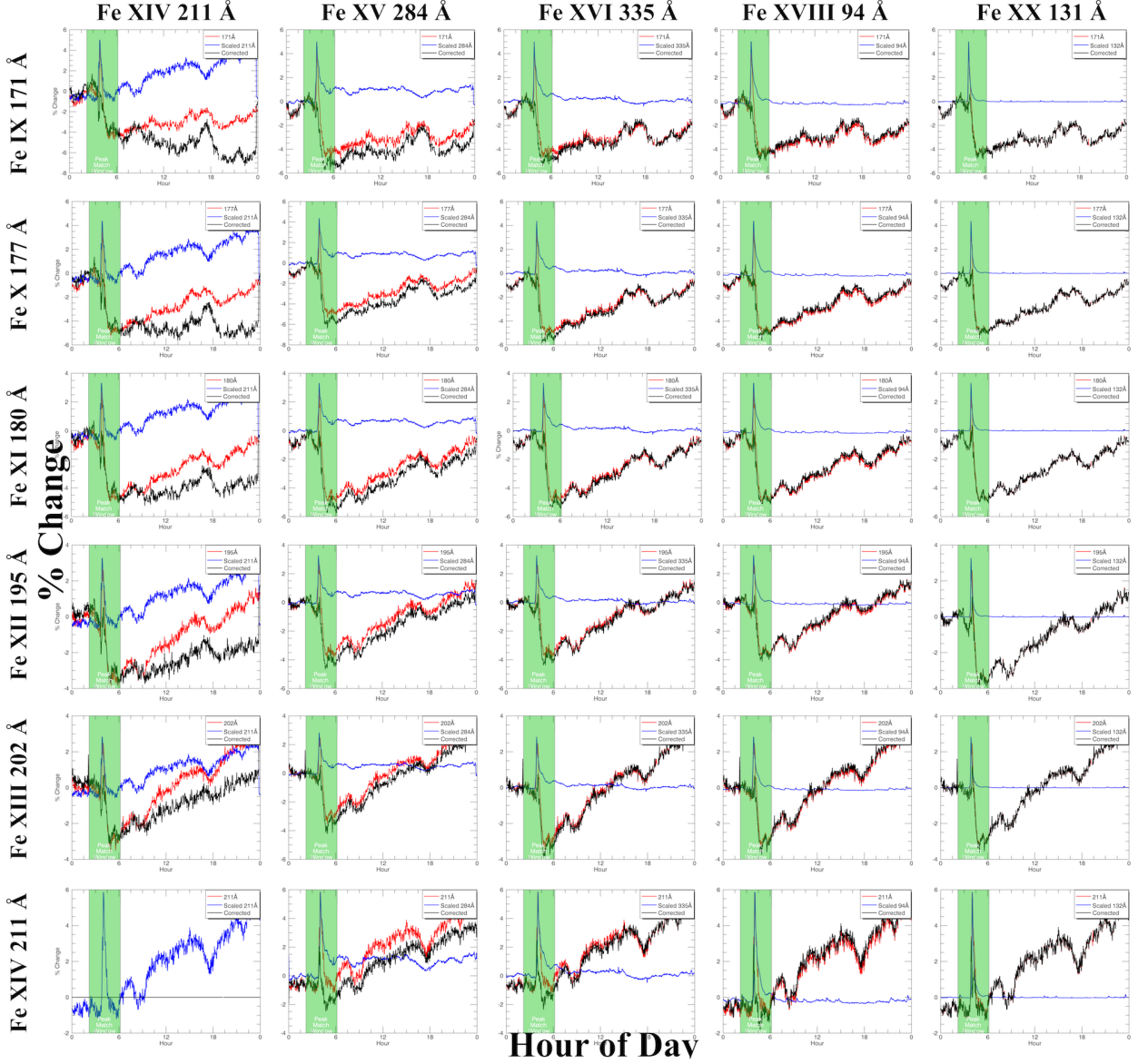


Figure 5.2: Example of every combination of the dimming (rows) and non-dimming (columns) emission lines for the deconvolution method for a single event (Event 20). In each plot, the red is the dimming line, blue is the scaled and time-shifted non-dimming line, and black is the result of the subtraction (red - blue). The vertical transparent green bar indicates the time window the algorithm uses for finding and matching peaks. All emission lines are for Fe. Ionization state increases down for dimming lines and to the right for non-dimming lines.

“purer” the flare light curve, i.e., higher ionization states return almost perfectly back to their pre-flare irradiance level soon after the peak while lower ionization states show some additional post-peak response. Because the most intense heating occurs early in the flare – during the impulsive

phase as observed by GOES or RHESSI HXRs – it’s unlikely that the emission from high ionization states disappears due to heating into the next ionization state. Rather, it returns to its pre-flare level because the intense heating supporting its existence is over and cooling has set in. Indeed, the mid-ionization states such as Fe XVI at 335 Å show a slow, hours-long ramp downward in irradiance. The fact that these mid-ionization states don’t immediately return back to their pre-flare level indicates that their net cooling rate is lower. The lower net cooling rate is likely due to the higher density of these ions where collisional de-excitation in the plasma competes with radiative cooling. Additionally, the Einstein A coefficient for Fe XVIII 94 Å is 11.4² larger than for Fe XVI 335 Å, indicating that the radiative cooling is even slower for Fe XVI 335 Å. The blue light curve for FeXVI 335 Å indicates that the cooling is ongoing during this hours-long period. In other words, warm ions like Fe XVI are slowly recombining with electrons and acting as a source term for the cooler ionization populations. Critically, this “feeding” of the lower ionization populations, like Fe IX, is a cooling mechanism, not a mass-loss one. By removing this trend as indicated by the irradiance in e.g., Fe XV 284 Å, we obtain a light curve more sensitive to mass-loss than temperature evolution (black curve in Figure 5.2).

In Chapter 4, it was found that for the 2010 August 7 event, the combination of Fe IX 171 (dimming) and Fe XV 284 (non-dimming) in EVE gave the best match to the spatially isolated dimming in AIA 171 Å. The only dimming mechanisms identified to be important in this event were mass-loss and thermal. Thus, it seems that the 171 Å - 284 Å combination can successfully mitigate the impact of thermal processes on the dimming line. If other dimming mechanisms play an important role in the irradiance, as is the case for the 2011 August 4 case in Chapter 4, it may be necessary to account for them, such as by identifying and removing the impact of obscuration dimming. Until such an analysis is performed, we apply the deconvolution method to the additional 28 events with viable EVE data, using the clean removal of the flare peak as the criteria for determining the best combination of dimming-non-dimming line. In other words, the peaks of the dimming and scaled/time-shifted non-dimming lightcurves should be similar in shape.

² Determined with the NIST online database

Figure 5.2 shows that many of the combinations would meet this criteria. The next determining factor is depth of dimming. Event 20 had a relatively consistent depth of dimming for all dimming lines, but this is not the case for all events. Generally, we prefer a larger magnitude dimming as its interpretation is less ambiguous and less susceptible to being dominated by other physical processes such as active region evolution. As was shown in Chapter ??, the ionization level is inversely proportional to depth of dimming. Thus, 171 Å is generally preferred as the dimming line but is evaluated on a case by case basis for the events studied here. Finally, we prefer to use 284 Å as the non-dimming line for deconvolution based on the physical motivation provided in the paragraph above.

This methodology has been applied to the 28 unique EVE dimmings found during the four weeks studied. Of these, all 28 were found to be best represented by the 171 Å - 284 Å combination. We will gain additional confidence in the effectiveness of this line pairing for EVE if we find a positive and statistically significant correlation between corrected EVE light curve parameterizations to independently derived CME mass and velocity. The first step in that process is to fit the EVElight curves in preparation for dimming parameterization.

5.4 Dimming Light Curve Fitting Method

5.4.1 Physics Motivation and Fit Types

The β parameter for a plasma is an indicator of the relative importance of plasma and magnetic pressures, expressed as

$$\beta = \frac{p_{plasma}}{p_{mag}} = \frac{nk_b T}{B^2/(2\mu_0)}$$

where p is pressure, n is number density, k_b is Boltzmann's constant, T is temperature, B is magnetic field strength, and μ_0 is the permeability of free space. In the solar corona, β is typically < 1 , indicating that the magnetic field dominates the flow of plasma, i.e. plasma is confined by magnetic fields. Thus, in the initiation of a CME where magnetic fields are propelled out of the

corona and expand as they do so, the plasma in the enclosed bubble of the CME experiences an adiabatic expansion and density decrease (Figure 5.3).

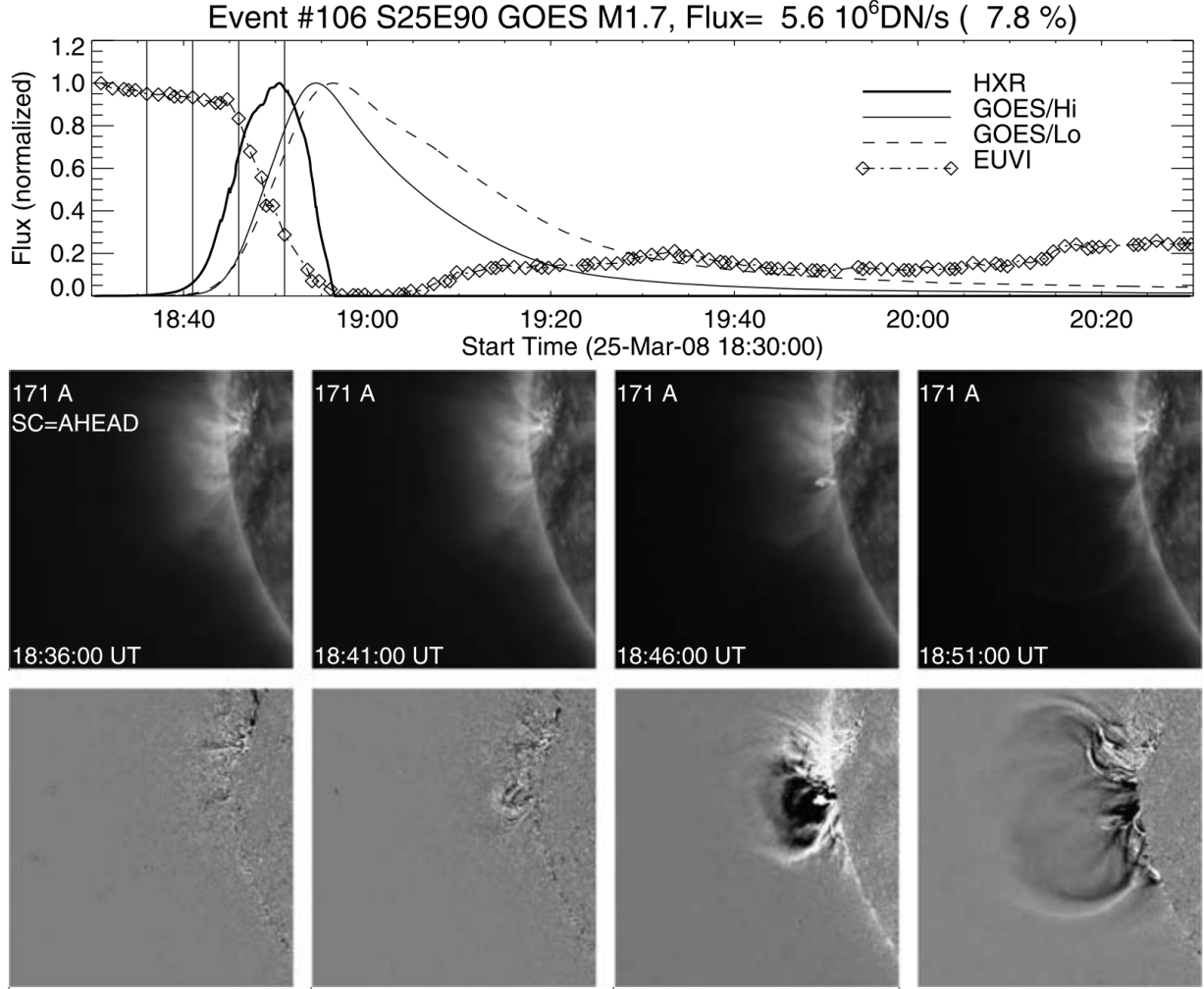


Figure 5.3: Example of CME bubble expansion and associated EUV dimming. (Top) Soft X-ray (GOES/Lo 0.5–4 and 1–8 Å, thin curves) and EUV (STEREO-A/EUVI, diamonds) light curves and time derivative, $dI(t)/dt$, of the harder soft X-ray light curve (thick solid line) for the flare/CME event on 2008 March 25 at 18:30 UT. (Bottom) Four STEREO-A/EUVI images (top row) and running-difference images (bottom row). Note the strong dimming in the EUV light curve. The diamond symbols mark the times of the EUV images; the selected images shown below are marked with vertical lines. The peak EUV flux is $F = 5.6 \times 10^6 DNs^{-1}$ (or 7.8% of the total flux). The field of view of the images is 512 EUVI pixels (600 Mm). Adapted from Aschwanden et al. (2009b).

Aschwanden et al. (2009b) described this process and here we adapt it for the variation of intensity in collisionally-excited lines as a function of height for a constant-temperature and

expanding volume:

$$\frac{I(t)}{I_0} \propto \left(\frac{h_0}{h(t)} \right)^3 \quad (5.1)$$

where $I(t)$ is the bubble intensity as a function of time t , I_0 is the intensity at an initial time, and h is the corresponding height from the photosphere. Note that height as a function of time is a speed. This simple power-law description does not account for any complicating factors such as thermally-induced emission changes, interaction with overlying coronal magnetic fields, or later recovery of the regional emission. Aschwanden (2009) developed a more sophisticated model of dimmings, including adiabatic expansion and gravitational stratification. However, the model contains 14 free parameters and is more suited to a case-by-case study of dimming morphologies. For the purposes of our correlative study, it is reasonable to assume that the decrease in emission due to the volume density is more significant than the thermal and inhomogeneity effects, and that the effective height scale of the CME is the most important parameter.

In Equation 5.1, as time tends to infinity, the local emission goes to zero. However, the solar irradiance, as observed by EVE, decreases to a constant background value during a dimming event. Thus, this simple power-law fit for the EVE dimming events would be expected to be poor, i.e., large χ^2 . Furthermore, the relationship of height and time is not well established, so different functions are fitted to the EVE dimming events to explore which functions are more optimal for determining the dimming event parameters of depth and slope. Exponential and power law fits tend to result in $\chi^2 > 20$, meaning they were very poor fits. Polynomial fits up to order five were also computed, with 5th and 3rd orders appearing to best describe the shape of the light curves (see Figures 5.4 and 5.5). Although the 3rd order polynomial function is expected to be a better match to the theory, the manually-selected best-fit function is used for deriving the dimming slope and depth (see Section 5.5).

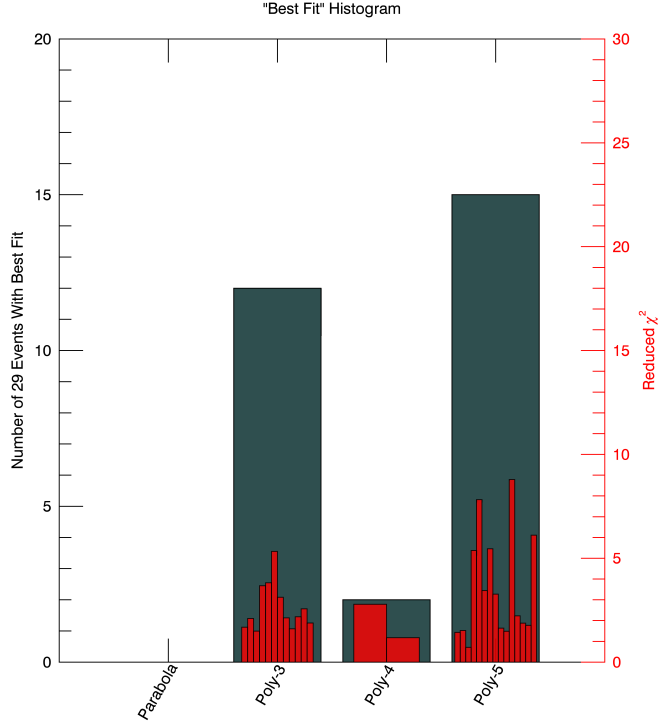


Figure 5.4: (grey) Statistics of manually selected “best fit” for all unique EVE dimming events in 4 weeks studied and (red) the reduced χ^2 for the best fits. The 3rd and 5th order polynomial fits provided the largest number of best fits.

5.4.2 Dimming Fit Uncertainty Computation

The uncertainties from Section 4.3 correspond to the deconvolved/corrected EVE dimming light curve. Those light curves are the input for the fitting function, IDL’s *poly-fit*, which also accepts an input *measure_errors* for uncertainties. Figure 5.5 shows polynomial fits from 2 to 5 with the measurement errors and the resultant 1σ uncertainties computed by *poly-fit*. The fits achieve the desired effect of reducing uncertainty even further than 2-minute averaging of the EVE data and providing a smooth function to parameterize.

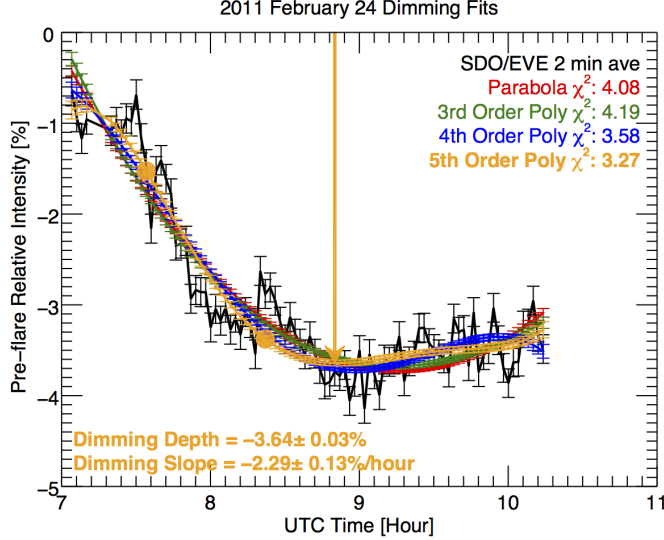


Figure 5.5: A single dimming event (Event 15) showing the reduction in uncertainties of the fits compared to the EVE data. The arrow shows the location of dimming depth parameterization for this event, and the two filled circles indicate the range where slope was computed. Their colors correspond to the fit types in the legend. The lowest χ^2 indicates that the 5th order polynomial was the best fit for this event, but we note that the results from the other polynomial fits are very similar.

5.5 Parameterization Methods

Dimming and CMEs are complex phenomena with complex observations and associated data analysis. Our end goal is to provide simple measures of dimming to act as proxies for CME mass and speed, driven by a physical explanation. Given this, the space weather community would have an independent indicator of CME presence and importance to geospace, and the astronomy community would have a means of detecting and characterizing CMEs on other stars (albeit a first-order characterization). To that end, this section describes the parameter derivations for dimming and CMEs that will be used to establish a correlation in Section 5.6, motivated by the physics in preceding sections.

5.5.1 Dimming Parameterization

Points for the computation of slope and depth are selected manually from the best fit light curve from Section 5.4. Slope point selection was guided by the desire to have χ^2 near unity and by some flexibility for events where the EVE dimming correction method did not completely remove the flare peak of the cool corona line (Fe IX 171 Å). In such cases with a residual flare peak, the fits can deviate from the “pure” dimming light curve and skew the χ^2 upward. Rather than develop a complicated algorithm to account for this effect autonomously, selection of the best fit was done by manual inspection. Dimming slope was computed across a range: the initial point was typically chosen to be soon after the initial dimming rollover when the slope becomes relatively constant, and the final point was selected just prior to the inverse rollover leading to the relatively flat period in the light curve (see solid circles Figure 5.5). The slope need not be constant between these two points. For each time step within the selected range, the derivative was computed. The single-value slope parameter for each event is the mean of these derivative (slope) values. The dimming depth parameter is taken from a relatively stable pre-flare value to a point near the beginning of the dimming floor (see arrow in Figure 5.5).

The uncertainty associated with dimming depth is just the uncertainty of the fitted light curve at the point selected for the depth measure, as exemplified by the error bar at the arrow in Figure 5.5. The uncertainty for slope requires some additional computation. To compute the derivative of the light curve at each point within the specified time range, IDL’s *deriv* function was used; the corresponding *derivsig* function returns the 1σ uncertainty for each point in the derivative array. Collapsing the various derivatives into a single slope parameter via the mean has the corresponding uncertainty,

$$\sigma_{slope} = \frac{1}{N} \sqrt{\sigma_1^2 + \sigma_2^2 + \dots + \sigma_n^2}$$

where N is the number of points, and $\sigma_1 \dots \sigma_n$ are the uncertainties for each point returned from *derivsig*. Appendix A includes the dimming depth, slope, depth uncertainty, and slope uncertainty

for each of the 38 events studied.

5.5.2 CME Parameterization

Detailed 3-D analysis of the velocity and mass was possible for six of the best-observed CMEs, using either or both LASCO and the CORs data. These six events are noted as 3V, 3M in Table 5.1 and shown as solid red symbols in Figure 5.6. Following the method of Colaninno and Vourlidas (2009), the GCS model is fit to the observations to determine the 3-D location and heights of the CMEs. The 3-D heights and longitude of the CME are needed to calculate the “true” 3-D mass of the CME. These heights are also used to calculate the de-projected velocity of the CME. The reported masses are for a height of $15 R_{\odot}$, using the fitting method of Bein et al. (2013) for mass increase with height. For the 2011 February 13-15 CMEs the mass was measured in both COR2A and COR2B and then averaged. For the 2011 August 9 and 11 CMEs, the mass was measured in LASCO-C3 only.

The following procedure was used to estimate the uncertainties for the CME kinetic parameters. The LASCO CDAW measurements were used for most of the events to derive the CME velocity and mass, which are based on a single viewpoint observation as opposed to 3-D. The reported linear speed of each CME is obtained by fitting a straight line fit to the height-time measurements at a fixed position angle. If we assume conservatively that the CME axis is 60° from the sky plane as the worst case (for non-halo CMEs), this results in a factor of 2 (50%) underestimation of the speed. The CDAW catalog also provides the CME span angle, which can be used to provide an estimated error on the CME mass (Figure 4 of Vourlidas et al. 2010). As an example, if we take Event 2 from Table 5.1 above, then using these errors we have $speed = 338 \pm 345 km s^{-1}$ and $mass = 3.40 \times 10^{14} \pm 4.30 \times 10^{14} g$.

For the six events with 3-D analysis of the CME measurements, we derive the error in the speed from the linear fit to the data assuming the error in the 3-D height measurements is $\pm 0.48 R_{\odot}$ (Colaninno et al., 2013). Thus, if we take Event 7 as a typical 3-D CME measurement, we get $353 \pm 13 km s^{-1}$ for the speed. The mass is still considered an underestimate from the 3-D analysis

but is better determined because the plane-of-sky angle and 3-D heights are known from the GCS model fit, so a $\pm 15\%$ error is assumed for the 3-D mass estimates (Bein et al., 2013).

For the purpose of linear-fitting with dimming parameters in Section 5.6, the midpoint between the low and high limits is chosen for each CME speed and mass parameter reported here, and the CME parameter error is the range between the high and low limits divided by two (i.e., \pm error bars in Figure 5.6). The plot of the points themselves does not display this center-point for single-viewpoint derived CME parameters but does for 3-D derived CME parameters. Appendix A includes the CME speed, mass, speed uncertainty, and mass uncertainty for each of the 38 events studied.

5.6 Dimming and CME Parameters Correlation

As described in Chapter 4, we expect direct proportionality between dimming depth and CME mass, and between dimming slope and CME velocity. In other words, there should be a stronger correlation between these parameters than between any other combination of parameters. The analysis of just two events in Chapter ?? does not establish any such possible relationships. This study is a more in-depth examination of such possible relationships with many more events. While our intention for this study was to have 30 events, it was challenging to obtain CME velocity and mass for all of the candidate events. Nevertheless, there was a sufficient number events with dimming and CME parameterizations to establish a significant correlation. Table 5.2 provides the Pearson correlation coefficients (Pearson, 1895) and p-value permutation statistical tests between each combination of the dimming and CME parameters, which confirms our initial expectation. Smaller p-values indicate a lower probability that the correlation could have arisen if no correlation existed at all. There is positive correlation between all of the parameter permutations, which is likely due to the “big flare syndrome” (Kahler, 1982, 1992), e.g., a rapid, powerful coronal magnetic field energy release tends to result in a faster, more massive CME.

Figure 5.6 shows scatterplots of speed vs. slope and mass vs. depth with estimated error bars. Linear fits for each scatterplot were computed using IDL’s *fitexy*, which can accept input

Table 5.2: Pearson correlation coefficients (PCC) and p-values between dimming and CME parameters.

Parameter 1	Parameter 2	PCC	p-value
Slope	Speed	0.78	1.51×10^{-4}
Depth	Mass	0.74	7.80×10^{-4}
Slope	Mass	0.60	0.01
Depth	Speed	0.51	0.04
Mass	Speed	0.64	2.79×10^{-3}
Slope	Depth	0.27	0.15

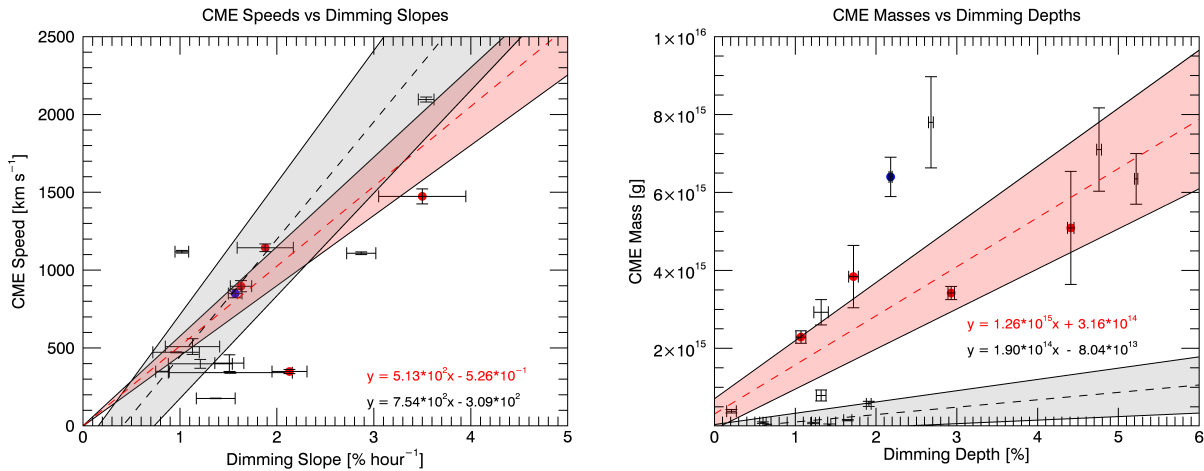


Figure 5.6: Scatterplots of (left) CME speed and dimming slope and (right) CME mass and dimming depth. Data without a center-point are derived from a single viewpoint of CMEs and are thus presented as a range of possible values rather than a single point with a standard uncertainty. Red symbols, line, and text indicate 3-D computed CME parameters, and the blue symbol indicates data from the simple 2010 August 7 event, which is also 3-D derived. Linear fits are shown as the dashed lines, and the grey/pink region represents the 3σ uncertainty of the linear fits.

errors in both axes and return the fit parameters with a 1σ uncertainty. The fit uncertainty is converted to 3σ and used to define the grey/pink regions of Figure 5.6. The fit equations are also listed in the Figure 5.6 panels. This process was repeated using only CME values computed from the 3-D methods and are plotted as the red dashed line and pink shaded region. In order to get a nominal fit for the 3-D case with so few data points, a virtual $(0, 0)$ point was added to the fit.

The mass vs. depth plot (Figure 5.6, right) is linear-linear for clarity of the fits, but several of the data points end up off scale as they are $< 1 \times 10^{15} g$. These points skew the fit uncertainty (grey area) significantly. Figure 5.7 is analogous to Figure 5.6, but shows the fit applied to high-mass only and low-mass only separately. The fit for high-mass only shows a slope that is less than a factor of two different from the all-points and 3-D points fits, whereas the fit for low-mass shows a slope that is an order of magnitude different from the others. When ignoring the low-mass points, the fit uncertainty narrows and is less skewed (grey area) and nearly all points fall within the uncertainty, when accounting for the uncertainty of the individual mass points. Thus, we suspect there may be two statistical families in the data. We examined all of these events individually and didn't notice any dimming or CME peculiarities that might cause this separation of high-mass and low-mass families in this comparison. The families do not strongly correlate to GOES flare magnitude (or whether there was a flare at all), CME span, or flare type. This result may be an artifact of small number statistics, which could be remedied in future work with many more dimming-CME events.

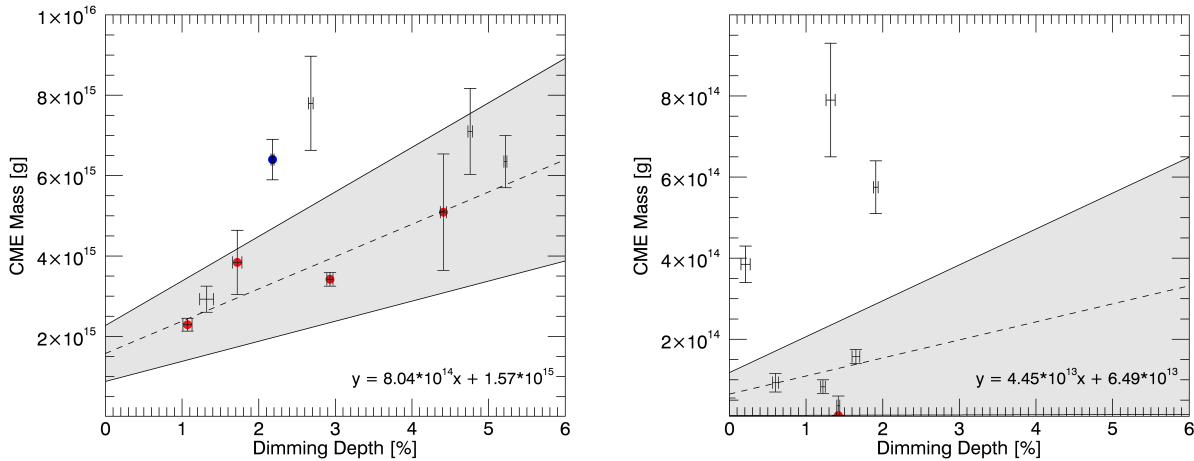


Figure 5.7: Same as Figure 5.6 but for (left) high CME mass ($\geq 1 \times 10^{15} g$) and dimming depth and (bottom) low CME mass ($< 1 \times 10^{15} g$) and dimming depth.

The 1σ uncertainties were computed by *fitexy* for each of these linear fits (note that the shaded regions in Figure 5.6 are 3σ). For all-points CME speed versus dimming slope, the fit slope

is $7.54 \times 10^2 \pm 9.45 \times 10^1$ and fit y-intercept is $-3.09 \times 10^2 \pm 5.83 \times 10^1$. Assuming a y-intercept of zero and averaging the black and red slopes in Figure 5.6 left, the best estimate for the linear relationship is that the CME speed is 630 km s^{-1} times the dimming slope ($\% \text{ hour}^{-1}$).

For CME mass vs dimming depth, the fit slope is $1.90 \times 10^{14} \pm 3.31 \times 10^{13}$ and fit y-intercept is $8.04 \times 10^{13} \pm 4.15 \times 10^{13}$. Averaging the 3D-derived and high-mass-only slopes, the best estimate for the linear relationship is that the CME mass is $1.03 \times 10^{15} g$ times the dimming depth (%).

Uncertainties are not factored into the Pearson correlation coefficients quoted in Table 5.2. Future work could use additional techniques for correlation that account for uncertainty, e.g., rank order. Such a study could include many more events to maximize the efficacy of the correlation comparison.

5.7 Summary

Positive correlations with a high degree of significance have been found between coronal dimming and CME parameters, providing evidence for our initial hypotheses that 1) dimming slope should be directly proportional to CME velocity, and 2) dimming depth should be directly proportional to CME mass. Existence of the correlation was predicted by physical theory. Linear fits between dimming slope and CME speed and between dimming depth and CME mass are provided in Section 5.6. Additionally, we found that the Fe IX 171 Å dimming corrected for the flare contributions using the Fe XV 284 Å line provides the most accurate dimming results for the EVE data. We note that the uncertainties for coronagraph and dimming parameters are complimentary: there are smaller uncertainties for CME speed than dimming slope, and there are smaller uncertainties for dimming depth than CME mass.

Chapter 6

Overview of MinXSS Solar CubeSat

The Miniature X-ray Solar Spectrometer (MinXSS) is a three-unit (3U) CubeSat developed at the Laboratory for Atmospheric and Space Physics at the University of Colorado, Boulder. Over 40 students contributed to the project with professional mentorship and technical contributions from professors in the Aerospace Engineering Sciences Department at University of Colorado, Boulder and from Laboratory for Atmospheric and Space Physics scientists and engineers. I have personally spent over 4500 hours working on MinXSS at the time of this writing. The scientific objective of MinXSS is to study processes in the dynamic sun, from quiet sun to solar flares, and to further understand how these changes in the sun influence the Earths atmosphere by providing unique spectral measurements of solar soft x rays (SXRs). The study of solar eruptive events such as solar flares is the thread tying this chapter and the next together with preceding chapters.

The enabling technology providing the advanced solar SXR spectral measurements is the Amptek X123, a commercial off-the-shelf silicon drift detector. The Amptek X123 has a low mass (324 g after modification), modest power consumption (2.50 W), and small volume (6.86 x 9.91 x 2.54 cm), making it ideal for a CubeSat. This chapter provides an overview of the MinXSS mission: the science objectives, subsystems, and lessons learned.

6.1 Brief CubeSat Introduction

CubeSats are now becoming a viable vehicle for scientific measurements in space. As commercial entities, government laboratories, and universities continue to miniaturize the requisite

technologies for satellites, the sophistication and size of space-based scientific instruments increases. The University of Colorado, Boulder (CU) and the Laboratory for Atmospheric and Space Physics (LASP), developed the Colorado Student Space Weather Experiment (CSSWE; Li et al. 2012; Gerhardt et al. 2013) three-unit (3U) CubeSat, which launched in 2012 and operated for approximately two years. The science instrument measured high-energy electrons and protons in low Earth orbit (LEO) and has resulted in many peer-reviewed journal articles. The present work builds on this success and takes advantage of new commercially available precision three-axis attitude determination and control to achieve fine target pointing toward the sun. To date, the majority of CubeSats have been technology demonstrations; their goal is to increase the technology readiness level of new technologies and old technologies that have been miniaturized for use in CubeSats. MinXSS (shown in Figure 6.1) is a CubeSat with science as its primary mission. So this chapter starts with science.

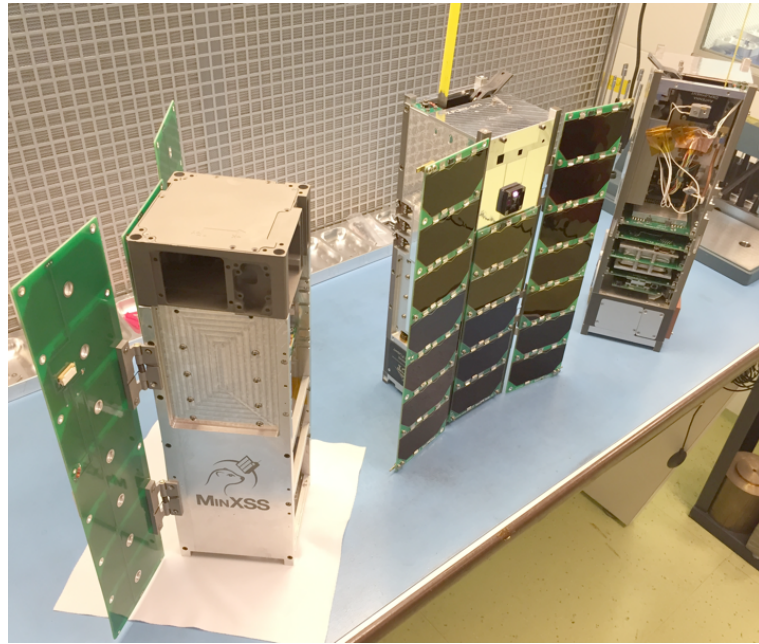


Figure 6.1: Photo of MinXSS family (left to right): prototype unit, flight model (FM)-1, FM-2.

6.2 Science Objectives

There is a rich history of solar SXR spectral observations over the past three decades, but with a significant gap of spectrally resolved measurements in the 0.46 nm range (see Figure 6.2). There were many new discoveries about solar flares during the 1980s using solar SXR spectral measurements from the Department of Defense P78-1, NASA Solar Maximum Mission (SMM), and Japan Aerospace Exploration Agency Hinotori satellites. For example, Doschek (1990) provides results about flare temperatures, electron densities, and elemental abundances for some flares during these missions. A review of flare observations from Yohkoh and the Compton Gamma Ray Observatory (CGRO), for the hard (higher energy) x-ray (HXR) range, is provided in Sterling and Hudson (1997). These earlier missions laid a solid foundation for studies of flare physics and flare spectral variability that the Reuven Ramaty High-Energy Solar Spectroscopic Imager (RHESSI; Lin et al. 2002) and SDO continue today for the HXR and EUV ranges, respectively. Other missions that have contributed to our understanding of the solar x-ray spectrum, as listed in Figure 6.2, include the Solar and Heliospheric Observatory (SOHO) Coronal Diagnostic Spectrometer (CDS), Hinodes EUV Imaging Spectrometer (EIS), GSAT-2s Solar X-ray Spectrometer (SOXS) Cadmium-Zinc-Telluride (CZT) and Si detectors, SMMs Bragg Crystal Spectrometer (BCS) and Flat Crystal Spectrometer (FCS), CGROs Burst and Transient Source Experiment (BATSE), Hinotoris solar Flare Monitor (FLM) and solar Soft X-ray Monitor (HXM), and P78-1s Solar X-rays (SOLEX) and X-ray Monitor (MONEX). With solar flare spectral variability expected to peak near 2 nm (Rodgers et al., 2006), in a range not currently observed by any spectrometer, MinXSS measurements of the solar SXR irradiance will provide a more complete understanding of flare variability in conjunction with measurements from RHESSI and EVE.

There are also nearly four decades of broadband (510 nm wide) SXR measurements not shown in Figure 6.2 because they do not provide spectrally resolved measurements. The very limited spectral information from these broadband measurements cannot quantify the specific spectral energy distribution, nor directly quantify the varying contributions of emission lines (bound-bound) among

the thermal radiative recombination (free-bound) and thermal and non-thermal bremsstrahlung (free-free) continua. These broadband measurements include, among others, the two geostationary operational environmental satellite (GOES) x-ray sensor (XRS) channels covering a combined band of 1.625 keV (0.05-0.8 nm) and the even broader band of 0.212 keV (0.1-7 nm) from several missions, including the Yohkoh soft x-ray telescope (1991-2001; Acton et al. 1999), Student Nitric Oxide Experiment (SNOE, 1998-2002; Bailey et al. 2000), Thermosphere-Ionosphere-Mesosphere Energetics and Dynamics (TIMED, 2002-present; Woods et al. 2005a), the Solar Radiation and Climate Experiment (SORCE, 2003-present; Woods et al. 2005b), and SDO (2010-present). Broadband measurements of solar SXRs have helped to resolve an outstanding difference between ionospheric models and measurements, such as the electron density from the Haystack Observatory incoherent scatter radar at Millstone Hill. In particular, the SNOE solar measurements were able to resolve the factor-of-4 difference between models and measurements because the SNOE data indicated much more SXR irradiance than had been previously thought (Solomon et al., 2001). Additional broadband SXR measurements have been made since then; however, differences still remain in understanding solar SXR spectral distribution and atmospheric photoelectron flux. Although smaller, these discrepancies are still as large as a factor of 2 at some wavelengths, as shown in Figure 6.3; the lack of spectral resolution in the SXR range is thought to be the culprit for most of these disagreements. For example, Peterson et al. (2009) show that discrepancy between photoelectron measurements and models were significantly improved with new EUV spectral measurements down to 6 nm, and we anticipate further improvement with new solar SXR spectral measurements and atmospheric modeling with data from the MinXSS because of its ability to measure all wavelengths in its spectral range simultaneously and with the relatively high spectral resolution of 0.15 keV full-width at half-maximum (FWHM).

6.2.1 Solar Flare Studies

Spectral models of the solar irradiance (e.g., CHIANTI; Dere et al. 1997; Landi et al. 2006) are needed to convert spectrally integrated broadband measurements into irradiance units. Detailed

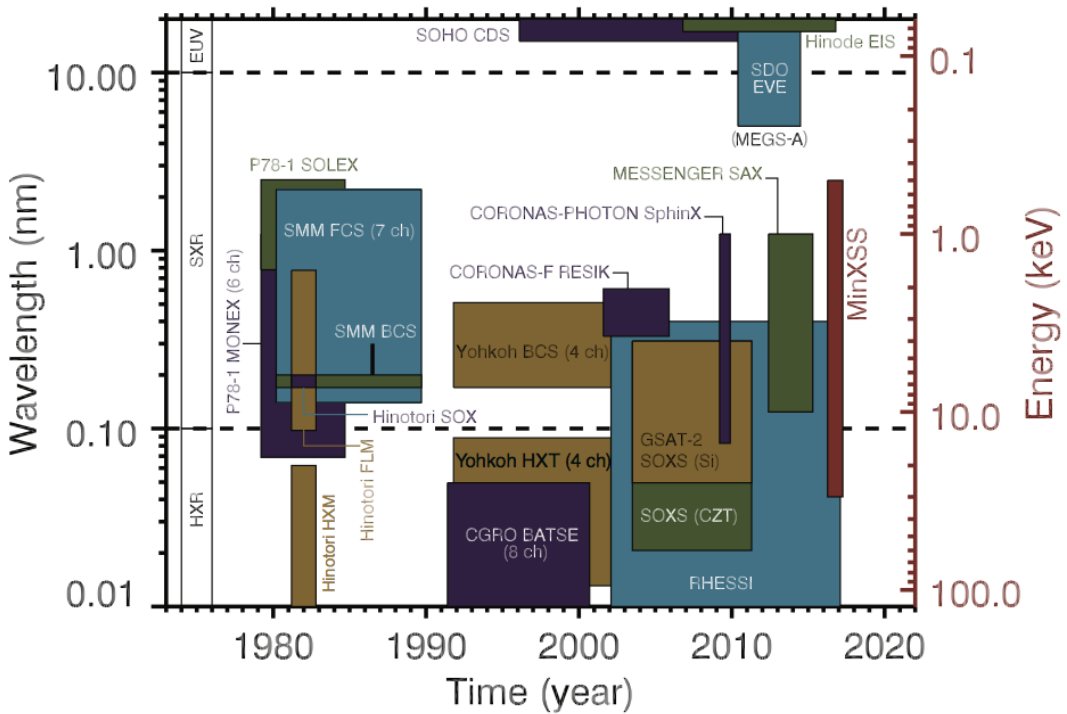


Figure 6.2: History of solar spectral measurements in and near soft x-ray 11 energies (not exhaustive). Figure courtesy of Amir Caspi and Tom Woods.

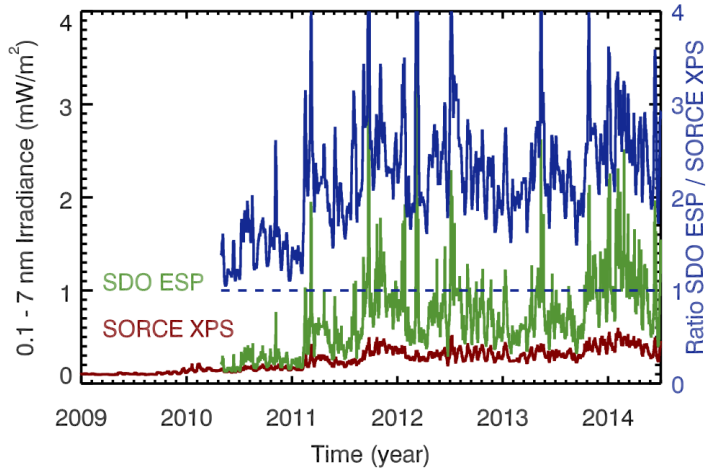


Figure 6.3: Solar 0.17 nm irradiance currently measured by broadband SXR photometers onboard NASAs SORCE and SDO satellites. Figure courtesy of Tom Woods.

modeling to estimate the SXR spectrum during a flare in April 2002 using a set of broadband measurements from the TIMED Solar EUV Experiment (SEE) was performed by Rodgers et al. (2006). The CHIANTI spectral model is part of their analysis and is also routinely used for processing these broadband measurements (e.g., Woods et al. 2008). Although the CHIANTI spectra are scaled to match the broadband SXR irradiance in data processing, there are significant differences for individual emissions lines between the CHIANTI model and observations, often more than a factor of 2 (Woods and Chamberlin, 2009; Caspi and Lin, 2010). Furthermore, there are concerns that CHIANTI could be missing many of the very hot coronal emissions lines, especially in the SXR range where there are so few spectral measurements between 0.5 and 6 nm. Additionally, there are factor of 2 differences when comparing the irradiance results from different broadband instruments, which are worst during times of higher solar activity (Figure 6.3). These discrepancies can be partially explained by wavelength-dependent instrument calibrations, but the greater contribution is likely the lack of knowledge of how this dynamic part of the solar spectrum changes as a function of wavelength and time.

The MinXSS spectrometer, an Amptek X123-SDD, flew on the EVE calibration rocket payload in June 2012, and that measurement had a difference of almost a factor of 8 below 2 nm as compared with the CHIANTI model prediction based on SORCE XPS broadband measurements (Caspi et al., 2015). This rocket result was a surprise considering that the SORCE-based CHIANTI model prediction agreed with SDO/EVE measurements down to 6 nm. Improvement of models of the solar SXR spectra, which is only possible with calibrated spectral measurements of the SXR emission, is critical to properly interpret these broadband measurements. Our goal with MinXSS observations is to reduce these SXR spectral differences from factors of 2 or more down to less than 30%. In addition, the MinXSS will measure solar SXR spectra with higher spectral resolution of 0.15 keV FWHM, as compared with the 0.6 keV FWHM resolution of the most recent analogous instrument, MESSENGER solar assembly for x rays (SAX; Schlemm et al. 2007). The MinXSS measurements will enable improvements to solar spectral models, such as CHIANTI and the Flare Irradiance Spectral Model (FISM; Chamberlin et al. 2007, 2008). By using the MinXSS to im-

prove the FISM predictions in the SXR range, atmospheric studies over the past 30 years will be possible, such as those for the well-studied Halloween 2003 storm period, as well as future space weather events after the MinXSS mission is completed. Getting this spectral distribution of solar flare energy in the SXR range is critical as a driver for atmospheric variations and will be discussed briefly in the next section.

The MinXSS data will also help improve understanding of the physics of solar flares themselves. The 0.5-9 keV (0.13-2.4 nm) range observed by the MinXSS is rich with high-temperature spectral lines from coronal plasma with temperatures from 5 to 50 million K, which are greatly enhanced during even small solar flares. MinXSS will also observe the underlying free-free and free-bound continua, extending out to 20-30 keV, which can provide an independent diagnostic of the emitting plasma temperatures. Understanding how solar flares heat plasma, especially up to many tens of million Kelvin, is a pressing question in solar physics (e.g., Caspi and Lin 2010; Fletcher et al. 2011; Caspi et al. 2014), and the MinXSS observations will provide the best spectral measurements in this energy range to date. Observing the variations of spectral lines in comparison with the continuum will also provide insight into coronal elemental abundances, particularly for Mg, Si, Fe, S, and Ar, to help measure abundances and to understand how they may vary with solar activity and during flares.

6.2.2 Topics Beyond Solar Eruptive Events

Quiescent-Sun Studies Examples of data analysis and spectral modeling for two quiescent (non-flaring) solar measurements made with the X123 aboard the EVE calibration rocket flights in 2012 and 2013 are provided in Caspi et al. (2015). One of the tantalizing results from these two 5 min observations is that the coronal abundance of certain elements is different for the quieter SXR spectrum on 2012 June 23 than the more active (but not flaring) sun on 2013 October 21. These abundance differences suggest that different heating mechanisms occur in the quiet network versus active regions and support the concept that numerous small impulsive events (“nanoflares,” e.g., Rodgers et al. 2006; Parker 1988) could be the source of the active region heating. Identifying

the mechanism responsible for heating the quiet sun corona to millions of degrees, while the photosphere below it is only 6000 K, remains one of the fundamental outstanding problems in solar physics (Klimchuk, 2006). We anticipate that one to three months of MinXSS measurements of the solar SXR spectrum will provide adequate data on active region evolution and several flares to more fully address these questions on nanoflare heating. The SXR variability is about a factor of 100-1000 over the solar cycle and can be as much as a factor of 10,000 for the largest X-class flares.

Improvements to Earth Atmospheric Models Energy from SXR radiation is deposited mostly in the ionospheric E region, from 80 to 150 km, but the altitude is strongly dependent on the incident solar SXR spectrum. This wavelength dependence is because of the steep slope and structure of the photoionization cross sections of atmospheric constituents in this wavelength range. The main reason that Earth's atmospheric cross section changes so dramatically in this range is because of the K edges of O at 0.53 keV (2.3 nm) and of N at 0.4 keV (3.1 nm). The distribution of energy in solar SXRs, even while holding total energy constant, results in peak energy deposition in Earth's atmosphere to change in altitude. The peak energy is near the mesopause but can vary by more than 5 km. This separation is considered significant because it is approximately equal to the scale height at 100 km, it is critical to E-region electrodynamics, and the mesopause (the coldest region of the atmosphere) is a critical transition between the middle and upper atmosphere.

6.3 Mission Architecture

All standard satellite subsystems are present on the MinXSS CubeSat, except for propulsion. Each will be overviewed in the following sections. Figure 6.4 shows the requirements flowdown from the science objectives to the mission level requirements, along with the expected performance of the system on orbit. Figure 6.5 shows the mechanical block diagram, and Appendix B shows the resource break-down of the spacecraft subsystems. Volume is only approximate because many components have nonstandard geometries. The 4800 g mass limit is derived from the interface control document for the NanoRacks CubeSat Deployer. The measurement requirement for range corresponds to the ISO standard definition for SXRs, and MinXSS is only required to make mea-

surements that fall somewhere within this range. The mission expectations listed are for FM-1 (ISS NanoRacks) only. The more conservative standard mass limit for a 3U CubeSat from the California Polytechnic State University CubeSat design specification is 4000 g and would result in a mass margin of 15% for the MinXSS.

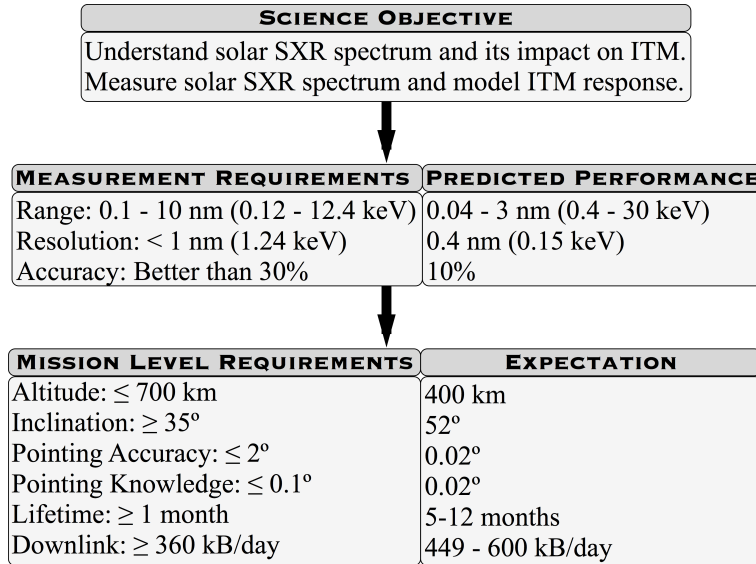


Figure 6.4: High-level requirements flowdown for MinXSS.

6.3.1 Primary Instrument: Amptek X123-SDD

The purpose of the primary MinXSS science instrument is to measure solar spectra within the International Organization for Standardization (ISO) standard SXR range of 0.1-10 nm listed in the requirements flowdown (Figure 6.4). To function within a CubeSat, the instrument must be low mass, low power, and have a small volume. A commercial off-the-shelf solution perfectly met these design requirements. The Amptek X123-SDD weighs 324 g after custom modifications were made for mounting to the CubeSat and thermal foam was added for cooling electrical components in vacuum. It consumes approximately 2.5 W of power nominally, and 5.0 W for approximately 1 min when first powered on. Much of the power draw (including the initial transient) results from the integrated thermoelectric cooler (TEC) reducing the temperature of the SDD to the user-

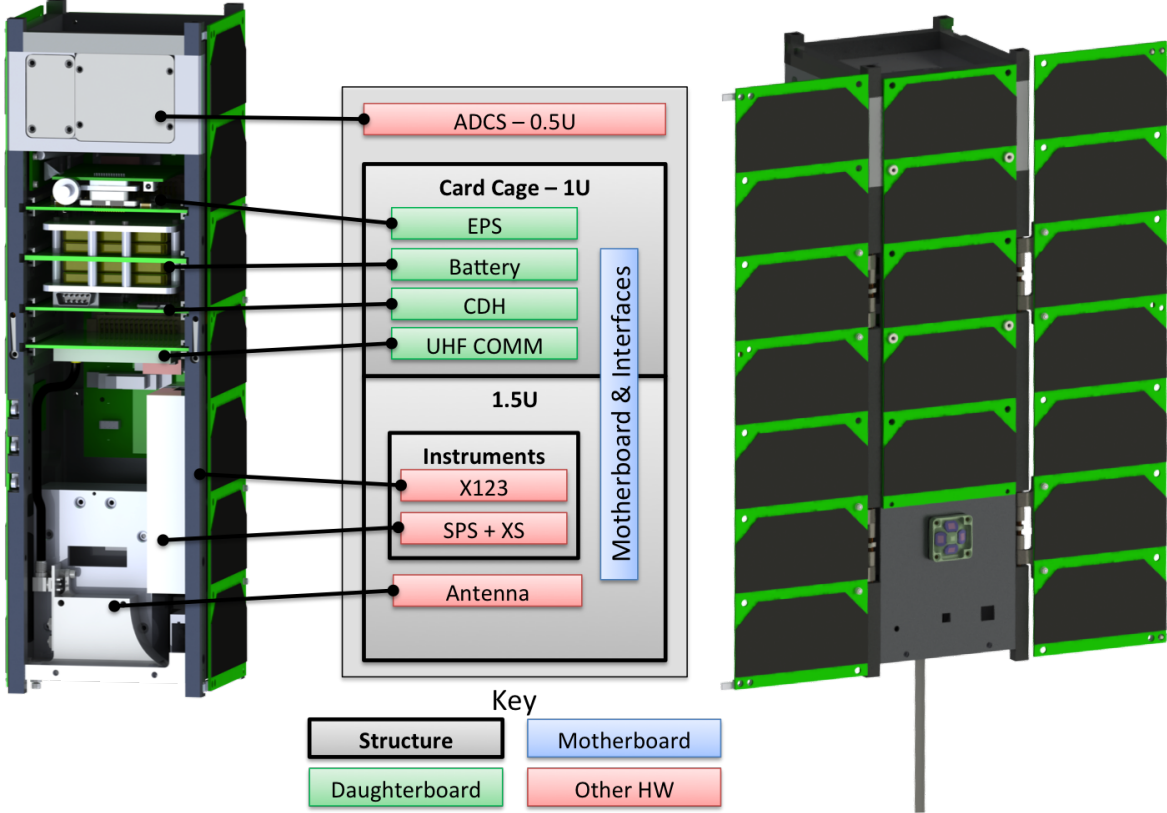


Figure 6.5: MinXSS CubeSat mechanical block diagram.

defined set point (-50 °C for the MinXSS). The dimensions of the X123 are also sufficiently small to easily fit within a CubeSat because of the manufacturers designed purpose as a handheld SXR measurement unit for geological fieldwork. The X123-SDD's 500 m active thickness and 16 m beryllium (Be) entrance window define a spectral range sensitivity of 0.430 keV (0.043 nm), which covers the primary range of interest for scientific studies of 0.52 nm. The instrument includes all the necessary processing electronics, including an integrated multichannel analyzer, to produce a spectrum that is output via an RS232 interface. It can also be commanded programmatically to change numerous parameters, such as integration time and energy thresholds. The custom modifications for spaceflight include staking the larger electronics components, adding a mounting plate for the electronics, adding a custom interface cable and 9-pin connector, adding a tungsten plate with pinhole aperture for the SDD, and providing stainless steel radiation shielding around

the aluminum detector vacuum housing.

In October 2014, the MinXSS science instruments, including the X123, were calibrated at the National Institute of Standards and Technology (NIST) Synchrotron Ultraviolet Radiation Facility (SURF; Arp et al. 2011). The synchrotron radiation provides a calibrated continuum emission source, with a radiometric accuracy of 10% in the SXR range. The SURF electron storage ring beam energy is adjustable from 60 to 416 MeV; the synchrotron spectral distribution is dependent on the beam energy, and the MinXSS calibrations use the higher beam energies to maximize the incident SXR flux. The absolute radiometric calibration of the X123, as a function of wavelength, is then obtained by comparing the measured output spectra with the known incident photon flux from the SURF beam; an example, and further description, can be found in Caspi et al. (2015). The narrow spatial extent of the SURF beam in the x-ray range allows for a mechanical determination of the instrument optical axis (“bore-sight”) relative to a reference frame, and the uniformity of response over the instrument’s field of view (FOV) is determined using a gimbal system to rotate the detector optical axis about the incident beam. The nonlinearity of the detector electronics is measured by adjusting the intensity of the incident synchrotron flux.

6.3.2 Secondary Instrument: Solar Position Sensor and X-Ray Sensor

The purpose of the secondary instrument is to provide support for scientific analysis of data from the primary instrument. Two sensors are needed to achieve this: one to provide independent high-precision attitude knowledge of the solar position and another to provide an in-flight SXR irradiance reference. Again, these instruments must be low mass, low power, and small volume to be accommodated within a CubeSat platform. MinXSS heavily leveraged instrument heritage from the larger GOES-R EUV x-ray irradiance sensor development at LASP, which already met all of these requirements. The custom-designed application specific integrated circuit (ASIC), in particular, provides the backbone of this exceptionally low-power, low-noise system. A custom mechanical design for the casing was necessary to integrate the subsystem with the MinXSS, which was manufactured for flight using aluminum sintering (3-D) printing.

Figure 6.6 shows an exploded mechanical view of this secondary instrument. The solar position sensor (SPS) is a quad-diode with effective neutral-density-7 filter and 2 mm^2 knife-edge aperture, with an FOV of 4° . The solar visible light falls on the four diodes such that the illumination on each diode depends on the incoming angle of the solar radiation. The resultant measurements are used to compute the sun's position to better than 1 arcmin (3σ) as described in Chamberlin et al. (2009). These data are sent to the attitude determination and control system (ADCS) for inclusion in the fine-attitude control solution and telemetered to the ground for use in science processing. The x-ray sensor (XS) is a single diode with two Be foil filters, whose total $16 \mu\text{m}$ thickness is matched to the X123 to define a response over the same 0.04-3 nm wavelength range. XS has a 5.0 mm diameter knife-edge aperture and an FOV of 4° . The diode operates in photocurrent mode, integrating the total SXR flux over its band-pass and integration period; this provides a measurement that can be compared with the integrated X123 spectrum, to within measurement and calibration uncertainties. These data are also telemetered to the ground for use in science data processing.

The SPS and XS were also calibrated at SURF. The SPS optical axis and the transfer equation relating off-axis position to quad-diode output were determined using the gimbal system to rotate the optical axis around the incident SURF beam. The XS optical axis and uniformity of response over its FOV were similarly determined. The absolute radiometric response of the XS was determined similarly to the X123, comparing the known incident synchrotron photon flux with the output from the photodiode. (No absolute calibration was necessary for the SPS.) The SPS and XS system, including ASIC, had been previously measured to be highly linear through testing during GOES-R development, and so the MinXSS calibrations omitted nonlinearity testing.

6.3.3 CDH and Flight Software

The core of the MinXSS CDH subsystem is a low-power Microchip dsPIC33 Microcontroller Unit (MC dsPIC33EP512MU810). The CDH communicates with and controls the X123 instrument, UHF communications, and ADCS via RS232, monitors voltages, currents, and temperatures

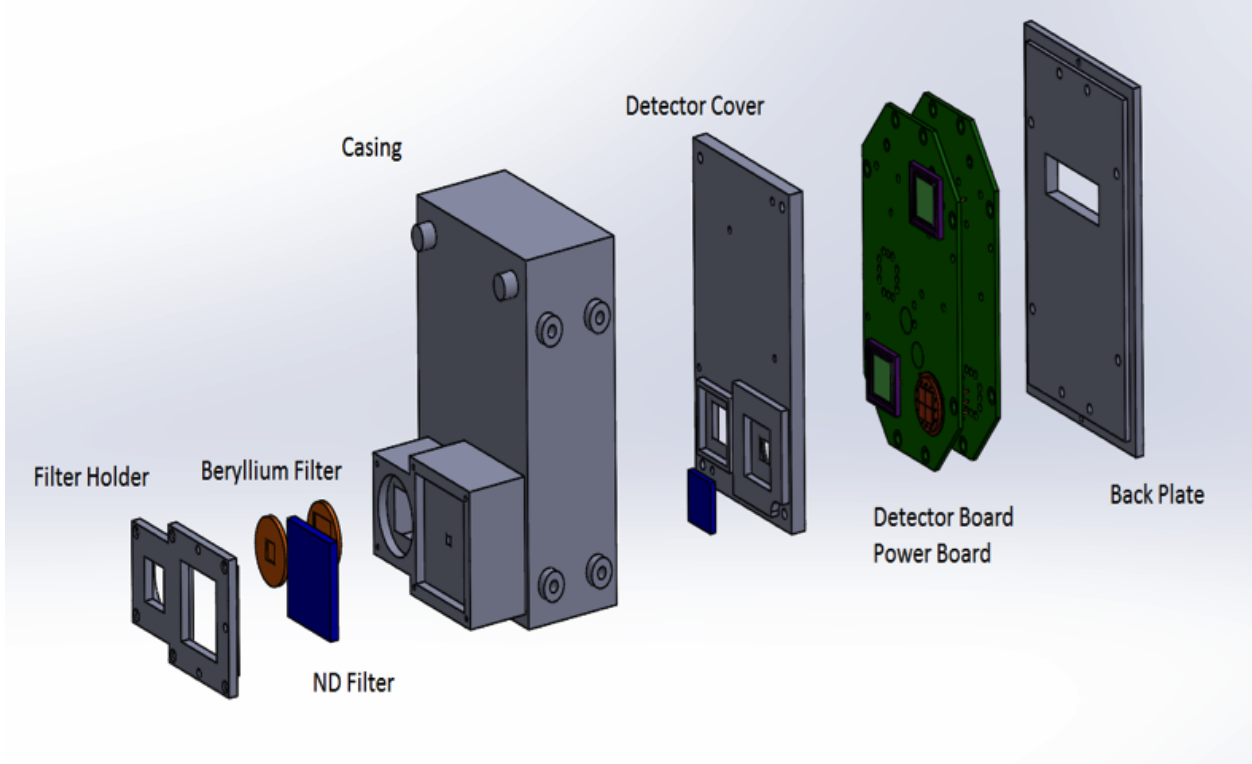


Figure 6.6: Solar position sensor and x-ray sensor (SPS and XS) exploded view. Figure courtesy of Siddhesh Naik.

via I2C for the motherboard, CDH, communications, EPS, and SPS and XS, and reads detector data from the SPS and XS ASIC via digital input/output. Additionally, the CDH handles all incoming commands, housekeeping monitoring, data manipulation for downlinking data packets, power switching of subsystems, and configuration of the operation modes. Most of the CDH operation is configurable via uplinked command, and several of these CDH processes are autonomous for maintaining a safe power configuration. Data are stored on a 4 GB secure digital (SD) memory card, and each type of data packet has its own dedicated circular buffer on the SD card. This SD card can store more than 1400 days (3.8 years) of science, housekeeping, and log message data packets, and 48 h of ADCS high-rate data packets. The dsPIC33 internal real-time clock (RTC) and an external RTC integrated circuit (IC) provide precise time knowledge. The external RTC IC also has an electrically erasable programmable read-only memory for storing startup configuration

parameters, which can be modified via uplinked commands. The dsPIC33 watchdog timer is used to initiate a reset of the system in case it becomes unresponsive, and a reset command can also be sent from the ground. The MinXSS FM-1 one year mission worst-case radiation dose estimate is 2.6 krad, with a minimum shielding of 2 mm of Al provided by the CubeSat structure. Two of the prototype CDH boards successfully passed radiation tests of 10 krad and 25 krad.

The embedded flight software is built on a Slot Real-Time Operating System (RTOS), written in C, as originally developed at LASP for the EVE rocket experiment. The key elements of the software design are robustness and simplicity, with the health and safety of the satellite as top priority. Because many of the tasks performed by the CDH are not time sensitive and can be handled at any time in the slot process, the real-time demands on the CDH and flight software are very low. The RTOS uses the dsPIC33 timer with 1 ms resolution for execution of tasks, but most monitoring by the CDH has a cadence of 1 s or slower.

6.3.4 Electrical Power System, Battery, and Solar Panels

The MinXSS EPS is largely based on heritage from the successful CSSWE direct energy transfer (DET) design. The EPS uses high-efficiency buck converters for power regulation to 3.3 and 5.0 V and a simple battery charging logic for use with Li-polymer batteries. Minor design modifications were incorporated to accommodate the higher power generation and consumption on the MinXSS as compared with CSSWE, as well as more voltage and current monitors. Two additional major differences were implemented: pseudo-peak power tracking (see Section 6.4.4) and additional switches to prevent the system being powered before deployment to comply with NanoRacks ISS human safety standards.

The battery pack consists of four SparkFun 2-Ah Li-polymer batteries, configured as two parallel sets of two batteries in series to provide a 6-8.4 V unregulated 4-Ah bus; two temperature sensors, and two heaters, which are sandwiched between the batteries. Heat transfer tape was used between each layer of the battery pack to achieve a homogenous temperature distribution during flight. The PCB in the middle of the pack does not have a copper plane in its center as all other

daughterboards do, the intent being to thermally isolate the batteries from the rest of the system. This was a part of the passive thermal design to create a battery-dedicated thermal zone, because the batteries have the narrowest operating temperature range of all components in the system. Finally, the pack was encapsulated with aluminum plates on standoffs, providing sufficient volume for the batteries to expand under vacuum and thermal cycling. Arathane 5753 with Cabosil glass beads was placed between the batteries and these encapsulation elements to act as a soft bumper to expanding batteries.

MinXSS uses 19 triple-junction GaAs, 30% efficient solar cells from Azur Space Solar Power, GmbH. One five-cell solar panel is fixed to the body of the CubeSat on the solar-oriented side, and two seven-cell solar panels will deploy by command to have the same solar orientation as the body-fixed panel. Because MinXSS is a sun-pointed spacecraft, these solar panels can nominally supply 22 W at end-of-life during the orbit insulation period. A 100 hour mission simulation test with the fully integrated spacecraft connected to a solar array simulator under various eclipse periods was performed to verify that there is adequate margin for operating all of the MinXSS subsystems and for charging the battery (see Section 6.4.5). Additionally, flight software incorporated the ability to autonomously power off the X123 (the largest power consuming subsystem) and the other non-critical subsystems during eclipse if there are any battery power issues for eclipse operations. The power-cycling flags can be enabled via command, but we do not anticipate the need for their use.

6.3.5 Communications

MinXSS leveraged heritage from the CSSWE CubeSat by using the same radio and ground station for UHF communications. The ground station is located on the roof of the LASP Space Technology Research Building in Boulder. It consists of a pair of M2 436CP42 cross Yagi antennas, each with a gain of 17 dB_{dc} and a circular beamwidth of 21°. A Yaesu G5500 azimuth-elevation rotator controlled by SatPC32 points the antenna system. SatPC32 also accounts for Doppler shifts via its control of the ground radio, a Kenwood TS-200. The antennas and motors are mounted on an 2.4 m tower and are connected to the electronics in the control room below by 60 m low-loss cabling,

which accrues 5.4 dBm of RF signal loss. The flight radio is an Astronautical Development, LLC Lithium-1 radio that operates in the UHF band at 437 MHz. Additionally, the antenna is nearly identical to that used on CSSWE, which is a deployable spring steel tape measure with a length of 47.6 cm. The gain pattern was measured using the MinXSS prototype in an anechoic chamber at First RF Corporation in Boulder, Colorado. The measurements were compared with a FEKO model and propagated through Satellite Tool Kit to estimate the expected daily average downlink data capacity: 600 kB day^{-1} using the FEKO model or 449 kB day^{-1} using the measurements. These estimates are not highly precise because of the limited fidelity of the model and the prototype structure, but provide an idea of what to expect. The requirement of at least 360 kB day^{-1} appears to be easily satisfied.

6.3.6 Attitude Determination and Control System

To provide a stable view of the sun for the science observations and to maintain appropriate antenna orientation during ground contacts, MinXSS has an active ADCS. With the wide field of view of the X123 (4°), the pointing requirements for MinXSS are only $2^\circ(3\sigma)$ accuracy and $0.1^\circ(3\sigma)$ knowledge.

The commercial CubeSat ADCS onboard the MinXSS is a flexible ADCS CubeSat technology (XACT) from Blue Canyon Technologies (BCT). BCT has developed a 0.5 U-sized ADCS unit (0.85 kg) using miniature reaction wheels, torque rods, a star tracker, a coarse sun sensor, inertial measurement units, and magnetometers. The BCT XACT is expected to provide pointing accuracy and knowledge of better than $0.003^\circ(1\sigma)$ in two axes, corresponding to the plane of sky of the star tracker, and $0.007^\circ(1\sigma)$ in the third axis, parallel to the star tracker optical axis. The XACT interface uses 5 and 12 V power inputs (1.0 W nominal, 2.8 W peak) and serial communication (RS232 for the MinXSS, but other options are available). SPS provides two-axis (pitch/yaw) pointing knowledge on the sun to better than 1 arcmin (3σ), which can be sent to the XACT for closed-loop fine-sun pointing; however, the XACT system can easily meet the MinXSS pointing requirements without this additional knowledge.

After integration with MinXSS, multiple tests were performed to verify functionality and performance of the ADCS. A custom air-bearing table was built to provide a relatively torque-free environment for the ADCS to control the spacecraft. For example, we verified that the spacecraft can track the sun with a heliostat at LASP, that magnetometers reversed sign when the spacecraft was rotated 180° in each axis, that torque rods produced a measurable magnetic field, and that the star tracker took interpretable images and found matches to stars in its library when observing the night sky.

6.4 Advancing CubeSat Technologies and Lessons Learned

6.4.1 CubeSat Card Cage



Figure 6.7: Prototype CubeSat card cage design. Figure courtesy of Tom Woods.

Experience with the PC104 PCB interface on the CSSWE CubeSat led the MinXSS team away from the card stack design because of the difficulty in debugging boards once integrated. Instead, the CubeSat card cage design uses a motherboard/daughterboard architecture that allows any individual card to be easily removed, and an extender board optionally inserted to have access

to the daughterboard for probing while still electrically connected (Figure 6.7). Additionally, the standard electrical interface allows boards to be swapped to any position. MinXSS uses a DIN 48-pin connector for the daughterboard/motherboard interface. This relatively large connector was chosen for ease of soldering for new engineering students and because it easily satisfied the requirements on the number of necessary pins and mechanical dimensions. In the future, a higher density connector with potentially more pins could be chosen to provide a lower mass and lower volume solution while still providing the flexibility of the card cage architecture.

6.4.2 3-D Printed Parts

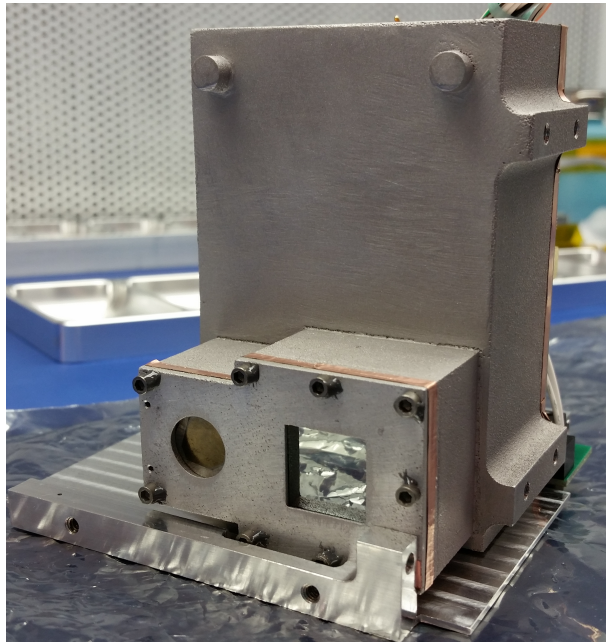


Figure 6.8: Aluminum 3-D printed SPS and XS housing after sanding and integration.

The MinXSS project used 3-D printed parts for both prototyping and flight components. For prototyping, the SPS and XS housing was 3-D printed in plastic twice as the design iterated, and the solar array hinges were printed in plastic once. This was done using CU's Objet 30 printer with VeroWhitePlus plastic. For flight, these same components were 3-D printed in metal using direct metal laser sintering at GPI Prototype. The SPS and XS housing is aluminum with a shot-blasted

finish (Figure 6.8). This finish was very rough and required significant sanding to get an acceptable surface finish and clean edges. The solar array hinges are stainless steel with a shot-blasted finish (Figure 6.9). A minimal amount of sanding was required for these parts because the requirements were looser and the finish was slightly better than SPS and XS. The better finish was likely because of the hinges being a simpler part that required no filler material during the 3-D print (sintering) process.

As plastic 3-D printers become more pervasive, affordable, and precise, the draw toward using the resultant parts for flight is becoming stronger. A major risk that must be addressed is the unknown properties of these materials, particularly in their response to vacuum and UV exposure. We would like to see an open database where specifications based on test results for common 3-D print materials, such as ABS and PLA, could be accessed.



Figure 6.9: Stainless steel 3-D printed solar array hinges as delivered from vendor.

6.4.3 Simplification of Solar Panel Fabrication Process

CSSWE used epoxy (Arathane 5753) on the back of solar cells to adhere them to the solar panel PCBs. This technique is typical but requires significant assembly and curing time. MinXSS used double-sided Kapton tape with acrylic adhesive to adhere solar cells to the PCBs. We used a specialized rubber vacuum sealer to apply pressure to the cells uniformly and meet the manu-

facturers recommended application pressure. This reduced the time to produce a solar panel from three days to one day. To get electrical conductivity from the back of the solar cell to the PCB, we applied silver epoxy in large vias behind each cell. We also tested a new-to-market tape: 3M Z-axis tape. This tape is electrically conductive between the adhesive and backside and could save the extra step of applying the silver epoxy or soldering/welding on tabs. For flight, Kapton tape was used because 1) the Z-axis tape adhesive was not rated for as wide a temperature range as the Kapton acrylic adhesive, 2) there was concern that the Z-axis tape could not sustain the high current of the solar cells for as long as solder or silver epoxy could, and 3) the Z-axis tape thermal conductivity properties were not specified in the datasheet. In the future, we would like to see solar cell manufacturers adopt a standard form factor compatible with CubeSats. MinXSS uses 40 x 80 mm cells from Azur Space (Figure 6.10), which are a great fit within the rail boundaries of CubeSats (maximum of 83 mm wide and 340.5 mm long for 3U CubeSat). The 80 mm width for cells provides a 1.5 mm margin on each side from the rails. If the spacing between cells could be reduced to 4.5 mm or less, then there could be eight Azur Space solar cells instead of seven on a 3U panel. Alternatively, if the height of the cells were changed to be 50 mm instead of 40 mm, then they would be more modular for fitting one solar cell per 0.5U of the panel length. With six 50 x 80 mm cells instead of seven 40 x 80 mm cells, there could be 7% more power per 3U panel.

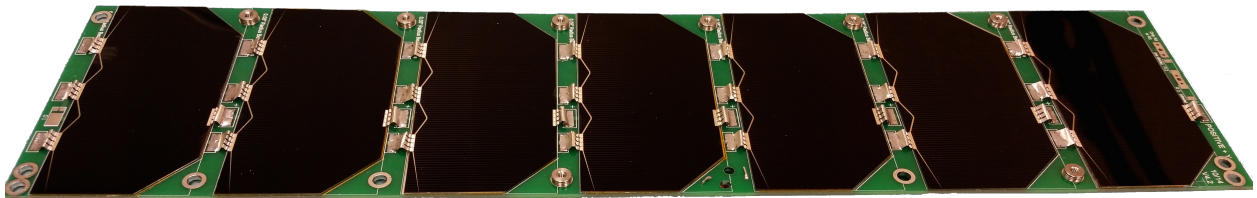


Figure 6.10: Populated seven-cell deployable solar array for MinXSS FM-1.

6.4.4 Pseudo-Peak Power Tracking

A modified DET EPS design was implemented on MinXSS that was inherited from the CSSWE CubeSat to include an additional specially selected resistor to create a pseudo-peak power

tracking (PPPT) system. The extra resistor was chosen to prevent a rapid voltage drop from the solar cells when the battery attempts to draw a large current, namely, when the battery state of charge is relatively low right as the spacecraft exits the orbit eclipse.

In the CSSWE and MinXSS EPS design, the output of the solar panels power 8.6 V regulators that then provide regulated 8.5 V power directly to the battery and system. In this DET design, the batteries will charge up to 8.5 V, and there are no supporting electronics required to control the battery charging process. In reality, this simple approach only provides about 50% of the power intended from the solar panels when the battery capacity is low. In particular, when the battery needs more power input (high current) for charging, the high current draw from the solar cells results in much lower voltage, following the standard solar cell current-voltage I-V curve. When the solar panel output voltage goes below the minimum input voltage level of the 8.6 V regulator, the regulator turns off. Consequently, the current drops and the solar panel output voltage increases, and the 8.6 V regulator turns back on. This results in a high-frequency on-off regulator oscillation that had the EPS 8.6 V regulators on for only about 50% of the time during the early part of the orbit dayside during mission simulations. The MinXSS solar panels were designed for 80% of peak efficiency at EOL, but the 50% decrease in power was an unacceptable power loss for the nominal power budget.

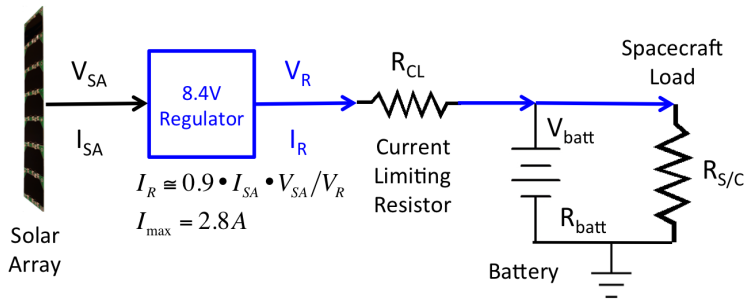


Figure 6.11: Simplified circuit diagram of PPPT for MinXSS EPS. Figure courtesy of Tom Woods.

The solution for MinXSS, without having to redesign or rebuild the EPS board, was to replace the sense resistor on the output of the solar panel regulator with a larger resistance so

that the effective current draw out of the solar panel would be limited and thus would not cause the regulator to turn off. We refer to this current-limiting resistor for the solar panels as PPPT. Figure 6.11 shows a simplified version of the PPPT circuit for the MinXSS EPS. The value for this current-limiting resistor was estimated for the MinXSS power configuration using Equation 6.1.

$$I_{Reg} = \frac{V_{Reg} - I_{max}R_{CL}}{R_{S/C}} + \frac{V_{Reg} - I_{max}R_{CL} - V_{Batt}}{R_{CL} + R_{Batt}} \quad (6.1)$$

where I_{Reg} is the current output from the regulating buck converter, V_{Reg} is the corresponding voltage, I_{max} is the maximum current from the solar panel, R_{CL} is the resistance of the current-limiting resistor for pseudo-peak power tracking, $R_{S/C}$ is the spacecraft load, V_{Batt} is the voltage of the battery pack, and R_{Batt} is the resistance of the battery pack.

The first term on the right-hand side of Equation 6.1 is the current for the spacecraft load, and the second term is the current for charging the battery. The spacecraft load is assumed to be constant, but the battery charging current starts off high when the battery voltage is low and then ramps down to zero when the battery voltage is the same as the regulator voltage downstream of the current-limiting resistor. The ideal value for the current-limiting resistor R_{CL} is such that it limits the current out of the regulator I_{Reg} to be less than the maximum current I_{max} possible from the regulator (at the peak power part of the solar panel I-V curve) and when the battery voltage V_{batt} is at the lowest allowed level. For MinXSS design and configuration, the regulator voltage V_{Reg} is 8.5 V, the worst-case system load (largest power) has 7.0 Ω for R_{SC} , a battery impedance of 0.125 Ω, and a value of 2.8 A for I_{max} . The goal for MinXSS was to keep the battery voltage above 7.1 V at all times, and so an R_{CL} of 0.25 Ω is the desired value for the MinXSS configuration to satisfy Equation 6.1. That is, with this value of R_{CL} , I_{Reg} equals I_{max} when V_{batt} equals 7.1 V. After the current-limiting resistor was installed into the EPS, additional mission simulations were run. We verified that the prediction of the regulator current I_{Reg} and the measured battery voltage agreed with the measured regulator current.

One disadvantage to the PPPT implementation is that there is additional heating of the

EPS board because of the larger resistance; however, this extra heating peaks right after exiting eclipse, the precise time when temperatures are cooler and heating is desired anyway. For example, the power loss (heating) in the PPPT current-limiting resistor is estimated to be 2.6 W when the battery voltage is at its lowest value of 7.1 V, decreasing to 0.93 W when the battery voltage is at 7.5 V, and reduces to less than 0.1 W once the battery voltage is above 8.0 V. The primary caveat in the PPPT design is that resistor tuning must be done a priori, and is fixed, whereas maximum PPT (MPPT) systems can tune resistance in real time to maintain the maximum power point on the solar cell I-V curve. The trade studies performed for CSSWE and MinXSS resulted in the selection of a custom DET EPS because of the simplicity of design. Both teams were unaware of the consequential loss of power generation at the time of the original designs. The advantage of the PPPT circuit is that it is only minimally more complex than DET, adding little risk for a large benefit.

In the future, we would like to see a standard MPPT IC for interfacing to common CubeSat battery packs (e.g., 8.4 V Li-polymer battery packs). We found it difficult to identify a commercial MPPT IC or proven MPPT circuit that could be integrated with our system. We purchased the most promising MPPT IC, a Linear Technology LT3652, and spent significant time attempting to integrate it with the MinXSS EPS, but its intended use prevented proper functioning for our solar panel and battery configuration.

6.4.5 Importance of Flight Like Testing

Various tests were performed on MinXSS that were geared toward simulating the orbital environment and flight-like operations. These included low-external-torque tests of the ADCS, thermal vacuum with a long-duration mission simulation, early orbit end-to-end communication testing performed several miles away from the ground station, and detailed battery characterization of the actual batteries to be flown.

Using a custom-built air-bearing table, we tested the functionality and performance of the ADCS. This test simulated an orbital environment with reduced external torques present. Through

this testing, we discovered that an operational amplifier (op-amp) was preventing the XACT coarse sun sensor from being properly read by its internal flight software, and this op-amp was replaced to resolve this issue. It is unlikely this would have been discovered otherwise and may have resulted in the spacecraft not being able to quickly find or accurately track the sun while on orbit. Significant effort in mission operations may have been able to salvage the mission in that situation, but only minor effort was required to replace the offending op-amp. Air-bearing testing requires very careful balancing of the system and as much reduction of external torques as possible (e.g., even airflow from building ventilation could limit the tracking duration while operating on the air-bearing table). It also requires the computation of moments of inertia specific to the air-bearing CubeSat system to be provided to the ADCS for appropriate control to be implemented. Without such an update to the ADCS software, the ADCS response is too sluggish (slow) to confirm that the ADCS is tracking as expected.

Thermal vacuum tests are irreplaceable for determining if the CubeSat can function in vacuum and for measuring performance near the operational limits of components. Through such testing of MinXSS, we discovered a short in a battery heater that reset the entire system every few seconds, which only manifested under vacuum. This was caused by the battery expansion, which created an unintended electrical connection between the two nodes of the heater. Typically, CubeSats are only required to bake out, not perform a functional thermal vacuum test, but we highly recommend this test as a process to increase the success rate of CubeSats.

A 100 hour mission simulation test was performed on MinXSS during four of the eight hot/cold cycles of the thermal vacuum testing. A solar array simulator, with an I-V curve programmed to model the Azur Space solar cells used on the MinXSS, was jumpered into the MinXSS EPS board. The jumper bypassed the two deployable solar panels. The output of the solar array simulator was programmatically cycled in intervals corresponding to ISS orbit insolation/eclipse periods at three different β angles. The total orbit period was 93 min and the three eclipse periods were 28 min (average β), 38 min ($\beta = 0^\circ$), and 0 min ($\beta > 76^\circ$). Power performance data were collected for the entire system throughout each of these scenarios and verified that the PPPT maintained a power

positive state through many orbits. Additionally, this test was used to verify the functionality of a flight software commandable flag to disable power to the X123 during eclipse periods. This option was introduced into the flight software early in the project in anticipation of a marginal power balance. The X123 was chosen for power cycling because it is the largest consumer of power and because the primary science target (the sun) is not visible in eclipse. However, this is not the default state in the mission design because it introduces excessive power cycling on the primary science instrument; nominal operations leave the X123 powered on during the entire orbit. As the spacecraft performance degrades on orbit (e.g., solar cell efficiency loss), it may become necessary to enable the X123-eclipse-power-cycling flag. Finally, the 100 hour mission simulation test included periodic stored-data downlinking with durations equivalent to the ground station contacts expected on orbit. The 100 hour mission simulation test was the most flight-like testing possible with the facilities available and greatly increased confidence in and understanding of the system as it will behave on orbit. It also ensured that the flight electronics are likely past the “infant mortality” phase.

End-to-end testing was also performed on the MinXSS to verify functionality of the full communication pipeline. The spacecraft was taken several miles away to a position in the line-of-sight of the ground station, and early orbit commissioning tests were performed. This boosted confidence in several areas: that we would meet the NanoRacks requirement of not deploying the MinXSS antenna or solar arrays in the first 30 min after deployment from the ISS, that those deployments would be successful, that communications could be established after antenna deployment, and that our ground software commissioning scripts could autonomously perform telemetry verification and commanding.

Significant battery testing was performed to comply with requirements flowed down from NASA Johnson Space Center through NanoRacks to all CubeSats going to the ISS. These requirements are in place to protect astronauts on the ISS and far exceed the standard CubeSat requirements in the California Polytechnic State University CubeSat Design Specification. Nevertheless, we recommend that all CubeSats perform several of these tests, if only to better understand

the actual batteries to be flown (i.e., not just batteries from the same lot or of the same type). We found the following to be the most useful tests: visual inspection for dents or leaks, measuring the open circuit voltage of the fully configured battery pack, recording voltage, current, and temperature through three charge/discharge cycles; measuring the voltages at which overcharge and overdischarge protection activated and deactivated; and measuring mass before and after undergoing vacuum. Given availability of the equipment to perform these tests and measurements, it took approximately two weeks to complete this testing for each battery pack. Much of that time was dedicated to setup, waiting for charge cycles to complete, and interpretation of the results. Additional tests were required for astronaut safety on the ISS, but we would consider them to be extraneous for non-ISS CubeSat missions. These include measuring of the physical dimensions of each battery, measuring the closed circuit voltage of the fully configured battery pack, measuring the time to trigger short-circuit protection and maintaining the short for 3 hours to verify the protection remains enabled; and doing a dedicated vibration test at five frequencies and strengths up to $9.65\ g_{rms}$ on all three axes, with voltage measurements between each axis. These additional tests took several weeks of additional time and planning, particularly in the design, manufacturing, and modification of components to support vibration testing.

6.4.6 Importance of a Second CubeSat Unit

The fabrication of two identical sets of hardware in parallel is much less expensive than the same development in series, particularly if the start of the development for the second set is delayed by months or years. Small projects tend to have less stringent requirements on documentation, and so details can be forgotten and lost in the time between two sets of flight hardware developed in series. Having two sets of hardware enables the development and testing of flight software, while other activities proceed in parallel. It is important to note that parallel development also enables the replacement of a subsystem if a problem is found, which is critical when schedules are tight. This was the case for the MinXSS when the battery heater short was discovered in FM-1 at the initial pump down for its thermal vacuum test. We were delayed half a day to swap the battery

pack out with FM-2, which did not have the same issue, as compared with the weeks of delay that would have been introduced if an entirely new battery pack had to be assembled and tested. Finally, having a second flight unit allows for debugging of hardware and software after delivery and launch of the first flight unit.

6.4.7 Low-Cost Mitigation of Radiation Issues for Electronics

The CubeSats developed at CU and LASP have generally used industrial-grade (automobile) electronic parts because those parts have wider operating temperature ranges. Typically, the automobile-grade ICs cost \$ 10 as compared with \$ 2 for standard commercial ICs, but this additional cost is outweighed by the significant benefits of the higher-grade components. For example, the number of uncorrupted SD card write cycles can be improved by a factor of 10100, and the operational temperature range can be expanded by purchasing a \$ 70 4 GB hardened SD card instead of a \$ 4 standard SD card. The total cost impact on the MinXSS for these industrial-grade electronics parts is only a few thousand dollars, a small fraction of the total budget, but it significantly improves the potential for a longer mission life. Although our intention was to have electronics that could operate over a wider temperature range, automobile-grade parts may also help with radiation tolerance of the electronics. Two MinXSS prototype CDH boards were radiation tested, one to 10 krad and another to 25 krad; both boards survived. It is not clear if industrial-grade parts made a difference or not for passing the harder radiation test; nonetheless, it is only a small cost increment to use the higher-grade parts.

6.5 Summary

CubeSat technologies and capabilities are now sufficiently mature to enable peer-review journal-quality science missions. This was clearly proven with the CSSWE CubeSat, which has 17 such articles to date (Li et al., 2012; Gerhardt et al., 2013; Li et al., 2013b,a, 2015; Baker et al., 2014; Jaynes et al., 2014; Schiller et al., 2014a,b; Blum et al., 2013; Blum and Schiller, 2012; Kohnert et al., 2011; Palo et al., 2010; Schiller and Mahendrakumar, 2010; Gerhardt, 2010; Gerhardt

and Palo, 2016a,b). Leveraging that success and the recent development of a commercially available, precision three-axis ADCS, MinXSS will push the boundary of what science is possible with a CubeSat further still. The primary science objective of MinXSS is to fill a critical spectral gap in solar measurements currently made by large satellite missions at one hundredth their typical cost. All standard satellite subsystems are present in the MinXSS, except propulsion, packaged in a volume that can fit in a breadbox. Many of these subsystems were custom developed by CU and LASP (e.g., CDH, EPS, SPS, and XS, structure), primarily by graduate students with professional mentorship; and other subsystems were purchased from commercial vendors (e.g., flight radio, ADCS, primary science instrument).

Bibliography

- Acton, L. W., Weston, D. C., and Bruner, M. E. (1999). Deriving solar X ray irradiance from Yohkoh observations. *Journal of Geophysical Research*, 104(A7):14827.
- Andretta, V., Del Zanna, G., and Jordan, S. D. (2003). The EUV helium spectrum in the quiet Sun: A by-product of coronal emission? *Astronomy and Astrophysics*, 400(2):737–752.
- Arp, U., Clark, C., Deng, L., Faradzhev, N., Farrell, A., Furst, M., Grantham, S., Hagley, E., Hill, S., Lucatorto, T., Shaw, P.-S., Tarrio, C., and Vest, R. (2011). SURF III: A flexible synchrotron radiation source for radiometry and research. *Nuclear Instruments and Methods in Physics Research Section A: Accelerators, Spectrometers, Detectors and Associated Equipment*, 649(1):12–14.
- Aschwanden, M. J. (2009). 4-D modeling of CME expansion and EUV dimming observed with STEREO/EUVI. *Annales Geophysicae*, 27(8):3275–3286.
- Aschwanden, M. J., Nitta, N. V., Wuelser, J.-P., Lemen, J. R., Sandman, A., Vourlidas, A., and Colaninno, R. C. (2009a). First Measurements of the Mass of Coronal Mass Ejections From the EUV Dimming Observed With Stereo EUVI A + B Spacecraft. *The Astrophysical Journal*, 706(1):376–392.
- Aschwanden, M. J., Wuelser, J. P., Nitta, N. V., and Lemen, J. R. (2009b). Solar Flare and CME Observations with STEREO/EUVI. *Solar Physics*, 256(1-2):3–40.
- Attrill, G. D. R., Harra, L. K., van Driel-Gesztelyi, L., and Wills-Davey, M. J. (2010). Revealing the Fine Structure of Coronal Dimmings and Associated Flows with Hinode/EIS. *Solar Physics*, 264(1):119–147.
- Bailey, S. M., Woods, T. N., Barth, C. A., Solomon, S. C., Canfield, L. R., and Korde, R. (2000). Measurements of the solar soft X-ray irradiance by the Student Nitric Oxide Explorer : First analysis and underflight calibrations. *Journal of Geophysical Research*, 105:27179–193.
- Baker, D. N., Jaynes, A. N., Hoxie, V. C., Thorne, R. M., Foster, J. C., Li, X., Fennell, J. F., Wygant, J. R., Kanekal, S. G., Erickson, P. J., Kurth, W., Li, W., Ma, Q., Schiller, Q., Blum, L., Malaspina, D. M., Gerrard, A., and Lanzerotti, L. J. (2014). An impenetrable barrier to ultrarelativistic electrons in the Van Allen radiation belts. *Nature*, 515(7528):531–4.
- Bein, B. M., Temmer, M., Vourlidas, A., Veronig, A. M., and Utz, D. (2013). THE HEIGHT EVOLUTION OF THE TRUE CORONAL MASS EJECTION MASS DERIVED FROM STEREO COR1 AND COR2 OBSERVATIONS. 31.

- Bevington, P. (2003). *Data reduction and error analysis for the physical sciences*. McGraw-Hill, Boston.
- Bewsher, D., Harrison, R. A., and Brown, D. S. (2008). The relationship between EUV dimming and coronal mass ejections I. Statistical study and probability model. *Astronomy & Astrophysics*, 478:897–906.
- Blum, L. and Schiller, Q. (2012). Characterization and Testing of an Energetic Particle Telescope for a CubeSat Platform.
- Blum, L. W., Schiller, Q., Li, X., Millan, R., Halford, A., and Woodger, L. (2013). New conjunctive CubeSat and balloon measurements to quantify rapid energetic electron precipitation. *Geophysical Research Letters*, 40(22):5833–5837.
- Caspi, A. and Lin, R. P. (2010). RHESSI Line and Continuum Observations of Super-hot Flare Plasma. *The Astrophysical Journal*, 725:L161–166.
- Caspi, A., McTiernan, J. M., and Warren, H. P. (2014). CONSTRAINING SOLAR FLARE DIFFERENTIAL EMISSION MEASURES WITH EVE AND RHESSI. *The Astrophysical Journal*, 788(2):L31.
- Caspi, A., Woods, T. N., and Warren, H. P. (2015). New Observations of the Solar 0.55 Kev Soft X-Ray Spectrum. *The Astrophysical Journal*, 802(1):L2.
- Chamberlin, P. C., Woods, T. N., and Eparvier, F. G. (2007). Flare Irradiance Spectral Model (FISM): Daily component algorithms and results. *Space Weather*, 5(7):n/a–n/a.
- Chamberlin, P. C., Woods, T. N., and Eparvier, F. G. (2008). Flare Irradiance Spectral Model (FISM): Flare component algorithms and results. *Space Weather*, 6(5):n/a–n/a.
- Chamberlin, P. C., Woods, T. N., Eparvier, F. G., and Jones, A. R. (2009). <title>Next generation x-ray sensor (XRS) for the NOAA GOES-R satellite series</title>. In Fineschi, S. and Fennelly, J. A., editors, *SPIE Optical Engineering + Applications*, pages 743802–743802–10. International Society for Optics and Photonics.
- Chen, P. F., Fang, C., and Shibata, K. (2005). A Full View of EIT Waves. *The Astrophysical Journal*, 622(2):1202–1210.
- Chen, P. F., Wu, S. T., Shibata, K., and Fang, C. (2002). Evidence of EIT and Moreton Waves in Numerical Simulations. *The Astrophysical Journal*, 572(1):L99–L102.
- Christensen-Dalsgaard, J., Dappen, W., Ajukov, S. V., Anderson, E. R., Antia, H. M., Basu, S., Baturin, V. A., Berthomieu, G., Chaboyer, B., Chitre, S. M., Cox, A. N., Demarque, P., Donatowicz, J., Dziembowski, W. A., Gabriel, M., Gough, D. O., Guenther, D. B., Guzik, J. A., Harvey, J. W., Hill, F., Houdek, G., Iglesias, C. A., Kosovichev, A. G., Leibacher, J. W., Morel, P., Proffitt, C. R., Provost, J., Reiter, J., Rhodes, E. J., Rogers, F. J., Roxburgh, I. W., Thompson, M. J., and Ulrich, R. K. (1996). The Current State of Solar Modeling. *Science*, 272(5266):1286–1292.
- Colaninno, R. C. and Vourlidas, A. (2009). First Determination of the True Mass of Coronal Mass Ejections: A Novel Approach To Using the Two Stereo Viewpoints. *The Astrophysical Journal*, 698:852–858.

- Colaninno, R. C., Vourlidas, A., and Wu, C. C. (2013). Quantitative comparison of methods for predicting the arrival of coronal mass ejections at Earth based on multiview imaging. *Journal of Geophysical Research: Space Physics*, 118(11):6866–6879.
- Dere, K. P., Landi, E., Mason, H. E., Monsignori Fossi, B. C., and Young, P. R. (1997). CHIANTI - an atomic database for emission lines. *Astronomy and Astrophysics Supplement Series*, 125:149–173.
- Doschek, G. A. (1990). Soft X-ray spectroscopy of solar flares - an overview. *The Astrophysical Journal Supplement Series*, 73:117.
- Eddy, J. A. (1979). *A New Sun: The Solar Results from Skylab*. National Aeronautics and Space Administration, Washington, D. C.
- Fletcher, L., Dennis, B. R., Hudson, H. S., Krucker, S., Phillips, K., Veronig, A. M., Battaglia, M., Bone, L., Caspi, A., Chen, Q., Gallagher, P. T., Grigis, P. T., Ji, H., Liu, W., Milligan, R. O., and Temmer, M. (2011). An Observational Overview of Solar Flares. *Space Science Reviews*, 159(1-4):19–106.
- Gary, G. A. (2001). Plasma Beta above a Solar Active Region: Rethinking the Paradigm. *Solar Physics*, 203(1):71–86.
- Gerhardt, D. (2010). Passive Magnetic Attitude Control for CubeSat Spacecraft.
- Gerhardt, D. and Palo, S. (2016a). Volume Magnetization for System-Level Testing of Magnetic Materials within Small Satellites.
- Gerhardt, D. and Palo, S. E. (2016b). Passive Magnetic Attitude Control Settling Prediction with On-Orbit Verification using the Colorado Student Space Weather Experiment CubeSat.
- Gerhardt, D., Palo, S. E., Schiller, Q., Blum, L., Li, X., and Kohnert, R. (2013). The Colorado Student Space Weather Experiment (CSSWE) On-Orbit Performance. *Journal of Small Satellites*, 3(1):265–281.
- Gilbert, H. R., Inglis, a. R., Mays, M. L., Ofman, L., Thompson, B. J., and Young, C. a. (2013). Energy Release From Impacting Prominence Material Following the 2011 June 7 Eruption. *The Astrophysical Journal*, 776(1):L12.
- Giordano, S., Antonucci, E., and Dodero, M. (2000). OXYGEN VELOCITIES IN A POLAR CORONAL. *Advances in Space Research*, 25(9):1927–1930.
- Gopalswamy, N., Yashiro, S., Michalek, G., Stenborg, G., Vourlidas, A., L, F. S., and Howard, R. A. (2009). The SOHO / LASCO CME Catalog. *Earth Moon Planet*, 104:295–313.
- Greenstein, J. L. (1958). High-Resolution Spectra of Comet MRKOS. *The Astrophysical Journal*, 128:106.
- Harra, L. K., Mandrini, C. H., Dasso, S., Gulisano, A. M., Steed, K., and Imada, S. (2010). Determining the Solar Source of a Magnetic Cloud Using a Velocity Difference Technique. *Solar Physics*, 268(1):213–230.
- Harra, L. K. and Sterling, A. C. (2001). Material Outflows from Coronal Intensity "Dimming Regions" During Coronal Mass Ejection Onset. *The Astrophysical Journal Letters*, 561:215–218.

- Harrison, R. A., Bryans, P., Simnett, G. M., and Lyons, M. (2003). Coronal dimming and the coronal mass ejection onset. *Astronomy & Astrophysics*, 400:1071–1083.
- Harrison, R. A. and Lyons, M. (2000). A spectroscopic study of coronal dimming associated with a coronal mass ejection. *Astronomy & Astrophysics*, 1108:1097–1108.
- Hudson, H. S., Lemen, J. R., St. Cyr, O. C., Sterling, A. C., and Webb, D. F. (1998). X-ray coronal changes during halo CMEs. *Geophysical Research Letters*, 25(14):2481–2484.
- Hudson, H. S., Woods, T. N., Chamberlin, P. C., Fletcher, L., Zanna, G. D., Didkovsky, L., Labrosse, N., and Graham, D. (2011). The EVE Doppler Sensitivity and Flare Observations. *Solar Physics*, 273:69–80.
- Hyder, C. L. and Lites, B. W. (1970). H-alpha Doppler Brightening and Lyman-alpha Doppler Dimming in Moving H-alpha Prominences. *Solar Physics*, 14(1):147–156.
- Imada, S., Hara, H., Watanabe, T., Kamio, S., Asai, A., Matsuzaki, K., Harra, L. K., and Mariska, J. T. (2007). Discovery of a Temperature-Dependent Upflow in the Plage Region during a Gradual Phase of the X-Class Flare. *Publications of the Astronomical Society of Japan*, 59(sp3):S793–S799.
- Jaynes, A. N., Li, X., Schiller, Q. G., Blum, L. W., Tu, W., Turner, D. L., Ni, B., Bortnik, J., Baker, D. N., Kanekal, S. G., Blake, J. B., and Wygant, J. (2014). Evolution of relativistic outer belt electrons during an extended quiescent period. *Journal of Geophysical Research: Space Physics*, 119(12):9558–9566.
- Jin, M., Ding, M. D., Chen, P. F., Fang, C., and Imada, S. (2009). CORONAL MASS EJECTION INDUCED OUTFLOWS OBSERVED WITH HINODE /EIS. *The Astrophysical Journal*, 702(1):27–38.
- Kahler, S. (1992). Solar Flares and Coronal Mass Ejections. *Annual Review of Astronomy and Astrophysics*, 30:113–141.
- Kahler, S. W. (1982). The role of the big flare syndrome in correlations of solar energetic proton fluxes and associated microwave burst parameters. *Journal of Geophysical Research*, 87(A5):3439.
- Klimchuk, J. A. (2006). On Solving the Coronal Heating Problem. *Solar Physics*, 234(1):41–77.
- Kohnert, R., Palo, S., and Li, X. (2011). Small Space Weather Research Mission Designed Fully by Students. *Space Weather*, 9(4):n/a–n/a.
- Krista, L. D. and Reinard, A. (2013). STUDY OF THE RECURRING DIMMING REGION DETECTED AT AR 11305 USING THE CORONAL DIMMING TRACKER (CoDiT). *The Astrophysical Journal*, 762(2):91.
- Labrosse, N. and Mcglinchey, K. (2012). Plasma diagnostic in eruptive prominences from SDO / AIA observations at 304 Å. *Astronomy & Astrophysics*, 537:A100.
- Landi, E., Del Zanna, G., Young, P. R., Dere, K. P., Mason, H. E., and Landini, M. (2006). CHIANTIAn Atomic Database for Emission Lines. VII. New Data for XRays and Other Improvements. *The Astrophysical Journal Supplement Series*, 162:261–280.

- Lang, . (2001). The Cambridge Encyclopedia of the Sun. *The Cambridge Encyclopedia of the Sun*.
- Li, X., Palo, S., Kohnert, R., Blum, L., Gerhardt, D., Schiller, Q., and Califf, S. (2013a). Small Mission Accomplished by Students-Big Impact on Space Weather Research. *Space Weather*, 11(2):55–56.
- Li, X., Palo, S., Kohnert, R., Gerhardt, D., Blum, L., Schiller, Q., Turner, D., Tu, W., Sheiko, N., and Cooper, C. S. (2012). Colorado Student Space Weather Experiment: Differential Flux Measurements of Energetic Particles in a Highly Inclined Low Earth Orbit. In Summers, D., Mann, I. R., Baker, D. N., and Schulz, M., editors, *Dynamics of the Earth's Radiation Belts and Inner Magnetosphere*, Geophysical Monograph Series, pages 385–411, Washington, D. C. American Geophysical Union.
- Li, X., Schiller, Q., Blum, L., Califf, S., Zhao, H., Tu, W., Turner, D. L., Gerhardt, D., Palo, S., Kanekal, S., Baker, D. N., Fennell, J., Blake, J. B., Looper, M., Reeves, G. D., and Spence, H. (2013b). First results from CSSWE CubeSat: Characteristics of relativistic electrons in the near-Earth environment during the October 2012 magnetic storms. *Journal of Geophysical Research: Space Physics*, 118(10):6489–6499.
- Li, X., Selesnick, R. S., Baker, D. N., Jaynes, A. N., Kanekal, S. G., Schiller, Q., Blum, L., Fennell, J., and Blake, J. B. (2015). Upper limit on the inner radiation belt MeV electron intensity. *Journal of geophysical research. Space physics*, 120(2):1215–1228.
- Lin, R. P., Dennis, B. R., Hurford, G. J., Smith, D. M., Zehnder, A., Harvey, P. R., Curtis, D. W., Pankow, D., Turin, P., Bester, M., Csillaghy, A., Lewis, M., Madden, N., Beek, H. F., Appleby, M., Raudorf, T., McTiernan, J., Ramaty, R., Schmahl, E., Schwartz, R., Krucker, S., Abiad, R., Quinn, T., Berg, P., Hashii, M., Sterling, R., Jackson, R., Pratt, R., Campbell, R. D., Malone, D., Landis, D., Cork, C., Tolbert, A. K., Zarro, D. M., Snow, F., Thomsen, K., and Henneck, R. (2002). The Reuven Ramaty High-Energy Solar Spectroscopic Imager (RHESSI). *Solar Physics*, 210:3–32.
- Liu, W. and Ofman, L. (2014). Advances in Observing Various Coronal EUV Waves in the SDO Era and Their Seismological Applications (Invited Review). *Solar Physics*, 289(9):3233–3277.
- Mason, J. P., Woods, T. N., Caspi, A., Thompson, B. J., and Hock, R. A. (2014). MECHANISMS AND OBSERVATIONS OF CORONAL DIMMING FOR THE 2010 AUGUST 7 EVENT. *The Astrophysical Journal*, 789(1):61.
- Muhr, N., Veronig, A. M., Kienreich, I. W., and Temmer, M. (2011). Analysis of Characteristic Parameters of Large-Scale Coronal Waves Observed by the Solar-Terrestrial Relations Observatory/Extreme Ultraviolet Imager. *The Astrophysical Journal*, 89:89.
- Palo, S., Li, X., Gerhardt, D., Turner, D., Kohnert, R., Hoxie, V., and Batiste, S. (2010). Conducting Science with a CubeSat: The Colorado Student Space Weather Experiment.
- Parker, E. N. (1988). Nanoflares and the solar X-ray corona. *The Astrophysical Journal*, 330:474.
- Pearson, K. (1895). Note on Regression and Inheritance in the Case of Two Parents. *Proceedings of the Royal Society of London*, 58:240–242.
- Peterson, J. and Fabian, A. (2006). X-ray spectroscopy of cooling clusters. *Physics Reports*, 427(1):1–39.

- Peterson, W. K., Stavros, E. N., Richards, P. G., Chamberlin, P. C., Woods, T. N., Bailey, S. M., and Solomon, S. C. (2009). Photoelectrons as a tool to evaluate spectral variations in solar EUV irradiance over solar cycle timescales. *Journal of Geophysical Research*, 114:A10304.
- Pohjolainen, S., Vilmer, N., Khan, J. I., and Hillaris, A. E. (2005). Early signatures of large-scale field line opening Multi-wavelength analysis of features connected with a halo CME event. *Astronomy & Astrophysics*, 434:329–341.
- Reinard, A. A. and Biesecker, D. A. (2008). Coronal Mass Ejection-Associated Coronal Dimmings. *The Astrophysical Journal*, 674:576–585.
- Reinard, A. A. and Biesecker, D. A. (2009). The Relationship Between Coronal Dimming and Coronal Mass Ejection Properties. *The Astrophysical Journal*, 705(1):914–919.
- Robbrecht, E. and Wang, Y.-M. (2010). The Temperature-Dependent Nature of Coronal Dimmings. *The Astrophysical Journal Letters*, 720:88–92.
- Rodgers, E. M., Bailey, S. M., Warren, H. P., Woods, T. N., and Eparvier, F. G. (2006). Soft X-ray irradiances during solar flares observed by TIMED-SEE. *Journal of Geophysical Research*, 111(A10):A10S13.
- Rompolt, . (1967). The H α Radiation Field in the Solar Corona for Moving Prominences. *Acta Astronomica*, 17.
- Schiller, Q., Gerhardt, D., Blum, L., Li, X., and Palo, S. (2014a). Design and scientific return of a miniaturized particle telescope onboard the Colorado Student Space Weather Experiment (CSSWE) CubeSat. In *2014 IEEE Aerospace Conference*, pages 1–14. IEEE.
- Schiller, Q., Li, X., Blum, L., Tu, W., Turner, D. L., and Blake, J. B. (2014b). A nonstorm time enhancement of relativistic electrons in the outer radiation belt. *Geophysical Research Letters*, 41(1):7–12.
- Schiller, Q. and Mahendrakumar, A. (2010). REPTile: A Miniaturized Detector for a CubeSat Mission to Measure Relativistic Particles in Near-Earth Space.
- Schlemm, C. E., Starr, R. D., Ho, G. C., Bechtold, K. E., Hamilton, S. A., Boldt, J. D., Boynton, W. V., Bradley, W., Fraeman, M. E., Gold, R. E., Goldsten, J. O., Hayes, J. R., Jaskulek, S. E., Rossano, E., Rumpf, R. A., Schaefer, E. D., Strohbehn, K., Shelton, R. G., Thompson, R. E., Trombka, J. I., and Williams, B. D. (2007). The X-Ray Spectrometer on the MESSENGER Spacecraft. *Space Science Reviews*, 131(1-4):393–415.
- Schrijver, C. J. and Higgins, P. A. (2015). A Statistical Study of Distant Consequences of Large Solar Energetic Events. *Solar Physics*, 290(10):2943–2950.
- Solomon, S. C., Bailey, S. M., and Woods, T. N. (2001). Effect of solar soft X-rays on the lower ionosphere. *Geophysical Research Letters*, 28(11):2149–2152.
- Sterling, A. C. and Hudson, H. S. (1997). YOHKOH SXT OBSERVATIONS OF X-RAY DIMMING ASSOCIATED WITH A HALO CORONAL MASS EJECTION. *The Astrophysical Journal*, 491:L55–L58.

- Swings, P. (1941). Complex Structure of Cometary bands Tentatively Ascribed to the Contour of the Solar Spectrum. Lick Observatory Bulletin, 508.
- Thompson, B. J., Cliver, E. W., Nitta, N. V., Delannée, C., and Delaboudiniere, J. P. (2000). Coronal Dimmings and Energetic CMEs in April-May 1998. Geophysical Research Letters, 27(10):1431–1434.
- Tian, H., McIntosh, S. W., Xia, L., He, J., and Wang, X. (2012). What Can We Learn About Solar Coronal Mass Ejections, Coronal Dimmings, and Extreme-Ultraviolet Jets Through Spectroscopic Observations? The Astrophysical Journal, 748(2):106.
- Vourlidas, A., Howard, R. A., Esfandiari, E., Patsourakos, S., Yashiro, S., and Michalek, G. (2010). Comprehensive Analysis of Coronal Mass Ejection Mass and Energy Properties Over a Full Solar Cycle. The Astrophysical Journal, 722:1522–1538.
- Vourlidas, A., Howard, R. A., Esfandiari, E., Patsourakos, S., Yashiro, S., and Michalek, G. (2011). ERRATUM : COMPREHENSIVE ANALYSIS OF CORONAL MASS EJECTION MASS AND ENERGY PROPERTIES OVER A FULL SOLAR CYCLE (2010 , ApJ , 722 , 1522). 59:2010–2012.
- Vourlidas, A., Subramanian, P., Dere, K. P., and Howard, R. A. (2000). LargeAngle Spectrometric Coronagraph Measurements of the Energetics of Coronal Mass Ejections. The Astrophysical Journal, 534(1):456–467.
- Woods, T. N. and Chamberlin, P. C. (2009). Comparison of solar soft X-ray irradiance from broadband photometers to a high spectral resolution rocket observation. Advances in Space Research, 43:349–354.
- Woods, T. N., Chamberlin, P. C., Peterson, W. K., Meier, R. R., Richards, P. G., Strickland, D. J., Lu, G., Qian, L., Solomon, S. C., Iijima, B. A., Mannucci, A. J., and Tsurutani, B. T. (2008). XUV Photometer System (XPS): Improved Solar Irradiance Algorithm Using CHIANTI Spectral Models. Solar Physics, 250(2):235–267.
- Woods, T. N., Eparvier, F. G., Bailey, S. M., Chamberlin, P. C., Lean, J., Rottman, G. J., Solomon, S. C., Tobiska, W. K., and Woodraska, D. L. (2005a). Solar EUV Experiment (SEE): Mission overview and first results. Journal of Geophysical Research, 110:A01312.
- Woods, T. N., Hock, R. A., Eparvier, F. G., Jones, A. R., Chamberlin, P. C., Klimchuk, J. A., Didkovsky, L., Judge, D., Mariska, J. T., Warren, H. P., Schrijver, C. J., Webb, D. F., Bailey, S. M., and Tobiska, W. K. (2011). New Solar Extreme-Ultraviolet irradiance Observations During Flares. The Astrophysical Journal, 739:59.
- Woods, T. N., Rottman, G., and Vest, R. (2005b). XUV Photometer System (XPS): Overview and Calibrations. Solar Physics, 230(1-2):345–374.
- Zhukov, A. N. and Auchère, F. (2004). On the nature of EIT waves, EUV dimmings and their link to CMEs. Astronomy & Astrophysics, 427:705–716.

Appendix A

Coronal Dimming Event List and Ancillary Data

Appendix B

MinXSS CubeSat Mass/Power Tables

(Data, Stardate 1403827) (A one-page chapter — page must be numbered!) Throughout the ages, from Keats to Giorchamo, poets have composed “odes” to individuals who have had a profound effect upon their lives. In keeping with that tradition I have written my next poem . . . in honor of my cat. I call it . . . Ode . . . to Spot. (Shot of Geordi and Worf in audience, looking mystified at each other.)

Felus cattus, is your taxonomic nomenclature
 an endothermic quadruped, carnivorous by nature?
 Your visual, olfactory, and auditory senses
 contribute to your hunting skills, and natural defenses.
 I find myself intrigued by your sub-vocal oscillations,
 a singular development of cat communications
 that obviates your basic hedonistic predilection
 for a rhythmic stroking of your fur to demonstrate affection.
 A tail is quite essential for your acrobatic talents;
 you would not be so agile if you lacked its counterbalance.
 And when not being utilized to aid in locomotion,
 It often serves to illustrate the state of your emotion.

(Commander Riker begins to applaud, until a glance from Counselor Troi brings him to a halt.) Commander Riker, you have anticipated my denouement. However, the sentiment is appreciated. I will continue.

O Spot, the complex levels of behavior you display
 connote a fairly well-developed cognitive array.
 And though you are not sentient, Spot, and do not comprehend
 I nonetheless consider you a true and valued friend.